Deterministic-Kinetic Computational Analyses of Expansion Flows and Current-Carrying Plasmas

by

Alexander Ryan Vazsonyi

A dissertation submitted in partial fulfillment
of the requirements for the degree of
Doctor of Philosophy
(Aerospace Engineering)
in The University of Michigan
2021

Doctoral Committee:

Professor Benjamin A. Jorns, Chair
Adjunct Professor Iain D. Boyd
Professor Alec D. Gallimore
Professor Mark J. Kushner

"And this I believe: that the free, exploring mind of the individual human is the most valuable thing in the world. And this I would fight for: the freedom of the mind to take any direction it wishes, undirected. And this I must fight against: any idea, religion, or government which limits or destroys the individual."

– John Steinbeck, *East of Eden*

Alexander Ryan Vazsonyi
vazsonyi@umich.edu
ORCID iD: 0000-0001-9531-7139

For Sarah

ACKNOWLEDGEMENTS

More than simply the result of four years of study at the University of Michigan, this dissertation represents the culmination of decades of encouragement, support, and mentorship from family, friends, teachers, professors, and professionals.

My journey towards a PhD in engineering began in high school FIRST Robotics. Under the mentorship of Doug Hepfer and Mike Evele, I not only became interested in science and engineering but was trusted to leadership roles which gave me the confidence to pursue my goals. In no small way did this experience ready me for study at the University of Kentucky, which gave me the immensely generous opportunity to study engineering under the Otis A. Singletary Scholarship (financed in part, through the UK Basketball program; thank you Coach Cal and Go Cats!). At Kentucky, Drs. Suzanne Smith, Alexandre Martin, and Sean Bailey all provided me with many opportunities to develop and grow as a researcher, which readied me for my time at the University of Michigan.

For my time at the University of Michigan, the foremost person to thank is my advisor Dr. Iain Boyd. He gave me the opportunity to study at a wonderful institution, supported my various endeavors, and guided me down many successful paths. I want to thank Dr. Ben Jorns for collaborating with me on my research, while also including me in meetings with the PEPL group; within PEPL, I enjoyed collaborations with Dr. Sarah Cusson and Leanne Su on Hall thruster modeling. I would like to acknowledge my committee members Drs. Mark Kushner and Alec Gallimore for agreeing to see my research through and providing useful insight.

During my time at Michigan, I was able to collaborate with many fantastic researchers across the world. Drs. Justin Koo and David Bilyeu at the Air Force Research Lab took me under their wing, and despite my inexperience, provided me with a chance to prove myself and learn. Dr. Laurent Garrigues at the University of Toulouse generously and graciously hosted me to discuss research and even took me to see the Tour de France, an experience which I remember very fondly. Finally, I must profusely thank Dr. Ken Hara for providing me with the opportunity to visit Stanford University, for being a very kind and accommodating host, and for, despite my impatience at times, pushing me to become a better researcher.

This dissertation was supported primarily by the National Defense Science and Engineering Graduate (NDSEG) Fellowship through the Air Force Office of Scientific Research, an award which I was humbled and privileged to receive. In addition, the University of Michigan College of Engineering's Rollin M. Gerstacker Fellowship supported my first year of study, and generous subsequent support came through various grants from the Rackham Graduate School and the College of Engineering. I am also grateful for the Michigan Institute for Plasma Science and Engineering's (MIPSE) support through the MIPSE Graduate Fellowship.

None of these opportunities would have been possible without the friendships I have been so lucky to hold throughout the years. To my childhood friends (Alan, Brian), my GHS friends (Dan, Teddy, Morrie, Jesse, Izzy), my UK friends (Mitch, Joon) and many others who have gotten me to where I am today, thank you. In Ann Arbor, there were many people I was lucky to meet whom I worked with, shared struggles with, and laughed with: Michael Holloway, Kaelan Hansson, Prince Kuevor, Gary Collins, Drs. Sam Chen and John Jasa. Of course, I have to mention my intermural sports crew, including Michael Holloway, Prince Kuevor, Dr. John Jasa, Dr. Puneet Singh, Ryan Patterson, and others. I had friends who were also mentors: Drs. Horatiu Dragnea and Astrid Raisanen, thank you for your friendship and mentorship.

Most importantly of all on this journey has been the support of my family. To my mother Kristina and father Alexander, who instilled in me the virtues of humility and tenacity. To my maternal grandparents, especially Samuel, whose pure delight in my endeavors has been a consistent source of motivation. To my paternal grandparents, first-generation immigrants to the United States who brought our family to opportunity; Susanna, my Canasta partner, and Gabi, who fled the persecution of the Iron Curtain. To my siblings, Philip, Marc, Katarina, and Jenna, who have (although a bit tardily) taken out the drab of being an only child and brought so much fun into my life. Finally, to my wife Sarah, for being more supportive than I thought possible, always listening to my struggles, taking pride in my accomplishments, and motivating me to be better. This accomplishment is as much all of yours as it is my own.

> ”Before it is science and career, before it is livelihood, before even it is family or love, freedom is sound sleep and safety to notice the play of morning sun.” -*Richard Rhodes*

TABLE OF CONTENTS

CHAPTER

LIST OF FIGURES

Figure

LIST OF TABLES

Table

LIST OF ABBREVIATIONS

AMR adaptive mesh refinement

BGK Bhatnagar-Gross-Crook

CEX charge exchange

CFL Courant-Friedrichs-Lewis

CPU Central Processing Unit

DK deterministic-kinetic

DSMC direct-simulation Monte Carlo

EP electric propulsion

ES-BGK ellipsoidal-statistical Bhatnagar-Gross-Crook

ESA European Space Agency

FFT Fast-Fourier Transform

IAI ion-acoustic instability

IMEX implicit-explicit

MEX momentum exchange

MFP mean free path

MPI Message Passing Interface

MUSCL Monotonic Upwind Scheme for Conservation Laws

NASA National Aeronautics and Space Administration

NDL non-monotonic double layer

OAI off-axis instability

PIC Particle-in-Cell

SCCM standard cubic centimeters per minute

TSI two-stream instability

TVD total-variation-diminishing

VDF velocity distribution function

VHS Variable Hard Sphere

ABSTRACT

Spacecraft electric propulsion (EP) takes advantage of the ability of electric and magnetic fields to accelerate plasmas to high velocities to generate efficient thrust. The thermionic hollow cathode is a critical component to both gridded-ion and Hall-effect thrusters, the state-of-the-art devices of the EP discipline. However, experiments demonstrate that the hollow cathode is plagued by erosion of its surfaces by the plasma, which may eventually cause premature failure of the device. This erosion has been linked to the ion-acoustic instability (IAI), a kinetic plasma instability which operates in the cathode plume. Existence of this kinetic instability has prevented numerical simulation from predicting the operating characteristics and lifetime of the hollow cathode device. Therefore, this thesis utilizes deterministic-kinetic (DK) simulation of gas and plasma flows to further the understanding of the IAI as it relates to the hollow cathode plume and to ultimately develop a predictive hollow cathode simulation platform. Towards these goals, two approaches to applying the DK simulation method to the hollow cathode plasma are undertaken: hybrid-kinetic simulation and fully-kinetic simulation.

Hybrid-kinetic simulations utilize a kinetic description of the heavy propellant particles while using a reduced-order, fluid approach for the light electrons. Two unique two-dimensional, axisymmetric kinetic schemes are developed, one for neutral particles and one for ions; the schemes are verified by comparison with solutions obtained using the direct-simulation Monte Carlo method and with an analytic solution for a rarefied neutral jet flow. Assuming quasi-neutrality in the hollow cathode plasma and using the Boltzmann relation for the plasma potential, the hybrid-kinetic solver is applied to the problem of NASA's NSTAR discharge hollow cathode. Partial validation is achieved through agreement with experimental Langmuir probe data in the near-orifice region, while shortcomings of the solver such as use of a simplified electron model are discussed.

Fully-kinetic simulations, where all species are considered kinetically, are carried out to study the IAI. The anomalous resistivity generated by the IAI is measured from one-dimensional fully-kinetic simulations and compared with a closure model commonly used in hollow cathode fluid codes, finding that the agreement with the closure model varies based on simulation domain size and electron Mach number. Further, the formation of high-energy tails in the ion velocity distribution function is observed near the transition to the Buneman instability, another instability of current-carrying plasmas. Two-dimensional kinetic simulations of current-carrying instabilities are carried out, finding that the nature of nonlinear saturation of the IAI differs significantly from that shown in one-dimensional simulations. A phenomenon known as the off-axis instability generates waves propagating normal to the current direction which eventually reach energy levels close to that of the waves along the current direction.

Further fully-kinetic simulations demonstrate the formation of weak plasma double layers, regions of plasma which sustain a potential gradient, in the nonlinear saturation stage of the IAI. These double layers are found to be ubiquitous in all plasma species considered, even the heavy xenon ions commonly used in hollow cathodes. Phase space analysis suggests the double layers form from ion-acoustic wave packets which grow into ion phase space holes. Spectral analysis demonstrates a shift towards smaller wavenumbers which marks this transition. An electron two-stream instability is spawned due to the potential well of the double layer, where spectral analyses demonstrate that a simple theoretical expression well-predicts the resulting wave phase velocity.

CHAPTER I

Introduction

> *"It is wrong to think that the task of physics is to figure out how nature is. Physics concerns what we can say about nature."*
>
> – Niels Bohr, as quoted by Aage Peterson

This chapter sets the stage for the work performed in this thesis. In Section 1.1, the motivations for pursuing the problems addressed throughout the thesis are described. Section 1.2 details the general theory of gas and plasma dynamics, which is the foundation of this work. In Section 1.3, the field of spacecraft propulsion is briefly surveyed, a field with which much of this work is concerned. Finally, Section 1.4 lays out the objectives that this thesis strives to accomplish.

1.1 Motivations

The advent of modern-day computing has had profound impacts on science and engineering. With ever increasing computational resources, problems of ever higher complexity are being unlocked for detailed study. The fields of fluid dynamics and plasma physics, notorious for their complexity, have benefited greatly by weaving the newer field of computational physics into their midst. The use of computers allows the scientist or engineer to peer into spatial and temporal scales which are as of yet inaccessible to experimental apparatus, with limited concerns for safety, cost, and time. As a companion to theoretical and experimental study, *numerical* study has proven an invaluable asset in science and engineering.

The massive increase in computational resources over the past few decades has enabled *direct* computational analysis of fluids and plasmas. That is to say, rather than making simplifying assumptions regarding the state of the fluid/plasma which allow for a reduced computational burden, the governing equation(s) may be solved directly. This relatively recent development makes numerical analysis all-the-more valuable, as the caveats to results introduced by simplifying assumptions are slowly being dropped.

Increasing access to direct computational analysis has had a profound effect on the field of spacecraft electric propulsion. In this field, gas and plasma flows are utilized in order to generate thrust in-space. In recent years, it has come to the attention of this field that thruster technologies which have decades of flight heritage are subject to an array of plasma instabilities, some of which tend to dominate the plasma discharge. These instabilities may degrade the operating efficiency of the thruster and even limit their operational lifetime due to effects such as erosion of the thruster body. One example of such an instability is the ion-acoustic instability, which has been identified to operate in the plume of the hollow cathode device, a sub-component of various flight-proven thruster technologies. This instability has been postulated as a primary life-limiting factor for the hollow cathode, as it is linked to surface erosion measured in standalone cathode tests. Therefore, this thesis aims to take advantage of the advent of direct numerical analysis of fluids and plasmas by applying it to problems of interest to the field of spacecraft electric propulsion, particularly relating to the effect of plasma instabilities and their role in the thermionic hollow cathode.

1.2 Gas and Plasma Dynamics

Macroscopically, gas is a state of matter with variable volume and shape. Microscopically, atoms or molecules of a gas freely traverse space and only interact with their neighbors through collisions. The average distance which a gas particle travels before encountering and colliding with another is known as the mean free path (MFP), λ. The degree of collisionality within a gas uniquely determines the theory which describes its motion and bulk properties. To measure this property, a non-dimensional parameter known as the Knudsen number:

$$Kn = \frac{\lambda}{L}, \tag{1.1}$$

was devised. The Knudsen number compares the MFP with the characteristic length of the gas container, L. Three general regimes exist to describe the state of the gas: continuum, transitional, and free molecular. In the continuum state, where $Kn < 0.01$, collisions between gas molecules are frequent. In the free molecular state, where $Kn > 10$, collisions are infrequent; the state between these two is known as the transitional state, where $0.01 < Kn < 10$.

Each of these three states lead to entirely different behavior of the gas; to understand why this is, the concept of the velocity distribution function (VDF), $f(\mathrm{v})$, is important. Any particular gas is composed of a massive amount of particles which each move with a velocity, v. In virtually every case, these velocities are not all identical, but rather form a *distribution* of velocities. The function $f(\mathrm{v})$ thus describes how many particles exist at each value for velocity, v. Now, going back to the concept of the Knudsen number: the action of collisions is to drive the particles towards a state of *equilibrium.* That is, in highly collisional (or continuum) flows, the particles of the gas exchange information so frequently that they are in a constant state of equilibrium. This equilibrium state in terms of velocity, or translational energy, is described by the Maxwell-Boltzmann, or Maxwellian, distribution:

$$f_M(\mathrm{v})\mathrm{dv} = \prod_{n_d=1}^{N} \left(\frac{m}{2\pi k_b T}\right)^{n_d/2} \exp\left(\frac{-m v_{n_d}^2}{2k_b T}\right)\mathrm{dv}, \tag{1.2}$$

where N is the number of dimensions, k_b is Boltzmann's constant, m is the species mass, and T is the species temperature. On the other hand, in the case of free molecular flow information is exchanged relatively infrequently; this allows the gas to reach a state of *non-equilibrium*, where the VDF is no longer necessarily described by the Maxwellian distribution.

The description of a gas as a distribution of particles with differing velocities applies equally well to a plasma. Plasma is often considered the fourth state of matter, where some fraction of a gas population has been *ionized*. That is, atoms or molecules of the gas have had electrons stripped off and free electrons exist in the flow; this may occur through a variety of physical mechanisms. Thus, a plasma consists of the charged particles known as ions and electrons, as well as some fraction of neutral gas particles. As in a gas, these particles all flow freely and interact via collisions, with one major exception: due to the charged nature of ions and electrons, they are subject to Coulombic interaction with each other and to the effects of external electric and magnetic fields. This property of the plasma, that the particles are able to interact from long ranges due to the electromagnetic fields between them, leads to what is otherwise known as *collective* behavior: the tendency for a plasma to respond to external influence by the collective motion of its constituent charged particles.

If plasmas are indeed considered to be the fourth state of matter, why, then, are they not commonly encountered on Earth? While plasmas exist naturally throughout the universe, they exist on Earth in a limited variety of forms: lightning bolts, the Aurora Borealis, and fluorescent lights, to name a few. Due to the high density of gas in Earth's atmosphere, plasmas do not exist under ambient conditions; the reason for this can be understood from the Saha equation, which gives the fraction of ionized particles to neutral particles:

$$\frac{n_i}{n_n} \approx 2.4 \times 10^{21} \frac{T^{3/2}}{n_i} \exp\left(\frac{-U_i}{k_b T}\right), \tag{1.3}$$

where U_i is the ionization energy, n_n is the neutral density, and n_i is the ion density. Assuming the atmosphere to be composed of molecular nitrogen, then $U_i = 14.5$ eV, $T = 300$K and $n_n \approx 3 \times 10^{25}$; this leads to an ionization fraction of $n_i/n_n \approx 10^{-122}$, which is certainly negligible. The reason for this absence of plasma lies in collisions: at low temperature, collisions aren't energetic enough to ionize the gas, and further, collisions with neutral particles cause any charged particles that do arise to recombine. Even in a plasma, this process of recombination occurs at some finite rate, which is the reason that plasmas are often encountered under near or total *vacuum* conditions, where the neutral particle density is very low.

The distinction of where a gas becomes a plasma, and vice versa, is an important one. To make this distinction, a variety of characteristic parameters are useful. In a plasma, the motion of charged particles tends to drive internal electric fields towards zero, which causes plasmas to generally be *quasi-neutral.* That is to say, if a test particle with finite charge is inserted into a plasma, the plasma re-organizes itself to shield out the charge. However, within a small enough spatial scale, finite electric fields do remain in the plasma; this characteristic spatial scale of plasmas is known as the Debye length:

$$\lambda_D = \sqrt{\frac{\epsilon_0 k_b / q_e^2}{n_e/T_e + n_i/T_i}}, \tag{1.4}$$

where ϵ_0 is the permittivity of free space, n_e is the electron number density, q_e is the elementary charge, and T_e and T_i are the electron and ion temperatures. Often times, the ion term is dropped by assuming the mobility of ions is negligible compared to the process time scale. The Debye length serves as one criterion in distinguishing a plasma: should a collection of charged particles exist in a container with length L, the Debye length must be much smaller, or $\lambda_D \ll L$, in order for a plasma to exist. Otherwise, rather than being quasi-neutral, the charged particles would sustain finite electric fields within the container.

The temporal characteristic parameter of plasmas is known as the plasma frequency. In particular, the electron plasma frequency is the rate at which electrons tend to oscillate about the ions to maintain quasi-neutrality. This is a fundamental motion of plasmas and is ubiquitous to any and all regimes of a plasma. In the limit of infinite ion mass and ignoring electron thermal motion, the plasma frequency is given by:

$$\omega_{p,e} = \sqrt{\frac{n_e e^2}{m_e \epsilon_0}}, \tag{1.5}$$

where e is the standard electric charge. Since frequent collisions with neutral particles cause charged particles to behave hydrodynamically, rather than collectively, the plasma frequency need be larger than the neutral collision frequency, $\omega_{p,e} > \omega_c$, in order for collective effects to dominate.

Finally, the last characteristic parameter of a plasma is known as the Debye sphere, N_D. Collective behavior of a plasma requires that there are a sufficient number of particles to screen out an external charge. The Debye sphere is defined as: $N_D = n\frac{4}{3}\pi\lambda_D^3$. The number of particles within a Debye sphere must be much greater than one, $N_D \ggg 1$, in order for collective behavior to dominate. Therefore, if the following are satisfied:

$$\begin{cases} \lambda_D \ll L, \\ N_D \ggg 1, \\ \omega_{p,e} > \omega_c, \end{cases} \tag{1.6}$$

a collection of charged particles is a plasma. [19] It is important to note that special cases exist where a plasma locally violates these parameters, such as at plasma-solid boundaries when a plasma forms what is known as a *sheath*; nonetheless, these parameters provide a useful measure to determine the relative importance of collective effects.

A plasma under the influence of a magnetic field requires further characterization. Should the effect of a magnetic field be considered, another important parameter arises known as the Larmor radius:

$$r_L = \frac{mv_\perp}{|q_e|B}, \tag{1.7}$$

where B is the magnetic field strength and $v_\perp$ is the velocity perpendicular to the magnetic field. The Larmor radius describes the radius of gyration for a charged particle in a magnetic field. Since this quantity depends on the mass of the particle, electrons and ions have varying orbits for an identical magnetic field. This one example of the hierarchy of temporal and spatial scales for electrons and ions in a plasma represents a defining feature of plasma physics that will be important to various studies in this thesis. Partially attributable to this large range of spatiotemporal scales is the important and wide-spanning concept of *instability* in a plasma. In addition to macroscopic instabilities, such as those experienced by gases, plasmas may also be subject to microscopic, or kinetic, instabilities. In some cases, when an instability is allowed to grow in a plasma from some initial perturbation, the result is generation of plasma waves with a phase velocity characterized by a dispersion relation. These plasma waves may either be electrostatic (characterized by only electric field perturbation) or electromagnetic (characterized by a coupled electric and magnetic field perturbation) in nature. The subject of plasma instabilities will also be a key point of exploration in this thesis.

A final and important point is the distinction of various regimes of plasma. Plasma regimes are generally characterized by the number density and temperature of the plasma electrons. Low-temperature plasmas, the regime in which the plasmas convered in this thesis lie, generally have temperatures such that $T_e < 10^5$K. The density of the plasmas considered here lie in the middle of the plotted range in Figure 1.1, in the bubble labeled "Electric Propulsion," with Debye lengths in the range of 1μm$< \lambda_D <$ 1mm. Indeed, these plasmas are similar in nature to industrial plasmas used for material processing, but vary significantly from fusion plasmas which are of much higher temperature and density. The concepts of electric propulsion, a key technology motivating this thesis, will be detailed in the next section.

1.3 Spacecraft Electric Propulsion

Electric propulsion (EP) is a sub-field of spacecraft propulsion which utilizes electric energy applied to a propellant to generate thrust. This technology differs from conventional, chemical propulsion in that for chemical propulsion, the thrust energy

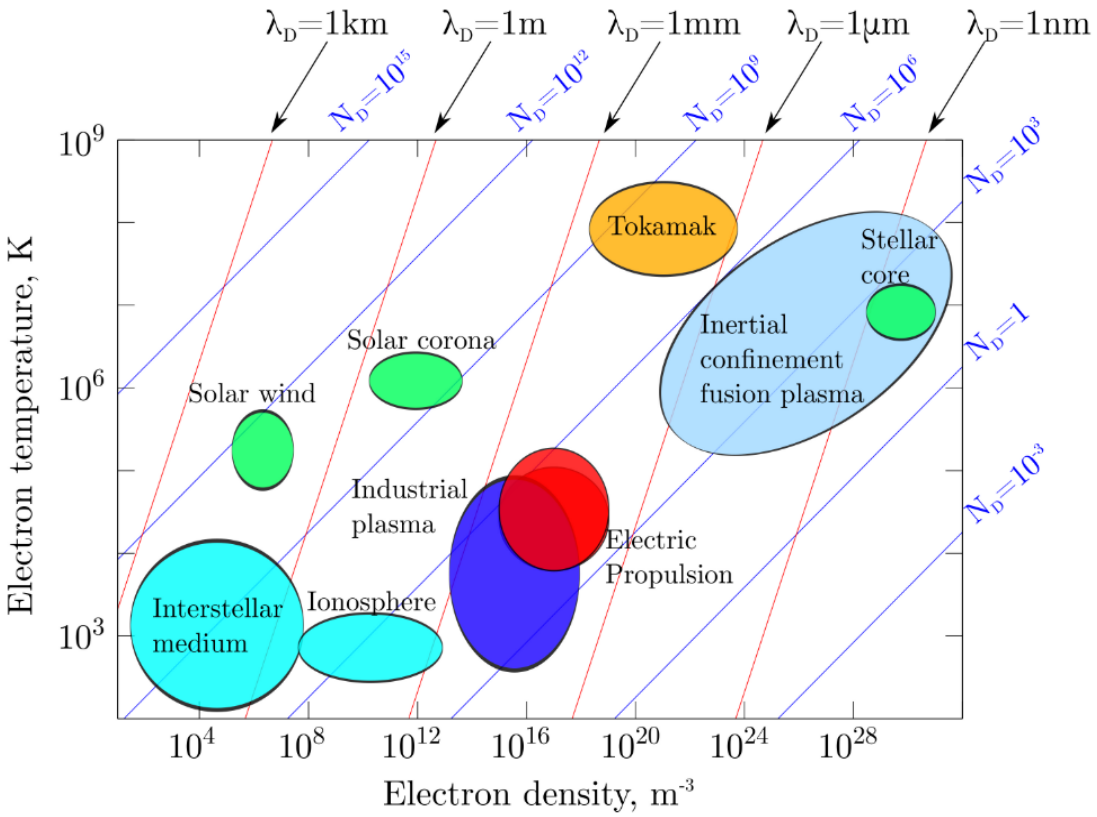

Figure 1.1: Various regimes of plasmas in the density-temperature space. The Debye length and Debye sphere parameters are given as reference. Reproduced from Ref. [46] with permission.

is harnessed from within the propellant, whereas in electric propulsion, energy is harnessed electrically. This electric energy may come from any type of in-space source, such as solar panels or nuclear reactors. Generally, EP thrusters produce significantly less thrust than their chemical counterparts, meaning that they may not be used to escape Earth's gravity but rather only once the craft is in-space. However, EPs advantage lies in its ability to generate large propellant exhaust velocities. The advantage of large exhaust velocities is clearly demonstrated by Tsiolkovsky's rocket equation, which gives the resultant delta-v for a particular thrust maneuver:

$$\Delta v = v_e \ln \frac{m_0}{m_f}, \tag{1.8}$$

where v_e is the exhaust velocity of the propellant, m_0 is the spacecraft mass before the maneuver and m_f is the mass after the maneuver.

Therefore, an efficient way to drive up the delta-v of a given maneuver is to increase the exhaust velocity of the propellant. EP is able to realize much larger exhaust velocities than chemical propulsion, meaning that less propellant mass is necessary to tackle an identical mission envelope. The exhaust velocity is often described in seconds by a quantity known as the specific impulse, $I_{sp} = \frac{v_e}{g}$, where g is the acceleration due to gravity. A typical mono- or bi-propellant chemical thruster has a specific impulse on the order of $200-400$s, whereas modern EP thrusters have an I_{sp} of $2000-4000$s. [73] EP devices are not without their pitfalls: for example, since their thrust is low, EP maneuvers may take much longer than their chemical counterparts; in many cases, however, this is an acceptable trade-off in order to save precious payload mass that must be launched into orbit.

There are three general types of electric propulsion systems: electrothermal, electrostatic, and electromagnetic. Electrothermal thrusters convert electric energy into heat in order to energize a propellant and achieve high exhaust velocities. Electrostatic thrusters utilize applied electric fields to accelerate propellant, and finally, electromagnetic thrusters utilize a combination of electric and magnetic fields to accelerate propellant. Several types of EP thrusters exist and have been flown on satellites, such as resistojets (electrothermal), gridded-ion thrusters, Hall-effect thrusters, electrospray thrusters (electrostatic). For satellite missions, these thrusters are often used for station-keeping (maintaining orbital altitude). While less common, there have also been deep-space missions that flew with EP systems: NASA's Deep Space 1 and Dawn missions (gridded-ion), ESA's Bepicolombo mission (gridded-ion), and NASA's upcoming Psyche mission (Hall-effect).

1.3.1 Ion and Hall Thrusters

Gridded-ion thrusters and Hall-effect thrusters utilize plasmas as their means of generating thrust. Figure 1.2 gives a schematic showing the fundamental components of ion and Hall thrusters. The basic operating principles of the gridded-ion thruster are as follows: a neutral gas is flowed into an ionization chamber, where by some process (often via a thermionic hollow cathode, which will be detailed in Subsection 1.3.2), the neutral gas is ionized. At the exit of the ionization chamber, a voltage drop is applied across two grids, causing the ions of the resulting plasma to be accelerated as they are extracted from the ionization chamber. A beam of ions exits the thruster and streams away, thus creating thrust. A device known as a thermionic hollow cathode generates a neutralizing stream of electrons to equalize the positive charge of the ion beam exiting the thruster, thereby avoiding a buildup of charge on the spacecraft.

For the Hall-effect thruster, the operating principles are quite different. At a positively biased anode, neutral gas is injected into an annular channel. Fixed concentric magnets create a radial magnetic field within this channel. A thermionic hollow cathode is placed outside of the channel and emits a current of electrons which stream towards the anode. However, when these electrons encounter the magnetic field within the channel, they are accelerated in the azimuthal direction (to circulate around the annular channel) and form what is known as the Hall current. This current of electrons serves to ionize the neutral gas which is flowing through the channel, ultimately creating a quasi-neutral plasma. While electrons are magnetized because their Larmor radius, r_L is smaller than the channel width, the plasma ions, being much more massive than the electrons, are effectively un-magnetized. Therefore, the applied electric field accelerates the ions out of the channel and thereby

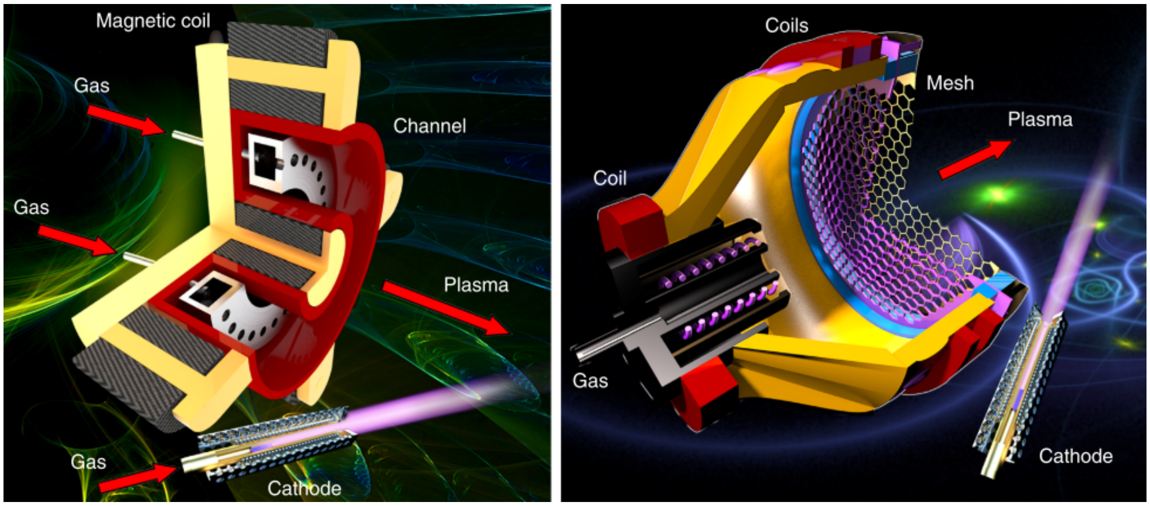

Figure 1.2: Schematic showing the basic components of a Hall-effect (left) and gridded-ion (right) thruster. Reproduced from Ref. [72] with permission.

creates thrust.

Ion thrusters and Hall thrusters have been in development for at least six decades; the first spacecraft ion thruster was flown by the United States in 1970, and the first spacecraft Hall thruster was flown in 1971 by modern-day Russia. [43] Considerable interest in these technologies and their efficiency for satellite station-keeping has resulted in a steady rise in EP-equipped spacecraft over the past several decades (see Figure 1.3). [71,72] A fundamental understanding of the physics driving the operation of these thrusters, however, has lagged behind their ever-expanding application. One of the chief limiting factors in advancing electric propulsion from a near-Earth orbit technology to a deep-space technology has been erosion of the thruster surfaces. For example, ions with sufficient energy to sputter the channel walls in a Hall thruster have posed a long-standing problem for their use in long duration deep space missions. [132] A major recent advance in Hall thruster technology has come in the form of magnetic shielding, where the magnetic field topology is shaped such that the field lines do not terminate on the channel walls; this technology has demonstrated a significant reduction in channel erosion. [86] However, magnetic pole-piece erosion

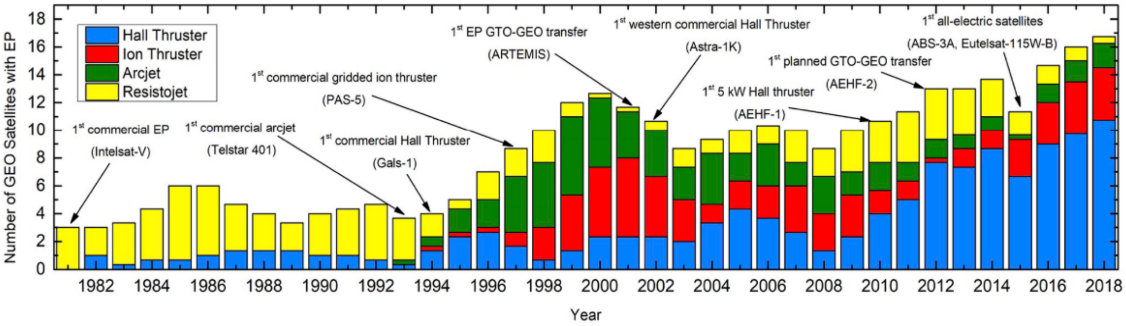

Figure 1.3: Number of geo-stationary satellite launches with EP from 1981 to 2018. Note the recent dominance of Hall-effect thrusters. Reproduced with permission from Ref. [71].

remains a challenge for these devices. [59] Ion thrusters, too, have been subject to erosion problems; in particular, erosion of the grid(s) of the thruster reduces the efficiency of the thruster and is a primary factor in determining thruster lifetime. [89]

For in-space operation, electric propulsion systems must reliably operate for thousands or even tens of thousands of hours. Flight qualification of a thruster thus requires continuous operation in a vacuum chamber for thousands of hours, requiring significant resources to construct, maintain, and operate. [55] Numerical simulation provides an attractive, complementary approach in the development of EP systems for many reasons. Perhaps most importantly, a well-posed simulation of a thruster operating for thousands of hours could potentially require significantly less resources than a full-scale experimental test campaign. Due to the complexity of these systems, however, this *predictive* EP modeling remains elusive. Before predictive modeling may be realized, the entirety of the dominant physics of the thrusters must be understood; fortunately, in this realm simulation also provides a crucial complement to experiment and theory. With these obstacles in mind, this thesis aims to apply simulation to both drive an understanding of the physics and push towards predictive modeling of the hollow cathode device.

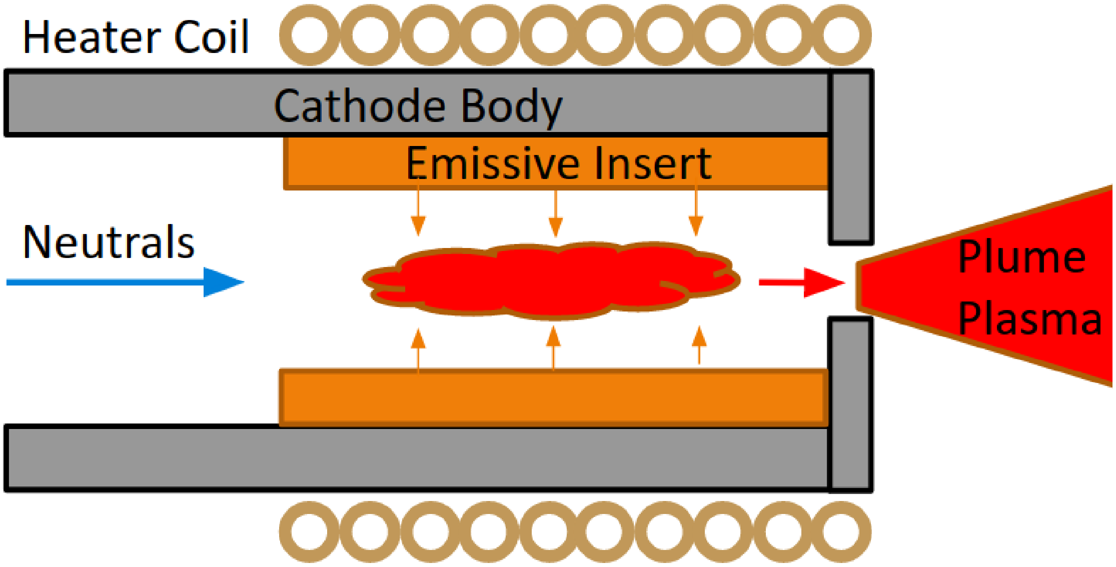

Figure 1.4: Cartoon demonstrating hollow cathode operation. Often, a keeper is placed around the cathode in order to shield it from ion bombardement and aid lighting the discharge.

1.3.2 Thermionic Hollow Cathodes

A common thread linking gridded-ion thrusters and Hall-effect thrusters is the thermionic hollow cathode. This device takes advantage of the phenomenon of thermionic emission, whereby an emissive material "boils off" electrons when sufficiently energized (this material is often chosen to be barium oxide or lanthanum hexaboride due to their favorable work function, ϕ_w, which determines the energy necessary to emit electrons). This energy is initially supplied in the form of heat by heater coils wrapped around the cathode body. The propellant gas, often xenon, is flowed through the cathode body where it encounters the emitted electrons and ionizes. The resulting quasi-neutral plasma then expands through an orifice at the end of the cathode body and into the plume. Figure 1.4 gives a simple cartoon demonstrating the hollow cathode operating principles.

The hollow cathode plasma often serves multiple purposes. In the case of the gridded-ion thruster, two hollow cathodes are often used: one serves to sustain the discharge plasma while the other serves to neutralize the resulting ion beam. In Hall-effect thrusters, one hollow cathode is used which serves to both sustain the discharge and neutralize the ion beam. As with the overall thruster systems, the physics of the hollow cathode itself is still in the process of being understood. Energetic ion bombardment of the plume-facing cathode body necessitates the use of a *keeper*, which is essentially a shield that encloses the cathode to protect it from ion sputtering. Despite this protection, cathode keeper erosion has proven to be problematic and a life-limiting factor for gridded-ion thruster operation. [26] The physics driving high-energy ion production was for a time unknown, but proposed mechanisms included the presence of multiply charged ions [33, 131] and a 'double layer'-type structure outside the cathode orifice [81]. Later numerical investigations, however, found that the conditions in the hollow cathode plume favored the growth of a plasma instability known as the ion-acoustic instability; [83] as this instability is capable of generating high-energy ions, it arose as a possible source of the eroding ions in the plume. Later experimental measurements confirmed the existence of ion-acoustic waves, which are spawned by this instability. [62]

The ion-acoustic instability is a kinetic instability, meaning that it cannot be captured by a fluid description of the plasma. However, most existing numerical efforts to model the hollow cathode utilize multi-fluid descriptions because these approaches have the distinct advantage of being significantly less computationally costly than kinetic methods. In order to incorporate the effects of the ion-acoustic instability, closure models have been introduced into fluid simulations that have improved agreement with experimental measurement. [83, 94, 112] There are important limitations to such an approach; for example, the efficacies of the applied closure models for the ion-acoustic instability have not been investigated for a xenon plasma with conditions relevant to the hollow cathode plume. As these closure models are derived using certain assumptions, it is important to evaluate them for their particular application to the hollow cathode plume; this may only be done through either experimental measurement or kinetic simulation.

Further, while a multi-fluid description may include the effect of anomalous resistivity or heating caused by the instability, it inherently cannot capture the *non-Maxwellian* nature of the particle VDFs driven by the instability. Recent attempts to develop a hybrid-kinetic particle-in-cell (PIC) simulation (with kinetic ions and fluid electrons) demonstrated the use of an ion-heating model driven by the ion-acoustic instability. [67, 68] This type of approach has the advantage of enabling sputtering predictions due to non-Maxwellian ion populations while keeping the benefit of low computational cost by using a fluid electron model. Assuming that such an ion heating model is well-posed and experimentally validated, it would provide a relatively low-cost option with the capability to predict erosion rates. In this thesis, this type of hybrid approach is adopted in order to provide an engineering-level tool to better understand hollow cathode operation, with the intent to eventually produce a predictive hollow cathode model.

The ion-acoustic instability, which occurs when a plasma carries a net current, is known to generate high-energy ion tails which are non-Maxwellian; these tails may prove to be important in assessing cathode erosion. [76] A recent numerical investigation into cathode keeper erosion found that back-streaming ion tails are indeed formed for such a current-carrying plasma, yet to observe non-negligible tails the current level had to be driven beyond that of the ion-acoustic instability and into the regime of another instability, the Buneman instability. [49] This finding challenges the commonly accepted notion of the ion-acoustic instability's sole role in driving cathode keeper erosion. However, notably these simulations were carried out in 1D; previous numerical studies of the ion-acoustic instability have demonstrated that the nature of the instability's saturation (the process by which the instability stops growing) differs significantly in higher dimensions. [6]

Additionally, previous experimental erosion estimates based on measured plasma potential fluctuation levels found agreement with measured erosion rates, yet these fluctuation levels were in excess of those expected by the ion-acoustic instability. [21,84] This finding highlights another important aspect of the hollow cathode plume plasma: the existence of two operational modes known as the spot and plume modes. The plume mode is characterized as an unfavorable regime where low-frequency oscillations arise in the plasma and erosion rates are measurably enhanced compared to the nominal, quiescent spot mode. Recent numerical and experimental work has identified that the plume mode is an ionization-type oscillation which is driven by the enhanced resistivity of the ion-acoustic instability. [38, 87] Therefore, the ion-acoustic instability may drive cathode keeper erosion both through triggering an ionization-type oscillation and by driving high-energy ions through interaction with ion-acoustic wave potentials. In the spot mode, low-frequency ionization oscillations are absent and thus erosion may be chiefly dictated by high-energy ion formation through the ion-acoustic instability, whereas in the plume mode the erosion may be influenced by the interplay of both processes.

In order to address the question of keeper erosion due to high-energy ion formation by the ion-acoustic instability, which may be important in both the spot and plume mode, the use of a fully-kinetic simulation approach provides an important piece to the puzzle. This is because fully-kinetic simulations may directly capture the growth of the plasma waves and their interaction with the ions which leads to high-energy tail formation. Therefore, this thesis sets out to utilize both hybrid-kinetic and fully-kinetic analyses of the current-carrying hollow cathode plasma to approach the problem of keeper erosion and achieving predictive simulation from multiple avenues.

1.4 Research Objectives

In light of the necessity to explore the properties of inherently kinetic current-carrying instabilities with plasma conditions relevant to the hollow cathode plume, this thesis sets out to accomplish the following:

- Develop and verify a 2D-axisymmetric kinetic simulation framework for analysis of the hollow cathode system to ultimately provide a predictive simulation capability.
- Implement new physical models into the kinetic simulation framework, such as collisions, to better capture the hollow cathode plasma.
- Validate the 2D-axisymmetric solver with experimental hollow cathode data.
- Analyze the ion-acoustic instability with properties relevant to the cathode plume plasma and evaluate the efficacy of a closure model(s) used in multi-fluid hollow cathode codes.
- Investigate the nonlinear behavior of plasmas subject to current-carrying instabilities in order to better understand saturation processes and particularly the production of high-energy ions important to cathode keeper erosion.
- Extend the numerical investigation of current-carrying instabilities to two-dimensions in order to observe how this saturation differs compared to one-dimensional studies.

1.5 Thesis Outline

In this thesis, the deterministic-kinetic method is applied to a variety of gas and plasma dynamics problems which are of interest to the electric propulsion discipline. The layout of the thesis is as follows: in Chapter II, the numerical methods used to study the various problems in the thesis are detailed. In Chapter III, the problem of gas and plasma expansion flows is considered. In this chapter, a study is conducted to verify kinetic results and benchmark performance with an existing kinetic method, known as direct-simulation Monte Carlo, using analytic solutions of a neutral gas expansion; this is followed by the 2D-axisymmetric solver's application to a hollow cathode geometry, where it is verified and validated with experimental data. Chapter IV presents an investigation of plasma current-carrying instabilities via fully-kinetic DK simulations. Both one-dimensional and two-dimensional simulations of the ion-acoustic and Buneman instabilities are considered. In Chapter V, the appearance of a nonlinear phenomenon as a result of the ion-acoustic instability, the plasma double layer, is investigated via one-dimensional, fully-kinetic simulation. Finally, Chapter VI lays out the findings of this thesis and provides avenues for future work.

CHAPTER II

Numerical Methods

In this chapter, the details of the numerical methods used in this study are given in detail. First, Section 2.1 gives a general overview of what kinetic methods are and to what situations they are applied. Section 2.2 details the stochastic particle method known as direct-simulation Monte Carlo (DSMC) which is applied to neutral gas flows. Section 2.3 details the deterministic- or direct-kinetic (DK) method which is primarily used in the simulations detailed in this thesis, both for neutral and charged particle cases. Sections 2.4 and 2.5 detail the implementation of Maxwell's equations and collision modeling, which are coupled to the DK simulation framework. Finally, Section 2.6 gives a variety of cases used to verify the various solvers implemented in this thesis.

2.1 Kinetic Methods Overview

Kinetic theory utilizes a detailed understanding of molecular behavior to build a macroscopic description of gas properties. This field is rooted in the understanding that any gas is characterized by a distribution of particles f over velocity space v, where $f(\mathrm{v})$ is known as the velocity distribution function (VDF). By avoiding simplifying assumptions, kinetic theory provides an exact description of a dilute gas' properties. The Boltzmann equation describes, most generally, the evolution of a dilute gas in physical, velocity and temporal space, otherwise known as phase space $(\mathrm{x}, \mathrm{v}, t)$:

$$\frac{\partial f}{\partial t} + \mathrm{v} \cdot \frac{\partial f}{\partial \mathrm{x}} + \mathrm{a} \cdot \frac{\partial f}{\partial \mathrm{v}} = \frac{\partial f}{\partial t}_{collisions}, \tag{2.1}$$

where the left-side terms describe advection in time, space, and velocity, respectively, and the right-side term accounts for the effect of inter-molecular collisions. This equation represents the most exact description of gas motion. However, direct solution of this equation is very computationally costly, and therefore simplifying assumptions are often made to reach the well-known Euler and Navier-Stokes equations of fluid dynamics.

To reach the Euler equations, one must assume infinite collisionality and thus a state of equilibrium everywhere in the gas. To reach the Navier-Stokes equations, on the other hand, one may assume small perturbations from equilibrium in what is known as the Chapman-Enskog expansion. [126] However, the assumptions of these well-known equations of fluid dynamics break down in limits such as those of zero collisionality (rarefied flow) or large perturbations from equilibrium (non-equilibrium). In these cases, one must return to a more complete, kinetic description of the gas.

Even when considering cases where the Euler and Navier-Stokes equations break down, the exact form of the collision term in Equation 2.1 is quite complex, both analytically and numerically. Approximations are often used to reduce this complexity: for example, in the limit of no collisions, the right-side is zero and the Boltzmann equation reduces to the Vlasov equation:

$$\frac{\partial f}{\partial t} + \mathrm{v} \cdot \frac{\partial f}{\partial \mathrm{x}} + \mathrm{a} \cdot \frac{\partial f}{\partial \mathrm{v}} = 0. \tag{2.2}$$

The Vlasov equation (2.2) is valid when the effect of collisions is negligible, such as in low-density plasmas and free-molecular gas flows. As this expression makes no assumptions on the state of the VDF, it is still able to capture non-equilibrium behavior. In the cases of dilute gas or plasma flows with highly non-equilibrium velocity distributions, there exist a variety of options for simulation of the Boltzmann and/or Vlasov equations. Two important examples of these kinetic simulation methods are described in this chapter: the direct-simulation Monte Carlo method and the deterministic-kinetic method.

2.2 DSMC: A Stochastic Method

A common approach to simulation of the Boltzmann equation is through particle methods. Particle methods are Lagrangian in nature, tracking individual particles through a computational domain in physical space. Two popular methods are the DSMC [4] and particle-in-cell (PIC) [5] methods, both of which have demonstrated great success in the fields of gas and plasma dynamics, respectively. Notably, PIC is better described as a semi-Lagrangian method, as properties of the particle distributions are interpolated to grid points and the electric and magnetic fields are then calculated there.

In this thesis, a particular focus is placed on the DSMC method, as it is repeatedly used for benchmarking and verification of the DK method. The DSMC code MONACO, developed in the Non-equilibrium Gas and Plasma Dynamics (NGPDL) group, is used for this purpose. [23] The DSMC method makes use of statistical units known as macroparticles, which are taken to represent a collection of real particles assumed to have identical properties. At each time in the DSMC simulation, particles are advanced in space according to their velocity v:

$$\frac{\mathrm{dx}}{\mathrm{dt}} = \mathrm{v}. \tag{2.3}$$

If any external forces are considered, the velocity is first updated according to the acceleration a:

$$\frac{\mathrm{dv}}{\mathrm{dt}} = \mathrm{a}. \tag{2.4}$$

At each time step, collisions may or may not be evaluated. DSMC often assumes that *binary* collisions between molecules are dominant, and therefore focuses solely on this type of collisions. There exist many methods to simulate such collisions, yet the No-Time-Counter (NTC) scheme is popular and used by MONACO. [4] This scheme calculates the probability of collision, P, in a particular cell via:

$$P = F_N V_{S,max}/V_C, \tag{2.5}$$

where F_N is the number of real particles simulated by a single macroparticle, $V_{S,max}$ is the volume swept by two molecules moving at the relative speed between them, and V_C is the numerical cell volume. With this expression, the number of colliding pairs in a particular time step is found by:

$$N_{pairs} = \frac{1}{2} N \bar{N} V_{S,max}/V_C, \tag{2.6}$$

where N is the instantaneous number of macroparticles in the cell and $\bar{N}$ is the time-averaged number of macroparticles in the cell. A collision probability is evaluated for each of these pairs, and for those which experience a collision the post-collision state is determined through conservation of momentum and energy. In the limiting case of a single specie of atoms (which have no internal energy modes such as rotation or vibration) the collision may be assumed elastic, e.g. all energy is kept in the translational mode. After collisions are assessed, particle interactions with boundary conditions are calculated. In MONACO, various boundary conditions have been implemented; those used in this study are:

- Inflow: particles are injected to the boundary cells according to a prescribed density, temperature, and bulk velocity,
- Outflow: particles which cross the boundary plane are removed from the simulation,
- Symmetry: particles which would cross the boundary plane are re-introduced to the simulation with velocity coordinates normal to the plane reflected,
- Wall: particles which would cross the boundary plane are reflected either specularly (elasticly), diffusely (where the particle takes on a new velocity characterized by the temperature of the wall), or a combination of both, depending on the specified accommodation coefficient.

Finally, the macroscopic properties of the gas, such as number density n, temperature T, and bulk velocity U may be found through averages of the macroparticle properties. Constructing a histogram of the aggregate particle velocities amounts to the VDF of the gas in every physical cell, where the resolution of this VDF depends on the number of particles per cell. Figure 2.1 gives a representative sketch of the system of macroparticles in DSMC and how a sampling of particle properties in a given cell reconstructs the VDF. There are a variety of numerical constraints which must be followed in order to ensure the DSMC solution is numerically valid:

- The number of particles per cell, N_p, must be sufficiently large. A common heuristic is that $N_p \geq 20$.

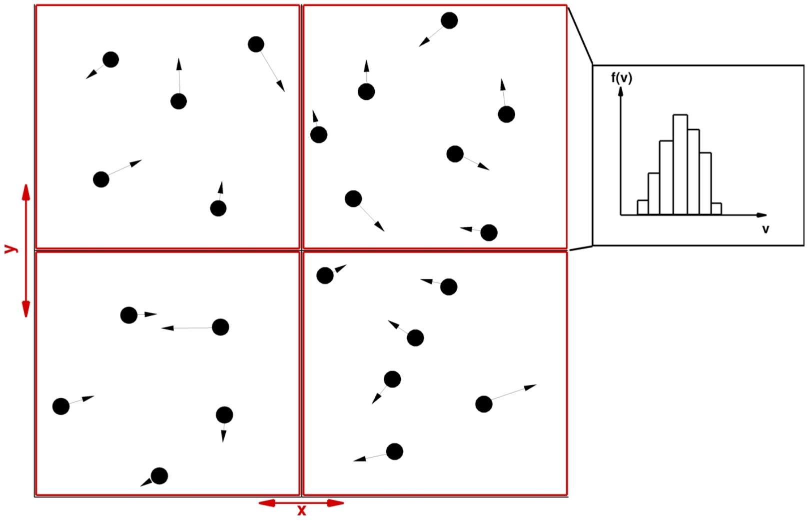

Figure 2.1: Sketch of a 2D DSMC simulation, with a representative grid, with a sampling of the particle properties from the top-left cell and the resulting reconstructed VDF.

- The time step is sufficiently small, such that it is smaller than the mean collision time $\Delta t < \tau_{coll}$.
- The cell size is smaller than the mean free path at any point in the domain, $\Delta x < \lambda$.

The use of macroparticles and the statistical nature of evaluating collisions allows the DSMC method to simulate flows with relatively low computational expense, but also introduces an important limitation to the scheme: statistical error. Statistical error is inherent to DSMC due to the use of macroparticles and a statistical collision algorithm. In order to drive down statistical error, an ensemble-average of multiple simulations (in the case of an unsteady system) or time averaging over multiple sampling steps (in a steady system) may be taken. However, even when all of the above conditions are met, statistical error is important to consider when evaluating the results of stochastic methods, as it may prevent resolution of fine-scale VDF perturbations or even introduce un-physical oscillations into the system. [103]

2.3 DK: A Deterministic Method

Another class of kinetic simulation methods solve the Boltzmann equation directly via an Eulerian approach, here called the DK method. In these methods, both physical and velocity space are discretized, and the Boltzmann equation is solved using, in this case, a finite-volume method with a hyperbolic scheme. Thus, these methods are not statistical in nature but rather are deterministic. At each physical location x, the VDF is represented by a velocity grid. Figure 2.2 gives a representation of the phase space grid. It should be noted that in actuality, the x and v coordinates are independent and would result in a 4D grid; this figure is only meant to help represent the storage of information for the DK scheme. At each velocity cell boundary and each physical cell boundary, a flux is calculated according to the Boltzmann equation. Thus, the distribution function f is the dependent variable which is advected through the domain.

2.3.1 Existing Numerical Schemes

The code used in these studies was originally developed at the University of Michigan, [46] and has been under active development since. [103] In the finite-volume method used here, a flux-limited scheme is used which reverts to first-order accuracy in order to prevent spurious numerical oscillation near sharp gradients [39], while attempting to achieve second-order accuracy otherwise. The scheme used is known as the Monotonic Upwind Scheme for Conservation Laws, or MUSCL. [122] Numerical fluxes, F, are calculated according to the following expression:

$$F^{+}_{i-1/2} = cf_{i-1} + \frac{(1-c)|c|}{2}(f_i - f_{i-1})\Psi(r_{i-1/2})r_{i-1/2}, \tag{2.7}$$

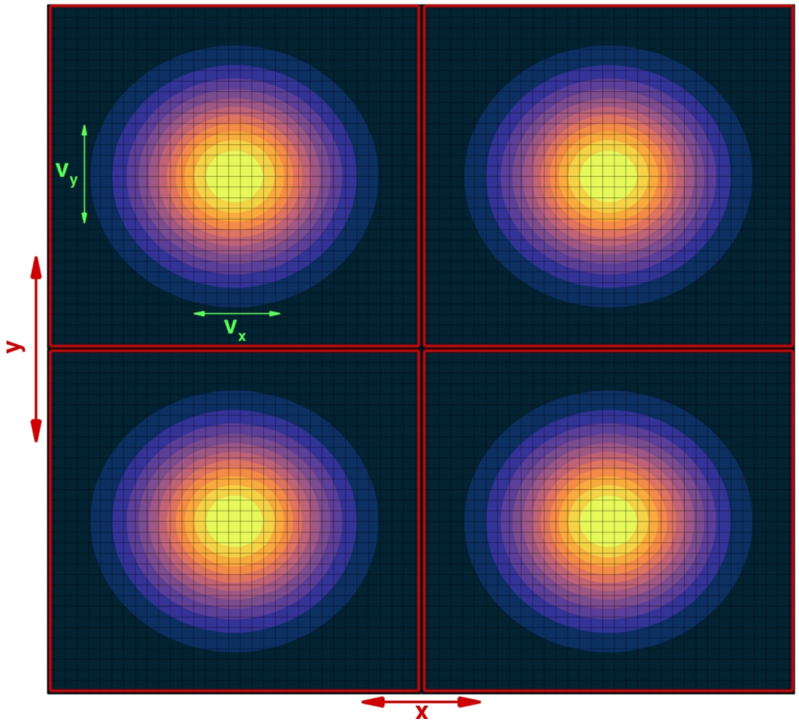

Figure 2.2: 2D2V DK simulation domain example. The VDF is represented at each physical cell (x, y) by an independent grid of velocity cells (v_x, v_y).

where c is the Courant-Friedrichs-Lewis (CFL) number, Ψ is the flux-limiter function, and r is the ratio of gradients in the solution. The subscript i refers to the location of f in physical or velocity space, depending on the flux being evaluated. The ratio of gradients, r, is defined as:

$$r_{i-1/2} = \frac{f_{i-1} - f_{i-2}}{f_i - f_{i-1}}, \tag{2.8}$$

and is used to determine the 'smoothness' of the function at a particular location. Based on this value, the flux limiter Ψ is then determined; a variety of choices are available for this function, though they must satisfy certain conditions. For example, the limiter function must go to zero when the ratio of gradients does, e.g. $\Psi(0) = 0$, and go to one when the ratio of gradients is one, $\Psi(1) = 1$. These properties ensure the solver is total-variation-diminishing (TVD), or that it tends to drive down the level of numerical oscillation. Thus, when $\Psi(0) = 0$, the scheme reduces to first-order accuracy. Figure 2.3 gives the Sweby diagram, which compares various limiter functions Ψ with the gradient ratio r. The harmonic, superbee, [105] and Arora-Roe [1] limiter functions are given for comparison with the function developed for the present DK scheme, a modified Arora-Roe limiter. [46] The modified Arora-Roe limiter has the following properties:

$$\Psi(r) = \begin{cases} 0 & r < 0, \\ \min(2r, \Psi(r)) & 0 \leq r < 1, \\ \min(2, \Psi(r)) & r \geq 1. \end{cases} \tag{2.9}$$

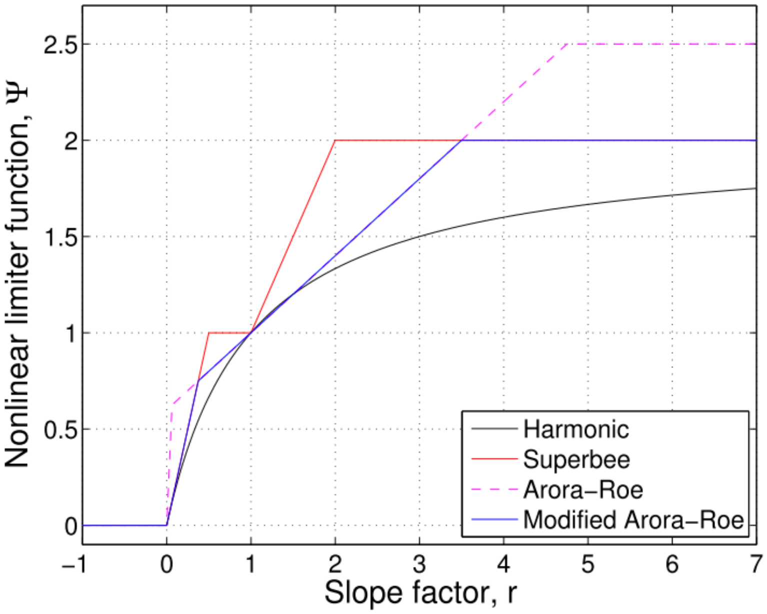

Figure 2.3: Sweby diagram demonstrating the properties of various flux-limiter functions, $\Psi(r)$, including that used in this study, the modified Arora-Roe limiter. Reproduced from Ref. 46.

Temporal advance is accomplished via explicit methods of varying orders of accuracy. The simplest first-order scheme, explicit Euler, is given by:

$$f^{n+1}(\mathrm{x}, \mathrm{v}) = f^n(\mathrm{x}, \mathrm{v}) + \Delta t D(f^n, \mathrm{x}, \mathrm{v}), \tag{2.10}$$

where $D(f^n, \mathrm{x}, \mathrm{v})$ is the total derivative of f with respect to x and v. If higher order accuracy is desired, Runge-Kutta (RK) schemes may be applied. RK schemes utilize intermediate values of the function to generate higher-order accurate solutions; for example, in second-order or RK2:

$$f^{int}(\mathrm{x}, \mathrm{v}) = f^n(\mathrm{x}, \mathrm{v}) + \Delta t D(f^n, \mathrm{x}, \mathrm{v}), \tag{2.11}$$

and

$$f^{n+1}(\mathrm{x}, \mathrm{v}) = f^n(\mathrm{x}, \mathrm{v}) + \frac{\Delta t}{2}(D(f^n, \mathrm{x}, \mathrm{v}) + D(f^{int}, \mathrm{x}, \mathrm{v})). \tag{2.12}$$

Since the temporal schemes used are explicit, a CFL condition must be satisfied to ensure stability. For explicit Euler, the CFL condition is $c \leq 1$; RK schemes extend the region of stability. The CFL number is defined differently based on the flux being considered. In the case of spatial flux, the CFL number is defined as $c = v\Delta t/\Delta x$, where in the case of velocity flux the number is defined as $c = a\Delta t/\Delta v$. Therefore, for the explicit Euler method, the total CFL condition c_{tot} which must be respected in the code is:

$$c_{tot} = \left(\frac{\max|\mathrm{v}|\Delta t}{\Delta \mathrm{x}} + \frac{\max|\mathrm{a}|\Delta t)}{\Delta \mathrm{v}} \right) \leq 1 \tag{2.13}$$

In order to evaluate the macroscopic quantities of the gas or plasma from the VDF, moments of the distribution are taken. The zeroth moment:

$$n = \int_{\infty}^{\infty} f(\mathrm{x}, \mathrm{v}) d\mathrm{v}, \tag{2.14}$$

is used to find the number density, while the first moment:

$$\langle U \rangle = \int_{\infty}^{\infty} \mathrm{v}\hat{f}(\mathrm{x}, \mathrm{v}) d\mathrm{v}, \tag{2.15}$$

is used to find the drift velocity, and the second moment:

$$\langle U^2 \rangle = \int_{\infty}^{\infty} \mathrm{v}^2 \hat{f}(\mathrm{x},\mathrm{v}) d\mathrm{v}, \tag{2.16}$$

is useful for finding information such as the temperature:

$$T = \frac{m}{Nk_b}(\langle U^2 \rangle - \langle U \rangle \langle U \rangle), \tag{2.17}$$

where the normalized distribution is found by: $\hat{f}_n = f_n/n_n$. In practice, these integrals must be evaluated numerically, with the continuous integral being replaced by a discrete one. For example, the zeroth moment becomes:

$$n = \sum_{v_{min}}^{v_{max}} f(\mathrm{x},\mathrm{v}) V, \tag{2.18}$$

where V is the velocity cell volume defined by $V_1 = \Delta v_x$ in 1V, $V_2 = \Delta v_x \Delta v_y$ in 2V, and $V_3 = \Delta v_x \Delta v_y \Delta v_z$ in 3V. As it is impossible to represent all of velocity space, the infinite limits of the continuous integral have been replaced with the discrete limits of v_{min} and v_{max}. Indeed, in order to capture the relevant information contained in the VDF, care must be taken to ensure these velocity boundaries are sufficiently large so as not to truncate the VDF. However, a balance must be struck, as larger velocity boundaries create a larger domain and thus larger computational expense.

Due to the necessity of simulating a spatial and a velocity (phase space) grid, the DK method is computationally intensive. In order to mitigate this expense, the DK code is parallelized via the Message Passing Interface (MPI). MPI launches simultaneous threads at runtime which communicate with each other to exchange information. The parallelization scheme of the DK code is to divide the domain based on the physical axial location, such that each thread holds information for an identical number of axial cells. Thus, each thread also holds information for the entire velocity grid located at each physical cell. In most cases considered within this thesis, the DK code is run in parallel on a supercomputer cluster which holds a very large number of CPU nodes. Both the Great Lakes cluster at the University of Michigan and the Summit cluster at the University of Colorado have been utilized in this thesis. For both clusters, the Slurm job scheduling language is used to launch and run these jobs. [133]

2.3.2 2D-Axisymmetric Solver

Previous iterations of the DK code have been applied to both 1D1V and 2D2V domains for both fully- and hybrid-kinetic modeling. [46, 103] In order to approach hybrid-kinetic modeling of the hollow cathode in this work, a new functionality is added to the DK code: the ability to run 2D-axisymmetric (2D-AXI) simulations, which are 2D3V. Previous DK simulations of, for example, Hall thruster channels have been able to demonstrate that 2D2V is sufficient when the solution is not near the centerline ($r = 0$). [103] This situation changes, however, for the case of center-mounted hollow cathodes as the solution is desired near $r = 0$ and therefore necessitates three-dimensional resolution in velocity space.

In order to accomplish this task, it is necessary to convert the full 3D3V Boltzmann equation in Cartesian (x, y, z, v_x, v_y, v_z) coordinates:

$$\frac{\partial f}{\partial t} + v_x \frac{\partial f}{\partial x} + v_y \frac{\partial f}{\partial y} + v_z \frac{\partial f}{\partial z} + a_x \frac{\partial f}{\partial v_x} + a_y \frac{\partial f}{\partial v_y} + a_z \frac{\partial f}{\partial v_z} = \frac{\partial f}{\partial t}_{collisions}, \tag{2.19}$$

to cylindrical $(z, r, \theta, v_z, v_r, v_\theta)$ coordinates. Such a transformation results in the following expression [128]:

$$\frac{\partial f}{\partial t} + v_z \frac{\partial f}{\partial z} + v_r \frac{\partial f}{\partial r} + \frac{v_\theta}{r} \frac{\partial f}{\partial \theta} + a_z \frac{\partial f}{\partial v_z} + \left(a_r + \frac{v_\theta^2}{r}\right) \frac{\partial f}{\partial v_r} + \left(a_\theta - \frac{v_\theta v_r}{r}\right) \frac{\partial f}{\partial v_\theta} = \frac{\partial f}{\partial t}_{collisions}. \tag{2.20}$$

For a 2D-AXI geometry, one assumes that there is no dependence of the dependent variable f on spatial position in θ, which yields:

$$\frac{\partial f}{\partial t}+v_z\frac{\partial f}{\partial z}+v_r\frac{\partial f}{\partial r}+a_z\frac{\partial f}{\partial v_z}+\left(a_r+\frac{v_\theta^2}{r}\right)\frac{\partial f}{\partial v_r}+\left(a_\theta-\frac{v_\theta v_r}{r}\right)\frac{\partial f}{\partial v_\theta}=\frac{\partial f}{\partial t}_{collisions}. \tag{2.21}$$

Equation 2.21 is applied to charged particles in the hybrid-kinetic, 2D-AXI problems addressed in this thesis.

Notably, additional acceleration terms have been introduced by the coordinate transform. These terms are the centrifugal acceleration, $\frac{v_\theta^2}{r}$, and the Coriolis acceleration, $\frac{v_\theta v_r}{r}$, and the implication of these terms is that a flux in velocity space must be evaluated even in the absence of any outside forcing: $(a_z, a_r, a_\theta) = (0, 0, 0)$. This flux calculation introduces additional numerical error into the system, which may cause an initially equilibrium distribution to distort. [129] Should there be no outside forcing, which is often true for neutral particles but not true for charged particles due to the Lorentz force, one may take advantage of the fact that the centrifugal and Coriolis forces act in a circular manner by introducing new variables (ξ, ω) and using the coordinate transformation $(v_r, v_\theta) = (\xi\cos(\omega), \xi\sin(\omega))$. [120] From here, the 2D-AXI Boltzmann equation in conservative form, with no outside forcing, is:

$$\frac{\partial rf}{\partial t}+v_z\frac{\partial rf}{\partial z}+\xi\cos(\omega)\frac{\partial rf}{\partial r}-\xi\frac{\partial(\sin(\omega)f)}{\partial\omega}=\frac{\partial rf}{\partial t}_{collisions}, \tag{2.22}$$

where the centrifugal and Coriolis forces are combined into a single coordinate-transform flux, $\xi D(\sin(\omega)f)$.

For this equation, care must be taken in choice of the scheme to evaluate the coordinate-transform flux. In Ref. 79, a variety of schemes are proposed and tested, finding that the T-UCE scheme has the most effective balance of accuracy and favorable conservation properties. The T-UCE scheme is an upwinded scheme given by:

$$D(\sin(\omega)f) = \frac{1}{2\sin(\Delta\omega/2)}\bigg((\sin\omega_{i+1/2})^+ f_{i+1} + (\sin\omega_{i+1/2})^- f_i - (\sin\omega_{i-1/2})^+ f_i - (\sin\omega_{i-1/2})^- f_{i-1}\bigg), \tag{2.23}$$

where $a^\pm$ denotes $\frac{1}{2}(a \pm |a|)$ and $\omega_{i\pm1/2}$ denotes $\omega_i \pm \frac{\Delta\omega}{2}$. This scheme has the favorable attributes of preserving positivity, conserving mass, axial momentum and energy, and dissipating entropy. This scheme is used in Equation 2.22, which is applied to neutral flows for 2D-AXI problems addressed in this thesis.

This cylindrical coordinate scheme takes advantage of the fact that, in combination, the characteristic curves of the coordinate transform forces are circular. [79] Figure 2.4 demonstrates the circular action of these forces in combination. However, charged particles do not equally benefit from this coordinate transform due to the action of the Lorentz force (electric and magnetic fields) on them. Therefore in this thesis, the ion scheme represents the velocity grid using a Cartesian coordinate space, while the neutral scheme represents the grid with a cylindrical coordinate space. To demonstrate the efficacy of the cylindrical representation and associated T-UCE flux scheme, the conservation of energy is tracked for an initially equilibrium (Maxwellian) xenon gas at $T = 300$ K in a 1D3V domain. The boundary conditions in physical space are set to be specular walls, while the axial, radial, and azimuthal velocity space boundaries are set to $v_b = \pm 4.3 v_{th}$ such that the VDF value is negligible near the boundaries. Time is advanced with a first-order explicit Euler scheme; the time step is set to $\Delta t = 10$ ns and the simulation is run for a total of 0.5 ms.

Tables 2.1 and 2.2 give the number of grid points used to represent the computational domain. While not explicitly plotted here, it was first verified that all six

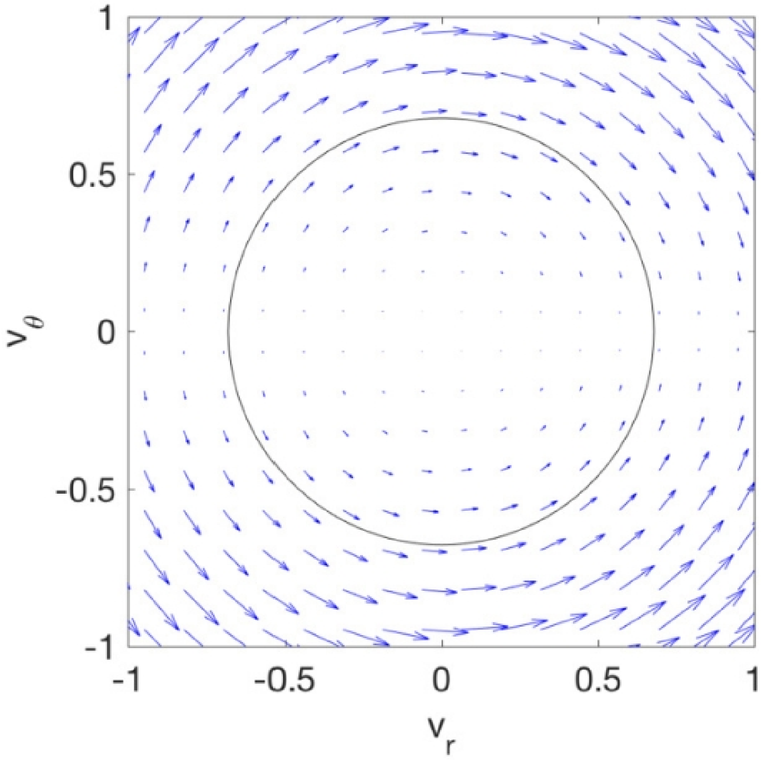

Figure 2.4: A sketch demonstrating the relative magnitude of the centrifugal and Coriolis accelerations in the v_θ-v_r plane. A circle is overlaid to demonstrate the circular characteristic curve of these accelerations in combination. Reproduced with permission from Ref. [129].

Case Name	Cartesian	rx1	rx2	rv1	rv2
$\boldsymbol{N_R}$	5	10	20	5	5
$\boldsymbol{N_{VR}}$	24	24	24	48	120
$\boldsymbol{N_{VT}}$	24	24	24	48	120

Table 2.1: Cartesian mesh discretization for the 2D-axisymmetric scheme energy conservation comparison.

Case Name	Cylindrical
$\boldsymbol{N_R}$	5
$\boldsymbol{N_\xi}$	24
$\boldsymbol{N_\omega}$	60

Table 2.2: Cylindrical mesh discretization for the 2D-axisymmetric scheme energy conservation comparison.

cases preserve the total number of particles in the system. Figure 2.5 tracks the conservation of energy during the simulation for all six cases. The Cartesian scheme does not preserve the system energy, and in the baseline case the gas temperature

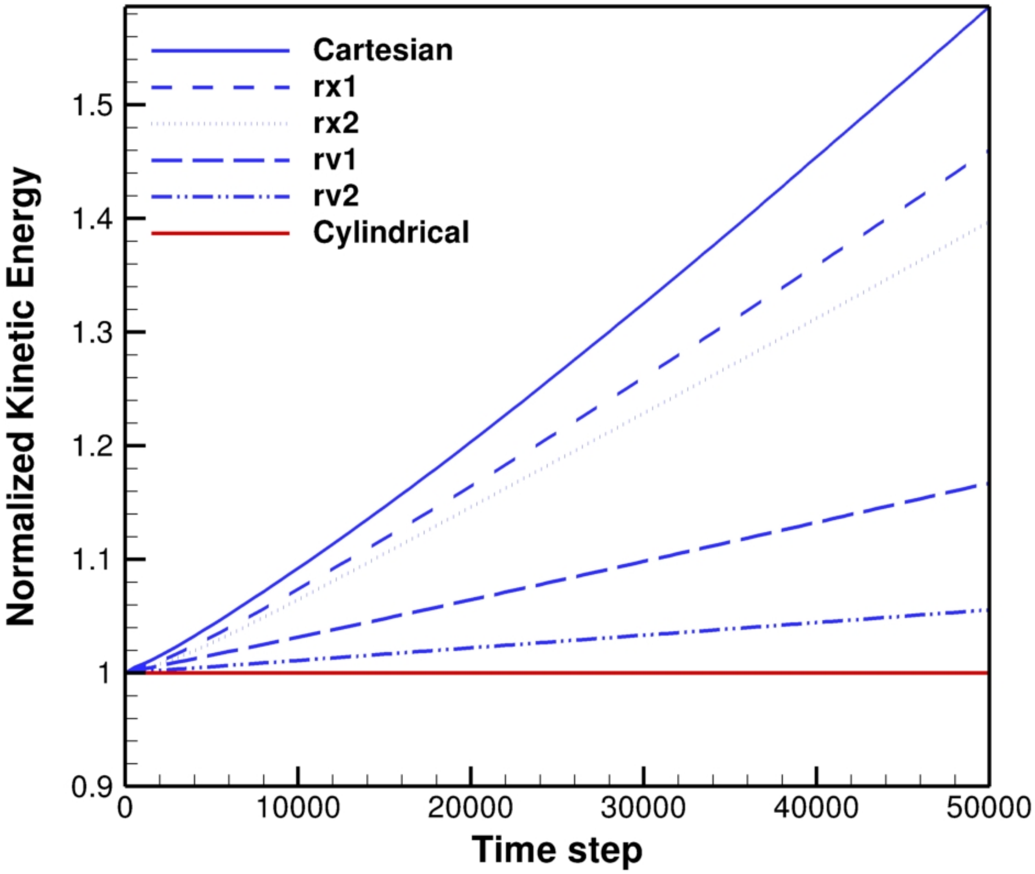

Figure 2.5: Comparing the energy conservation property of the Cartesian and cylindrical 2D-axisymmetric schemes. The cylindrical scheme preserves the system energy to machine precision while the Cartesian scheme converges towards this exact conservation with refinement of the grid.

rises from 300 K to 900 K by the end of the simulation. This clearly demonstrates the effect of numerical error when the coordinate transform forces are present. However, Figure 2.5 demonstrates that the level of conservation of energy improves with grid refinement; this is an important verification of the scheme. The cylindrical scheme, on the other hand, exactly (to machine precision) preserves the system energy over the course of the simulation such that the gas temperature is identical at the beginning and end of the simulation. This behavior clearly demonstrates the advantage of utilizing the cylindrical scheme for neutral gas flows where no outside forcing, such as the Lorentz force, is present.

2.3.3 Boundary Conditions

Careful application of boundary conditions (BCs) is important for an accurate solution, and a variety of boundary conditions are utilized in this thesis. These boundary conditions are used for both the hybrid- and fully-kinetic simulations conducted here. The DK scheme uses a ghost cell method to apply boundary conditions, where additional cells are simulated outside of the domain with values assigned according to the boundary condition desired. Two layers of ghost cells are applied at each boundary. There are five boundary conditions considered in this work: inflows, outflows, walls, periodic planes, and symmetry planes.

Physical Space: Inflows At inflow boundaries, a distribution function is set, based on information known *a priori*, relevant to the problem being considered. The inflowing distribution, f_{in}, is assumed to be in a state of thermal equilibrium, described by the Maxwell-Boltzmann distribution, with a known temperature and species mass. Both ghost cells are set to this distribution, $f_{g1,g2} = f_{in}$. The last term needed to fully describe the inflow is the number density, n. Two methods to supply this information have been implemented: i) scaling the distribution by a known number density n, or ii) supplying a volumetric flow rate, Q, and determining the number density from this quantity. More information on this second method will be detailed in Chapter III.

Physical Space: Outflows Outflow boundaries are defined by the information exiting the domain at the last cell, f_{out}. For a first-order accurate solution, assuming information exits the domain with positive velocity, a zeroth order extrapolation is used and the ghost cells are set equal to the information within the domain: $f(\mathrm{x},\mathrm{v})_{g1,g2} = f(\mathrm{x},\mathrm{v})_{out}$ for $\mathrm{v} > 0$. For second-order accuracy, a first-order extrapolation is necessary [130]. For information entering the domain, or ($v < 0$) in this example, an external pressure P_b may be assigned. Otherwise, a vacuum condition may be set by setting the ghost cells to zero: $f_{g1,g2}(\mathrm{x},\mathrm{v}) = 0$; as no background pressures are considered, this vacuum condition is used for all cases considered in this thesis:

$$\begin{cases} f_{g1}(\mathrm{x},\mathrm{v}) = f_{out}(\mathrm{x},\mathrm{v}) + \Delta x \frac{\partial f_{out}(\mathrm{x},\mathrm{v})}{\partial x} & \mathrm{v} > 0, \\ f_{g2}(\mathrm{x},\mathrm{v}) = f_{out}(\mathrm{x},\mathrm{v}) + 2\Delta x \frac{\partial f_{out}(\mathrm{x},\mathrm{v})}{\partial \mathrm{x}} & \mathrm{v} > 0, \\ f_{g1,g2}(\mathrm{x},\mathrm{v}) = 0 & \mathrm{v} < 0. \end{cases} \tag{2.24}$$

Physical Space: Walls When particles encounter a wall, they may either be perfectly (specularly) reflected, or strongly (diffusely) interact with the wall and be reflected according to a Maxwellian distribution with the temperature of the wall T_{wall}. Wall boundaries are therefore described by an accommodation coefficient, α_{acc}, which determines what fraction of particles are reflected specularly ($\alpha_{acc} = 0$) and what fraction diffusely ($\alpha_{acc} = 1$). In specular reflection, the information entering the domain from the boundary is set equal to the information exiting the domain. The information exiting the domain is set via zeroth order extrapolation. Assuming particles impinge on a wall boundary with positive velocity, $v > 0$, the ghost cells are set as:

$$f^{spec}_{g1,g2}(x,\mathrm{v}) = \begin{cases} f_{out}(\mathrm{x},\mathrm{v}) & \mathrm{v} > 0, \\ f_{out}(\mathrm{x},-\mathrm{v}) & \mathrm{v} < 0. \end{cases} \tag{2.25}$$

Therefore, all particles which impinge on the wall are effectively reflected.

In diffuse reflection, the information exiting the domain is set via zeroth order extrapolation. The information entering the domain is set to a half-Maxwellian distribution characterized by the wall temperature, T_{wall}. Again assuming particles impinge on a wall boundary with positive velocity:

$$f^{diff}_{g1,g2}(\mathrm{x},\mathrm{v}) = \begin{cases} f_{out}(\mathrm{x},\mathrm{v}) & \mathrm{v} > 0, \\ \prod_{n_d=1}^{N}\left(\frac{m}{2\pi k_b T_{wall}}\right)^{n_d/2} \exp\left(\frac{-mv^2_{n_d}}{2k_b T_{wall}}\right) & \mathrm{v} < 0. \end{cases} \tag{2.26}$$

The density of the incoming Maxwellian is set by equating fluxes in such a way that ensures mass conservation, $\Gamma_{in} = \Gamma_{out}$. [103] Finally, the boundary information is set according to: $f_{g1,g2} = (1 - \alpha_{accom}) f^{spec}_{g1,g2}(\mathrm{x},\mathrm{v}) + \alpha_{accom} f^{diff}_{g1,g2}(\mathrm{x},\mathrm{v})$, such that the accomodation coefficient α may be adjusted to allow any fraction of particles to be reflected specularly and diffusely.

Physical Space: Symmetry Planes The symmetry boundary is handled in the same way as the specular reflection boundary. Particles which impinge upon the boundary are reflected by assigning the incoming distribution to be equivalent to the outgoing one, while the outgoing distribution is set via zeroth order extrapolation. For particles impinging on a symmetry boundary with $v > 0$:

$$f^{symm}_{g1,g2}(\mathrm{x},\mathrm{v}) = \begin{cases} f_{out}(\mathrm{x},\mathrm{v}) & \mathrm{v} > 0, \\ f_{out}(\mathrm{x},-\mathrm{v}) & \mathrm{v} < 0. \end{cases} \tag{2.27}$$

Physical Space: Periodic Planes For periodic boundaries, the ghost cells are set to be equivalent to the cells adjacent to the boundary on the opposite side of the domain. For a domain with N_x cells:

$$f_{g1}^{peri}(x_{-1}, \mathrm{v}) = f_{out}(x_{N_x}, \mathrm{v}), \tag{2.28}$$

$$f_{g2}^{peri}(x_{-2}, \mathrm{v}) = f_{out}(x_{N_x - 1}, \mathrm{v}). \tag{2.29}$$

Velocity Space For all cases considered in this thesis, the velocity space boundaries are set to a Neumann condition with zero flux, e.g. $\frac{\partial f}{\partial v} = 0$. This assumption of zero flux is valid when the value of the VDF is negligible near the boundary, $f(\mathrm{v}) \approx 0$, which is accomplished by setting the velocity boundaries to be sufficiently large.

2.4 Maxwell's Equations

The fully-kinetic simulations of a plasma in this thesis require a self-consistent calculation of electromagnetic fields, where one must concurrently solve Maxwell's equation(s). In these studies, only electrostatic systems are considered, and therefore the magnetic field does not need to be calculated. Two options for calculating the electric field are possible: Poisson's equation and Ampere's equation.

2.4.1 Poisson's Equation

Poisson's equation is given by:

$$\nabla^2 \phi = -\frac{\rho}{\epsilon_0}, \tag{2.30}$$

where ϕ is the electrostatic potential and ρ is the charge density. In a plasma, the charge density is given by: $\rho = e(n_i - n_e)$, where n_i is the ion number density and n_e is the electron number density. Poisson's equation is purely elliptic and therefore requires a different class of solution method than those detailed for the DK solver. In these studies, the library PoisFFT is adopted, which makes use of Fast Fourier Transforms (FFTs) to solve this equation. [31] This library allows for a variety of boundary conditions, but in all cases considering Poisson's equation within this thesis, the boundary conditions are set to periodic.

2.4.2 Ampere's Equation

Another option for calculating the electric field is use of Ampere's equation: [93]

$$\frac{\partial E}{\partial t} = -\mu_0 c^2 (J_{int} + J_{ext}), \tag{2.31}$$

where J_{int} is the internal current density given by:

$$J_{int} = \sum_i q_i \int_{-\infty}^{\infty} v f(\mathrm{x}, \mathrm{v}) d\mathrm{v}, \tag{2.32}$$

where q_i is the unit charge of species i. In practice, however, the current density of the DK solver is actually given by the limited fluxes calculated by the likes of Equation 2.7. Therefore, the values of these numerical fluxes are used in place of the analytic fluxes calculated from Equation 2.32. When approaching electrostatic problems with Ampere's Law, a common assumption is that there exists some external current density, J_{ext}, such that the spatially-averaged electric field E_0 is constant in time: $\frac{\partial E_0}{\partial t} = 0$. [12] This means that J_{ext} always balances the spatially-averaged internal current, J_{int}. Solution of Ampere's equation has the advantage of requiring no spatial boundary conditions and may therefore be useful for open boundary simulations. However, while this method has been implemented in the code, it is not used for the studies detailed herein due to the possibility of temporal error to building up over the course of a simulation.

2.5 Collisions

In problems where collisions are important, the collision source term Q on the right side of the Boltzmann equation becomes non-zero. However, the full Boltzmann collision integral is very computationally costly and often unnecessary to solve exactly. Instead, different models are available, depending on the type of collision in question and the level of accuracy desired. In this thesis, two types of collision models are implemented in order to study collisional flows.

2.5.1 Ionization Collisions

In a plasma, ionization events are important in problems with sufficiently high neutral densities. The hollow cathode, for example, may have neutral densities of $\mathcal{O}(10^{19-22})$ m^{-3} near the cathode channel, and therefore it is expected that ionization events are frequent. [80] The model applied here is a rate coefficient model based on empirical data: [43]

$$Q_i = n_i n_n \zeta(\epsilon_e), \tag{2.33}$$

where n_n is the neutral density and the term $\zeta(\epsilon_e)$ is the rate coefficient which depends on the electron energy ϵ_e. This rate coefficient is given by: [103]

$$\zeta = \int_{\epsilon_0}^{\infty} \sqrt{\frac{2\epsilon_e}{m_e}} \sigma(\epsilon_e) f_e(\epsilon_e) d\epsilon_e, \tag{2.34}$$

where σ is the collision cross section, f_e is the electron energy distribution function, and ϵ_0 is the collision activation energy. Here, the electrons are assumed to be represented by a Maxwellian distribution, and so the rate coefficient may be represented only by the electron temperature: $\zeta(\epsilon_e) = \zeta(T_e)$. The collision cross sections used are given by Ref. [100]. Although doubly or triply charged ionization events are possible, in these studies only singly charged ions are considered. Self-consistent inclusion of multiply-charged ions is reserved for future work.

When ionization events occur, neutrals are subtracted from the system and ions are added to the system. However, in the 2D-AXI simulations, ions and neutrals are represented by different velocity space coordinate geometries (solving Eqs. 2.21 and 2.22, respectively). In order to properly execute ionization events, a mapping function is developed which ensures particle conservation. If the velocity coordinate in Cartesian space (for ions) is given by j_{ion}, the velocity coordinate in Cylindrical space (for neutrals) is given by j_{neut}. The mapping function then gives:

$$C_{map}(j_{neut}) = j_{ion}. \tag{2.35}$$

In order to calculate the number of neutrals lost, the normalized neutral distribution function, $\hat{f}_n$ is found by:

$$\hat{f}_n = f_n / n_n. \tag{2.36}$$

Then in a given time step Δt, neutrals are lost to ionization via the following:

$$f_n^{n+1}(j_{neut}) = f_n^n(j_{neut}) - \Delta t \zeta(T_e) \hat{f}_n(j_{neut}), \tag{2.37}$$

and ions are gained by ionization via:

$$f_i^{n+1}(C_{map}(j_{neut})) = f_i^n(C_{map}(j_{neut})) + \Delta t \frac{V_n}{V_i} \zeta(T_e) \hat{f}_n(j_{neut}), \tag{2.38}$$

where V_n and V_i are the velocity cell volumes for neutrals and ions, respectively.

2.5.2 BGK and ES-BGK Operators

In addition to ionization collisions, other collisions such as momentum-exchange collisions (MEX) are important in certain physical systems. For example, as mentioned in the last section, the hollow cathode channel has high neutral densities of $\mathcal{O}(10^{19-22})$ m^{-3}, where neutral-neutral (n-n) collisions are important and cannot be neglected. In order to model these collisions, the Bhatnagar-Gross-Crook (BGK) and ellipsoidal-statistical BGK (ES-BGK) collision operators are implemented. The

BGK model is given by the following:

$$Q_{MEX} = \frac{1}{\tau}(f_M(\mathrm{x}, \mathrm{v}) - f(\mathrm{x}, \mathrm{v})), \tag{2.39}$$

where τ is the relaxation time and f_M is the Maxwellian distribution function (Eq. 1.2) characterized by the local temperature and density.

The ES-BGK model is generally considered superior to the original BGK model as it is able to capture the correct Prandtl number, $Pr = \frac{2}{3}$, in the hydrodynamic limit. [64] The Prandtl number is a dimensionless quantity that is defined as the ratio between momentum diffusivity and thermal diffusivity. The ES-BGK model is given by the following:

$$Q_{MEX} = \frac{1}{\tau}(f_{eq}(\mathrm{x}, \mathrm{v}) - f(\mathrm{x}, \mathrm{v})), \tag{2.40}$$

where f_{eq} is an anisotropic Gaussian distribution characterized by the local temperature and number density:

$$f_{eq} = \frac{n}{\det(2\pi\mathcal{T})} \exp\left(-\frac{1}{2}(\mathrm{v} - \langle U \rangle)^T \mathcal{T}^{-1} (\mathrm{v} - \langle U \rangle) \right), \tag{2.41}$$

where R is the gas constant and $\mathcal{T} = \frac{1}{Pr} RTI + (1 - \frac{1}{Pr})\Theta$ is a linear combination of the stress tensor, Θ, and the Maxwellian isotropic stress tensor, I. [79] In the limit that $Q_{MEX} = 0$, the ES-BGK operator reduces to the BGK operator as $f_{eq} = f_M$.

The choice of how to define relaxation time, τ, depends on the collision process being modeled. In the case of neutral-neutral MEX collisions, the variable-hard-sphere (VHS) model is chosen. [4] From the VHS model, the relaxation time is:

$$\tau = \frac{T_{ref}^{\delta}}{\mu_{ref}} mnRT^{1-\delta}, \tag{2.42}$$

where T_{ref} is the reference temperature and δ is a constant related to the inverse-power law for inter-atomic potentials for the particular species in question. These values are assigned based on the species considered; considering xenon, for example, they are: $T_{ref} = 273K$, $\delta = 0.85$. Based on these values, the reference viscosity μ_{ref} is defined by:

$$\mu_{ref} = \frac{15\sqrt{2\pi m k_b T_{ref}}}{2(5-2\delta)(7-2\delta)\pi d_{ref}^2} \tag{2.43}$$

where d_{ref} is the reference diameter for xenon, taken to be $d_{ref} = 5.74\mathring{A}$. [10]

In order to avoid the strict CFL condition that would be imposed by the collision operator in dense regimes, e.g. where $\tau \lll 1$, an implicit-explicit (IMEX) method is applied. [98] In this method, the collision source term is computed implicitly, while the remaining flux terms are computed explicitly as previously detailed. To first-order, this method involves implicit calculation of an intermediate value of the VDF, $f^{(1)}$:

$$f^{(1)} = f^n + \frac{\Delta t}{\tau}(f_{eq} - f^{(1)}), \tag{2.44}$$

where the value at time $n+1$ is:

$$f^{(n+1)} = f^n + \frac{\Delta t}{\tau}(f_{eq} - f^{(1)}). \tag{2.45}$$

The IMEX approach is used in the problems within this thesis which make use of the BGK or ES-BGK operators to model collisions.

2.6 Verification Problems

It is of critical importance to provide verification of numerical methods in order to have confidence of future results. Verification is the process of comparing numerical results with an analytic solution or other, previously verified code results, to ensure that the code has been correctly implemented and is therefore solving the governing equations as intended.

2.6.1 Manufactured Solution for Poisson's Equation

In order to verify the PoisFFT solver in a standalone configuration, a 'toy' problem or manufactured solution is considered. Consider a 1D, periodic system where $\phi_{toy} = \sin(2x)$, such that the solution to Poisson's equation is then $\nabla^2\phi_{toy} = \frac{\partial^2\phi_{toy}}{\partial x^2} = -4\sin(2x)$. Solution of this equation by the PoisFFT library is expected to produce second-order accuracy, meaning the solution error, $\epsilon = \langle\phi - \phi_{toy}\rangle$ should decrease with number of grid points h following a power law with exponent -2. Indeed, in Figure 2.6 demonstrates that second-order accurate convergence is achieved by the solver by giving the equation of the line-fit to the data points (note that log in this case is the natural logarithm, such that $Y = e^{-2\log(x)} = x^{-2}$). With this result, there is confidence that the PoisFFT solver has been correctly implemented.

2.6.2 Sod Shock Tube

The ES-BGK model detailed in Section 2.5.2 is implemented in the DK solver; to verify the algorithm coupled with the solver, a classic problem in gas dynamics is considered: the Sod shock tube. [118] In this problem, gases with different properties are initialized on either side of a virtual diaphragm. At time $t = 0$, this diaphragm bursts (or is removed), allowing the gases to intermix. This problem is particularly well-suited to test that the collision algorithm is properly implemented and married to the DK solver, as an analytic solution exists and predicts that a shock, contact discontinuity, and rarefaction fan should be clearly observed.

The 1D problem is initialized as two Maxwellian gases, left (L) and right (R) of the diaphragm, with the following properties: $\rho_L = 5.25\rho_r$, $T_L = 6.75T_R$, where ρ represents the mass density of the gas. The numerical parameters of the test case are

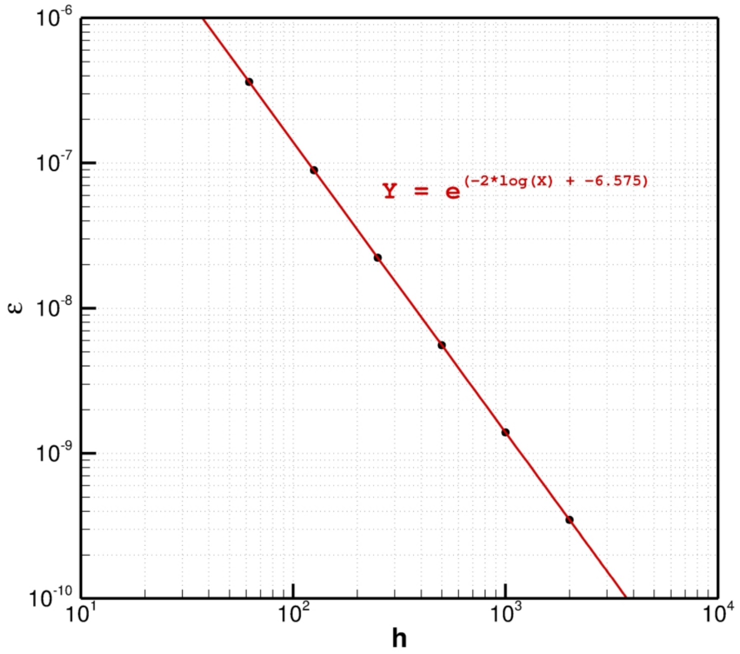

Figure 2.6: Grid convergence demonstrating second-order accuracy of the Poisson equation solver from PoisFFT. Numerical error, ϵ, decreases with an increasing number of grid points, h, to the second power.

detailed in Table 2.3. Solutions from the DK code are compared with exact solutions of the Riemann problem evaluated numerically (see Ref. [118] for details on these calculations) with Python.

Table 2.3: Numerical parameters of the Sod shock tube verification problem.

Physical Domain Size	L (cm)	2.0
Number of Physical Cells	N_x	2000
Velocity Bounds	V_x (m/s)	$[-1500, 1500]$
Number of Velocity Cells	N_v	120
Total Time	T (μs)	10
Number of Time Steps	N_t	$10,000$

Figures 2.7, 2.8, and 2.9 give the normalized density, velocity, and pressure compared with the Riemann solver solution. All results demonstrate excellent qualitative agreement with the analytic solution. Numerical diffusion is clearly visible, causing the DK solution to ‘smooth out’ near the regions of sharp gradients. This is due

to the flux-limiting scheme tending towards first-order accuracy to avoid numerical oscillation. [122] Nonetheless, even with this limiter in place, some amount of numerical oscillation is observed in the velocity solution in Figure 2.8. As this oscillation remains small and localized to the region of discontinuities in the flow, these results provide confidence that the collision algorithm is properly implemented and coupled to the DK code.

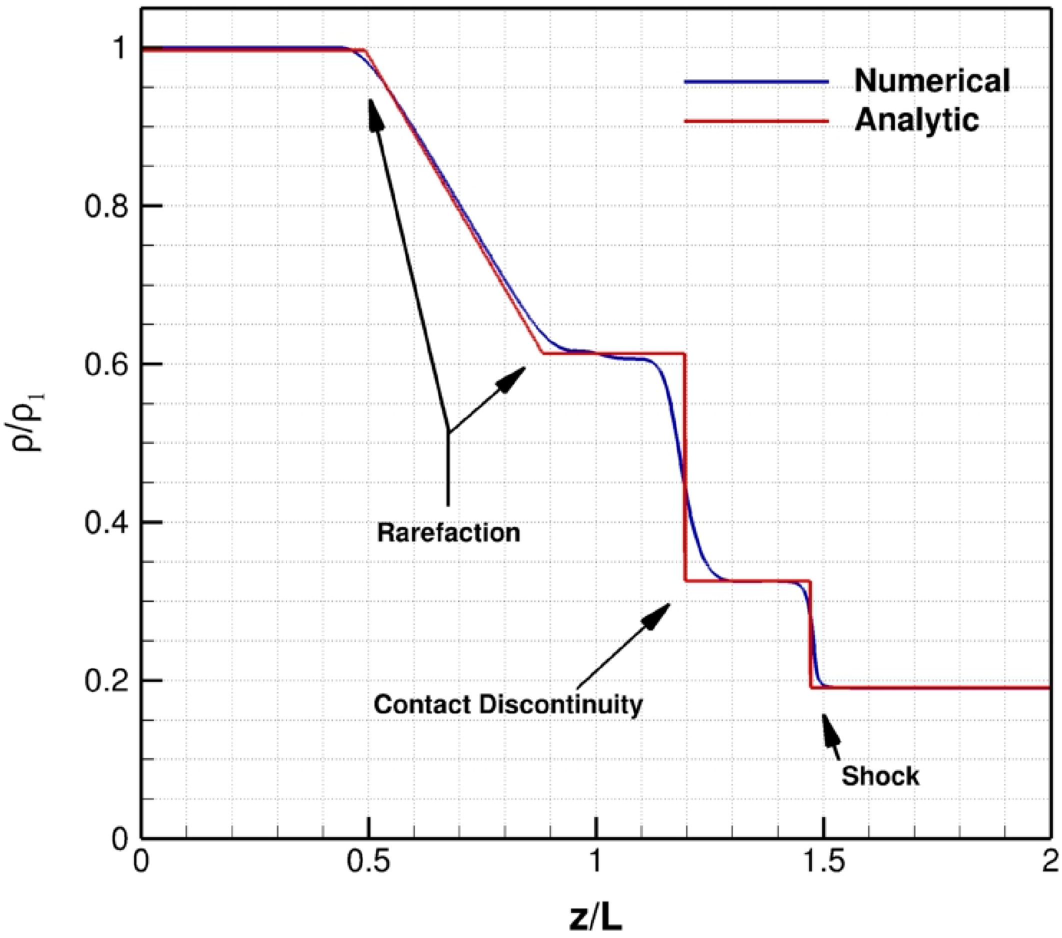

Figure 2.7: Normalized density from DK compared with the analytic (Riemann problem) solution for the Sod shock tube problem. The rarefaction, contact discontinuity, and shock are all labeled.

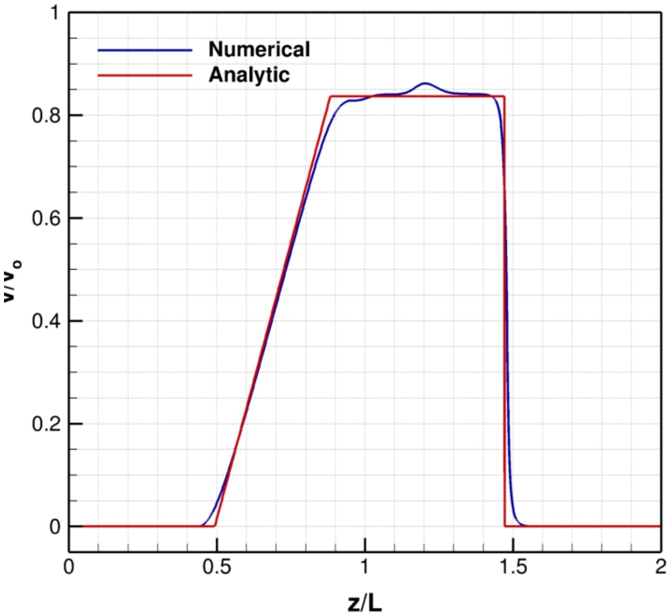

Figure 2.8: Normalized velocity from DK compared with the analytic (Riemann problem) solution for the Sod shock tube problem. A small numerical oscillation occurs near the contact discontinuity which is a likely result of the flux limiting scheme not providing sufficient diffusion in this region.

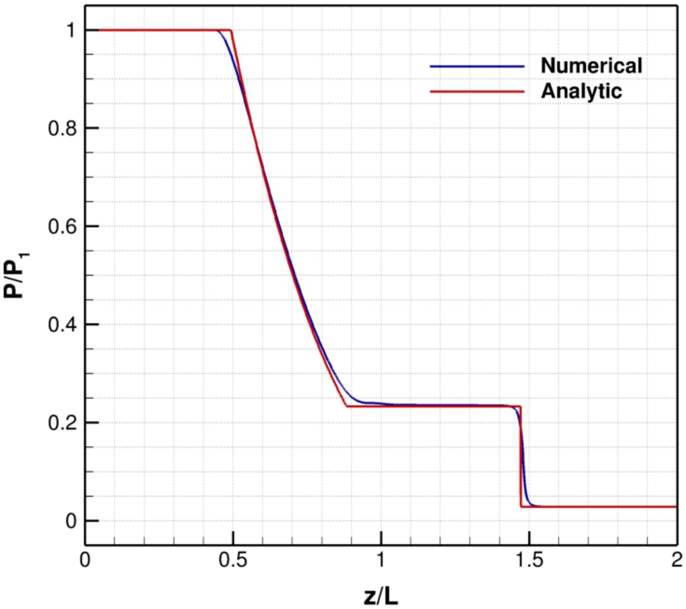

Figure 2.9: Normalized pressure from DK compared with the analytic (Riemann problem) solution for the Sod shock tube problem.

2.6.3 1D1V Landau Damping

The coupling of the Poisson's equation solver into the DK code is important to verify, as this solver has not been used in conjunction with the code previously. In order to accomplish this, the problem of Landau damping in a plasma is particularly useful. Landau damping is the collisionless damping of plasma waves whereby energy is transferred to the plasma particles at the expense of the wave energy. [69] This problem is particularly useful as a verification for plasma solvers as there exists an analytic solution for the linear damping rate γ for a particular wavenumber k_o and frequency ω_r:

$$\gamma = \omega_{p,e}\sqrt{\frac{\pi}{8}}\frac{1}{(k_o\lambda_D)^3}\exp\left(-\frac{1}{2}(k_o\lambda_D)^2\right), \tag{2.46}$$

where λ_D is the electron Debye length and $\omega_{p,e}$ is the electron plasma frequency. In practice, to launch a wave in the plasma simulation, a density perturbation is applied to the initial electron distribution f_{init} of the form:

$$f_{init}(x) = f_M(1 + \alpha\sin(k_o x)), \tag{2.47}$$

where α is the perturbation magnitude. The numerical setup of this problem is given in Table 2.4, where the problem dimension is 1D1V and the boundary conditions are periodic for both the DK and the Poisson solver. The problem setup is equivalent to that of Refs. [75, 110], where $k_o\lambda_D = 0.4$ and $\alpha = 0.05$. Ions are assumed to provide a stationary background. With no collisions, the solver is solving the Vlasov-Poisson system of equations.

From the density perturbation applied, Landau theory predicts an electron plasma wave to be launched with phase velocity $v_\phi = 3.21$. Figure 2.10 gives the logarithm

Table 2.4: Numerical parameters of the 1D1V Landau damping verification problem.

Total Time	T (ω_{pe})	60
Number of Time Steps	N_t	$25,000$
Domain Length	L (λ_D)	15.7
Number of Physical Cells	N_x	512
Electron Velocity Bounds	V_e ($v_{th,e}$)	[-6,6]
Electron Velocity Cell Count	N_{V_e}	1600

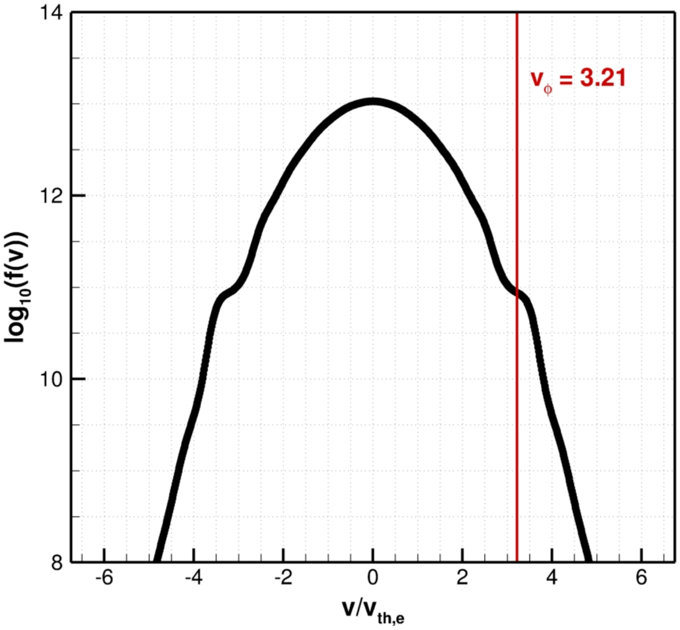

Figure 2.10: Trapping signature in the electron VDF associated with the density perturbation of electrons from Eq. 2.47. The theoretical prediction of phase velocity v_ϕ from Landau's theory is given as a red line.

of the spatially-averaged electron VDF, $\langle f \rangle$, from the simulation during the linear damping phase, with the expected phase velocity of the wave given as the red line. The electrons are trapped by the plasma potential oscillations caused by the wave, causing a plateau in the VDF centered around the wave phase velocity. Figure 2.10 provides confirmation that the wave launched in the plasma is traveling at the expected phase velocity. After the linear phase, Landau damping becomes inherently non-linear after the bounce time $\tau_b = \alpha^{-1/2}$. Figure 2.11 gives the variation of the average electric field with time during the course of the simulation, compared with the expected linear Landau damping rate of $\gamma = -0.0661$. The decay of the electric

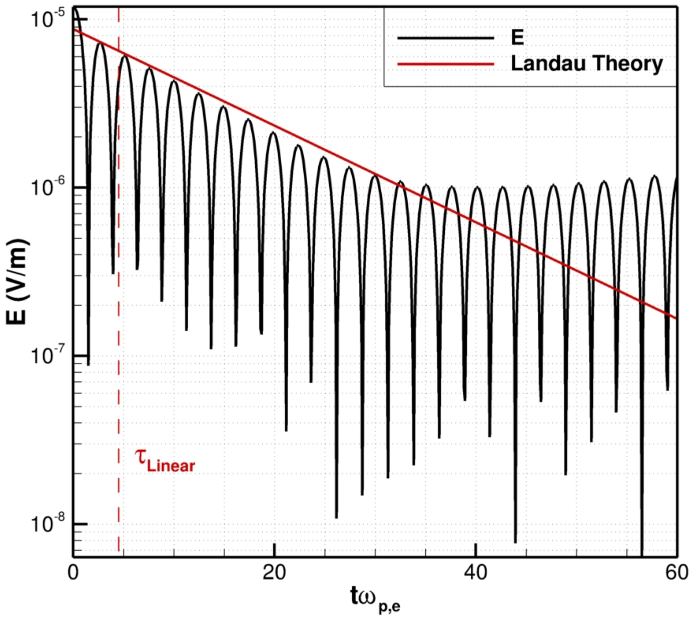

Figure 2.11: Damping rate of the electric field associated with the plasma wave (black) compared with the analytic theory of Landau damping (red) for 1D1V. The cutoff time of linear damping is marked by the dashed red line marked τ_{linear}, after which time non-linear effects become important.

field agrees well with the expected value. After time τ_b, the problem becomes non-linear; while agreement with the linear rate worsens after this time, it is observed that reasonable agreement with this damping rate is found until $t\omega_{p,e} \approx 25$, in agreement with Ref. [75]. These agreements with analytic predictions provide confidence that the 1D1V Vlasov-Poisson system is properly implemented.

2.6.4 2D2V Landau Damping

While the DK code has been previously verified for 1D1V problems, it has not been verified for 2D2V problems. A straightforward extension of the 1D1V Landau damping problem, verified in Section 2.6.3, is the 2D2V Landau damping problem. The problem in this case is similar to that in 1D1V: a density perturbation is applied to plasma electrons in order to launch a wave in the plasma, which is subsequently damped, collisionlessly, by Landau damping. For this case we use the parameters given in Table 2.5. The perturbation applied to the electrons takes the form:

$$f_{init}(x, y) = f_M(1 + \alpha \sin(k_o x) \sin(k_o y)), \tag{2.48}$$

where $\alpha = 0.05$ and $k_o = 0.5$.

Table 2.5: Numerical parameters of the 2D2V Landau damping verification problem.

Total Time	T (ω_{pe})	48
Number of Time Steps	N_t	$10,000$
Domain Length	L_x (λ_D)	12.6
Domain Length	L_y (λ_D)	12.6
Number of Physical Cells	N_x	64
Number of Physical Cells	N_y	64
Electron Velocity Bounds	$V_{e,x}$ ($v_{th,e}$)	[-6,6]
Electron Velocity Bounds	$V_{e,y}$ ($v_{th,e}$)	[-6,6]
Electron Velocity Cell Count	$N_{V_{e,x}}$	300
Electron Velocity Cell Count	$N_{V_{e,y}}$	300

For the input perturbation values, the expected damping rate is $\gamma = -0.394$. [91] Figure 2.12 compares the measured electric field amplitude, $E = \sqrt{E_x^2 + E_y^2}$, with this analytic prediction. The results indicate excellent agreement between the linear theory and the DK results until $t\omega_{p,e} \approx 25$, after which time non-linear effects dominate. This finding is the same as in the 1D1V case, which is to be expected as the density perturbation magnitude α is identical for both cases. With these results in hand, the 2D2V DK code, coupled with the Poisson solver, is verified.

2.7 Summary

In this chapter, an outline on numerical approaches to solving the Boltzmann equation (kinetic methods) was given. The deterministic-kinetic method, utilized in the remainder of the thesis, was described and the techniques used to solve the Boltzmann equation were detailed. A particular focus was the implementation of the 2D-AXI functionality in the code, while boundary conditions for the solver were also

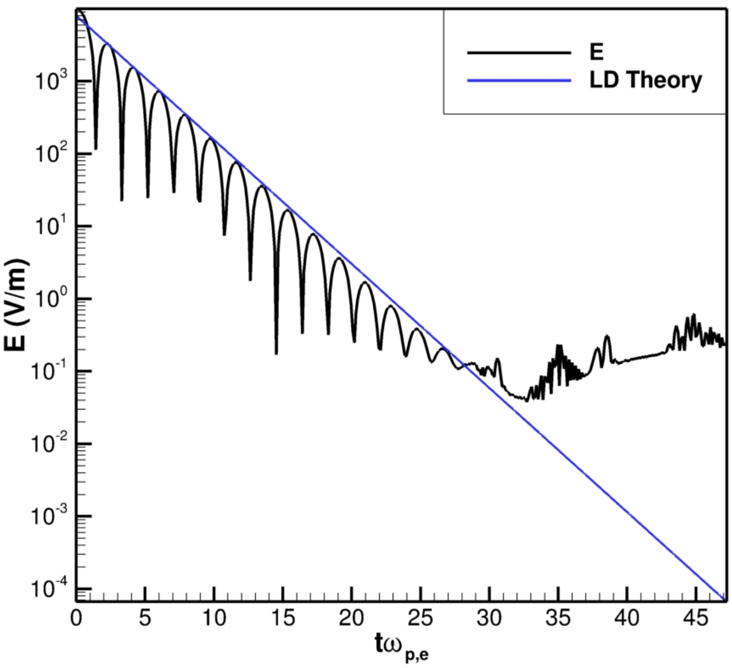

Figure 2.12: Damping rate of the electric field magnitude associated with the plasma wave (black) compared with the analytic theory of Landau damping (blue) for 2D2V. As in 1D, agreement with the linear theory is found until $t\omega_{p,e} \approx 25$. This is expected as the perturbation strength α is identical in both cases.

laid out. The implementation of supplemental modules, such as for Poisson's equation and for collisions, was explained. Finally, a variety of verification problems were analyzed: the 1D1V Sod shock tube for neutrals, 1D1V & 2D2V Landau damping for plasmas. Numerical solutions found good agreement with theory, providing confidence that the DK solver and new functionalities have been correctly implemented and coupled.

CHAPTER III

Neutral Gas and Plasma Expansion Flows

The existence of various methods to approach kinetic simulation of gas and plasma flows requires that one carefully considers which method is most appropriate for the problem at hand. While deterministic methods, such as the one developed in this thesis, are attractive for their noise-free nature, they are also generally known to require more computational resources to apply. It is therefore important to compare the deterministic method with another method, the stochastic particle method DSMC, to weigh the costs and benefits associated with each. Critical to such a comparison is the existence of analytic solutions for verification. The rarefied jet presents a useful tool for such a comparison, as analytic solutions exist in both one and multiple dimensions. In addition, the 2D-axisymmetric rarefied jet serves as a simplified hollow cathode problem, and thus provides a meaningful step towards a hollow cathode simulation tool.

In this chapter, Sections 3.1 and 3.2 consider neutral flow in both an unsteady, one-dimensional rarefied jet and a steady, two-dimensional-axisymmetric rarefied jet problem. For both problems, grid convergence is tested by refining the *discretization* variables associated with each numerical scheme. For DK, these variables are the spatial grid spacing Δx, velocity grid spacing Δv, and temporal grid spacing Δt, while for DSMC they are Δx, Δt, and the number of particles per cell, N_p. The distinction of N_p as a discretization variable is chosen so as to provide an analog to the Δv of DK; however, this quantity is also tied to the *statistical* error of particle methods. Statistical error is known to be related to the number of samples $N_s = N_p * k$, where k is the number of sampling steps or number of ensemble averages taken. These sections carefully consider statistical error in addition to discretization error when analyzing results.

After careful consideration of the rarefied neutral jet problems, Section 3.3 turns to simulation of a hollow cathode system, which involves concurrent simulation of both neutral and charged particles. For this purpose, the NSTAR discharge hollow cathode is chosen for comparison, as there exists a wealth of numerical and experimental data on this device. By comparing with experimental data, these results provide a level of validation for the newly developed cathode simulation platform, while also addressing the current shortcomings of the solver.

3.1 The Unsteady, One-Dimensional Rarefied Jet

3.1.1 Problem Setup

The problem of the unsteady, 1D rarefied jet has a solution detailed in Ref. 10. This problem is characterized by an equilibrium gas, described by temperature T_o and density n_o, initially held at rest within a reservoir. At time $t = 0$, a wall holding the gas is removed from one side, allowing the gas to escape. Solutions for both the density and velocity of the gas, in space and time, exist:

$$\frac{n(z,t)}{n_o} = \frac{1}{2}\,\mathrm{erfc}\left(\frac{\beta z}{t}\right), \tag{3.1}$$

and

$$U(z,t) = \frac{1}{\sqrt{\pi}\beta} \frac{\exp\left[-\left(\frac{\beta z}{t}\right)^2\right]}{\operatorname{erfc}\left(\frac{\beta z}{t}\right)}, \tag{3.2}$$

where erfc() is the complementary error function. For clarity of comparison, nondimensional variables are introduced in this solution. The spatial normalization factor is the hard sphere mean free path λ_o, which is defined as $\lambda_o = \frac{1}{\sqrt{2}n_o\sigma}$, where n_o is the number density of the gas and σ is the collision cross section of the molecule considered. The velocity normalization factor β, the inverse thermal velocity ${v_{th}}^{-1}$, is defined as $\beta = \sqrt{\frac{m}{2k_bT_o}}$. The temporal normalization factor τ is then defined as $\tau = \frac{\lambda_o}{\langle C \rangle}$, where $\langle C \rangle = \sqrt{\frac{8k_bT_o}{\pi m}}$ is the mean speed of the gas.

The domain extents and initial conditions for the problem are given in Table 3.1. A sweep of cases are run, uniformly refining the number of cells used for each discretization parameter in both numerical schemes. The number of cells or particles for each case are given in Table 3.2. Thus, in cases with an identically numbered subscript, the DK case (subscript D) and DSMC case (subscript S) have identical parameters, save for the difference between velocity cells and number of particles.

Dimensions	1D1V
Total Time, $\boldsymbol{T}$ (τ)	0.3
Channel Length, $\boldsymbol{L}$ (λ_o)	6
Velocity Boundaries, $\boldsymbol{V_z}$ (v_{th})	[-7,7]

Table 3.1: Numerical inputs for the 1D unsteady, rarefied jet cases run using DK and DSMC. The velocity boundaries are only relevant to the DK case.

Parameter	$\boldsymbol{C_{1D}}$	$\boldsymbol{C_{2D}}$	$\boldsymbol{C_{3D}}$	$\boldsymbol{C_{4D}}$	$\boldsymbol{C_{5D}}$	$\boldsymbol{C_{1S}}$	$\boldsymbol{C_{2S}}$	$\boldsymbol{C_{3S}}$	$\boldsymbol{C_{4S}}$	$\boldsymbol{C_{5S}}$
$\boldsymbol{N_t}$	150	300	600	1200	2400	150	300	600	1200	2400
$\boldsymbol{N_z}$	50	100	200	400	800	50	100	200	400	800
$\boldsymbol{N_{vz}}$	50	100	200	400	800	-	-	-	-	-
$\boldsymbol{N_p}$	-	-	-	-	-	50	100	200	400	800

Table 3.2: Grid parameters for the 1D rarefied jet cases. DK cases are denoted by subscript D while DSMC cases are denoted by subscript S.

3.1.2 Results: Comparing DK with DSMC

Figure 3.1a gives the densities and Figure 3.1b the velocities for a few cases of the 1D jet compared with the analytic solution at the early time of $t = 0.1\tau$. It becomes immediately clear that the DSMC solution does not exist in the far downstream region of the flow; this is due to the absence of any macroparticles in this region. At the same time, in the region where a solution does exist for DSMC, there are apparent fluctuations in the solution. Both of these problems may be traced back to an insufficient sample size, N_s. In the upstream region of the flow (behind the location of the removed wall), the DSMC solution is subject to fluctuations which diminish when the quantity N_p increases (see Figure 3.2), indicating the fluctuations are due to statistical error. Downstream of the removed wall, in this relatively early time of the flow, only fast particles or 'tails' of the distribution are able to reach locations far from the initial wall boundary. For DSMC, representing this sparse population of particles is difficult, as they represent only a small fraction of the VDF.

The problems of statistical error and insufficient particles to generate a solution may both be helped by increasing the quantity N_p, which would increase the sample size N_s in both the region upstream and downstream of the wall boundary. Ensemble-averaging of multiple runs would also serve to increase k and therefore N_s, yet this approach is not effective when there are insufficient macroparticles to generate a solution. It is important to note that, by choosing an early time in the simulation to make the comparison given here ($t = 0.1\tau$), the problem of resolving VDF tails in the downstream flow is exacerbated. As the solution progresses, the slow-moving particles reach the downstream section of the domain, making the difficulty of resolving the fast tails less pronounced and allowing a solution for the DSMC case.

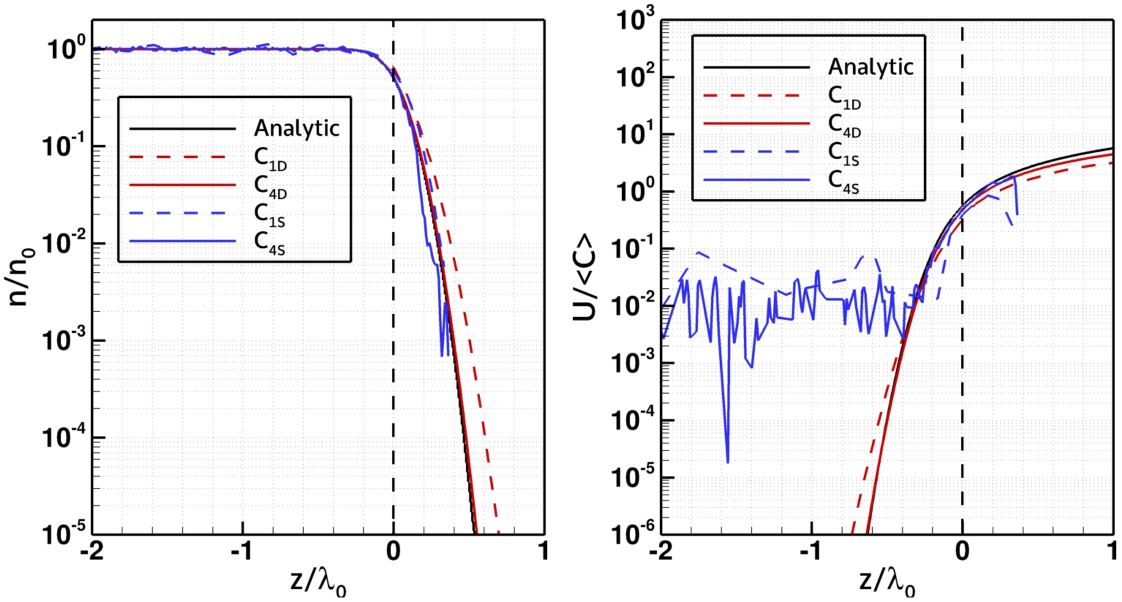

(a) Normalized densities.

(b) Normalized velocities.

Figure 3.1: 1D rarefied jet flow properties compared with the analytic solution in the domain at time $t = 0.1\tau$. The location of the removed wall is marked by the black dashed line.

There is another attribute of DSMC that is important to consider: since it is impossible to sample all possible velocity space, limits must be chosen for which particles will be introduced. In the case of MONACO, these limits are $\pm 3v_{th}$, which encompasses all but .002% of a non-drifting Maxwellian distribution. [4] The choice of velocity space limits for DSMC is important, as it determines how effective a certain number of particles can be at representing the VDF. In this case, extension of the velocity limits of DSMC would likely aid agreement in the downstream region, at the expense of requiring more macroparticles to represent the VDF. This is because larger velocity boundaries results in a greater velocity spread of macroparticles which represent the distribution; should N_p be kept constant, the resolution of the VDF becomes inherently coarser. In DK, the choice of where to cut off velocity space is also made; the advantage of DK is that the choice of an excessively large velocity domain does not risk under-representing the distribution while the cell size is kept constant, though it may result in undue computational expense. For this case, the DK velocity boundaries are $\pm 7v_{th}$, much larger than the effective boundaries set by DSMC. Aside from resolving tails of the VDF, the zero-gradient velocity boundary condition used in the DK method makes it important to ensure the distribution is essentially zero at the velocity boundaries, as this can otherwise lead to a buildup of information at the boundary and an unphysical solution.

The DK solution is able to capture the analytic solution more effectively than DSMC. There are no regions where the solution does not exist, nor are there fluctuations due to statistical error. Upstream of the wall, the DK solution is able to capture the very small bulk velocity, while downstream of the wall, DK well-captures the supersonic flow. The extent to which both methods capture the analytic solution is made more clear in Figure 3.2, which gives the relative error $\epsilon_r = (n_s - n_a)/n_a$, where n_s is the simulated value and n_a is the analytic value. The largest error in the DK solution is downstream of the wall, but decreases rapidly with grid refinement. By comparison, the DSMC error is much higher than DK upstream of the wall and, similar to DK, begins to increase in the downstream region before the solution vanishes and no further error may be plotted.

The convergence behavior for each method is determined by comparing the level of error for each refinement of the grids. As all parameters are refined simultaneously, the rate of convergence is expected to be either a mix of the rates of all parameters considered, if the errors are of similar magnitude, or dominated by the largest source of error. There are expected levels of error associated with both numerical approaches used here. The error in the DK method is subject to the order of accuracy of the numerical scheme; the DK method uses the second-order accurate method detailed in Chapter II and thus the expected convergence of numerical error goes with $\epsilon \sim N^{-2}$.

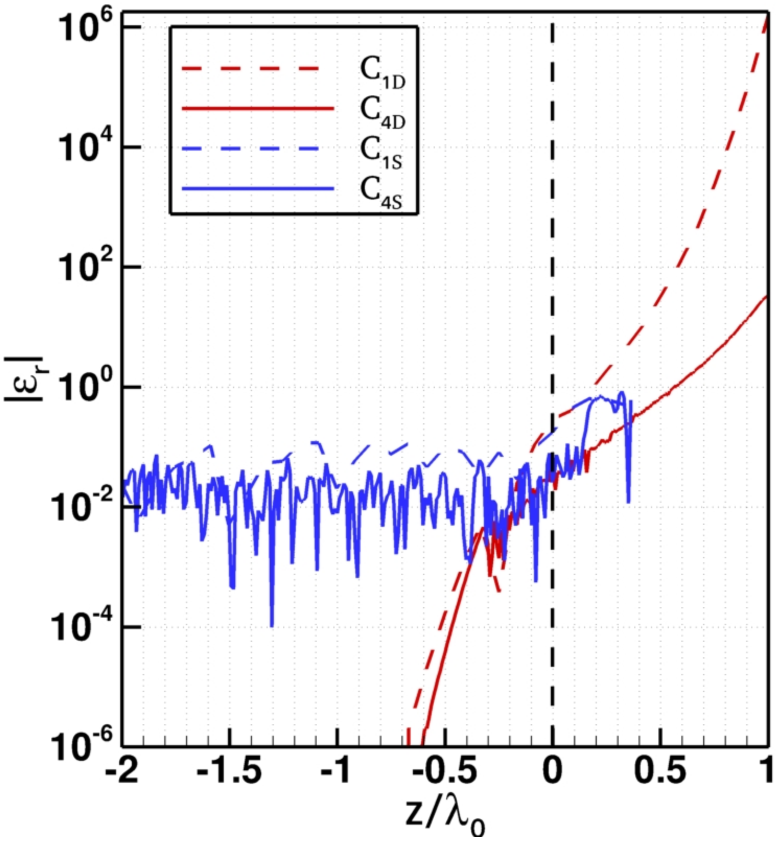

Figure 3.2: Relative density errors for DK and DSMC in the 1D rarefied jet.

For DSMC, the expected accuracy associated with the particle movement scheme is first-order, $\epsilon \sim N^{-1}$, while the order associated with the number of particles is also first-order. [20, 102] On the other hand, the statistical error of DSMC is known to converge with half-order, $\epsilon \sim N^{-0.5}$. [32] Therefore, only if the level of statistical error is driven below the level of discretization error will first-order accuracy be realized.

The chosen parameter in this comparison, seen in Figure 3.3, is the number of spatial cells N_x, though the rate would be identical for any chosen parameter as the refinement ratio is identical for all parameters, $r_p = 2$. The results from Figure 3.3 show that DSMC converges with the rate $1/\sqrt{N}$. This demonstrates that the DSMC results here are chiefly dictated by the statistical error, rather than any discretization error, in the range of parameters considered. On the other hand, DK converges with $1/N$, which is far below the expected second-order rate of convergence. The reason for this reduced convergence is due to the presence of a discontinuity in the problem considered here. In the presence of discontinuities, the flux limiter used drops to first-order accuracy in order to prevent numerical oscillation. [106] Therefore, the DK scheme is limited to first-order accuracy for this particular problem, which is important to consider when applying the DK method to further problems with discontinuous flow features.

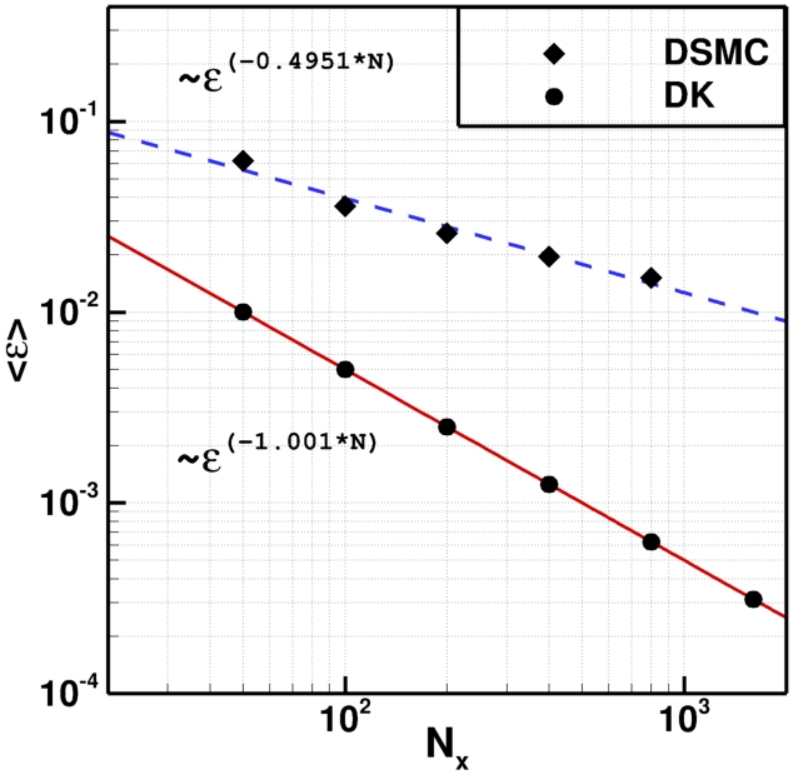

Figure 3.3: Grid convergence for DK and DSMC cases of a 1D rarefied jet. The DK solution converges with first order accuracy while the DSMC solution converges with one half order accuracy. The DSMC solution is not ensemble-averaged to demonstrate the effect of statistical error.

The amount of computational expense required to achieve a certain level of accuracy for both schemes is a useful metric when weighing which numerical approach to adopt. This comparison is subject to many factors, such as efficiency of each code structure. For example, the DK code is compiled with Intel compilers using the optimization flags `-O3` and `-ipo`. On the other hand, MONACO is compiled with GNU compilers using the optimization flag `-O3`. These compiler options may lend an advantage to the speed of the DK results. Nonetheless, despite these differences, comparing simulation wall times represents a useful benchmark to qualitatively understand the relative expense required to achieve a certain level of accuracy. In Figure 3.4, the computational wall time, WT, associated with each simulation is compared to the level of error. In the range of parameters considered, it is evident that DK achieves roughly an order of magnitude lower error than DSMC for similar wall times. Conversely, considering the wall time required to achieve the same level of error: DK is able to reach an error of order $\epsilon \sim 10^{-2}$ with a wall time that is approximately three orders of magnitude less than DSMC.

These results demonstrate the efficacy of DK for both an unsteady problem and a problem of low dimensionality (1D). However, it is important to recognize that ensemble averaging may enable DSMC to become more effective in this test case, by increasing the order of accuracy to $1/N$ in regions where there are sufficient particles to generate a solution. There are additional ways to improve the DSMC method; for example, Strang splitting has been demonstrated to enable second-order accuracy for spatio-temporal updates. [54] Further, running the simulation with significantly more particles is a viable method, given the computational ease of the 1D problem, in order to predict flow properties further downstream. However, this approach to unsteady problems would become far more computationally costly in higher dimensions, and a careful comparison of results for such a problem is necessary.

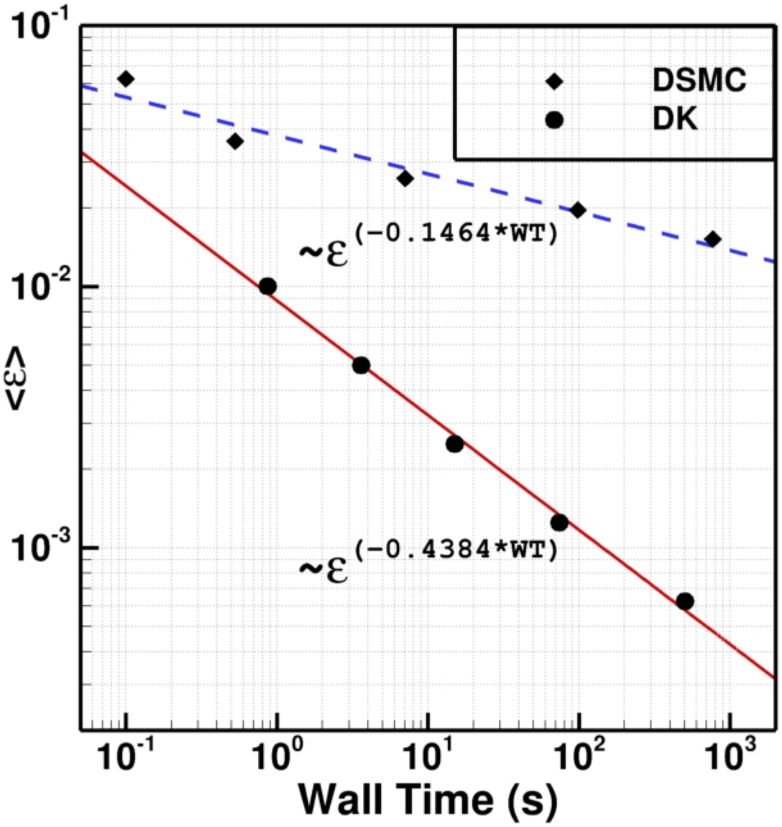

Figure 3.4: Computational effort to achieve a certain level of error for DK and DSMC cases of a 1D, unsteady rarefied jet. The DK results demonstrate better efficiency in achieving a lower level of error for a particular wall time. The DSMC solution is not ensemble-averaged to demonstrate the effect of statistical error.

3.2 The Steady, Two-Dimensional Axisymmetric Rarefied Jet

3.2.1 Problem Setup

Both steady and unsteady rarefied jet solutions have been derived in higher dimensions for a variety of inlet shapes. [14] The problem of interest in this study is that of rarefied gas effusion from a circular exit with zero bulk velocity ($U_o = 0$). The flow is assumed to be axisymmetric such that $\frac{\partial f}{\partial \theta} \approx 0$. This problem considers an exit with radius R, from which emanates an equilibrium gas with initial density n_o and temperature T_o. Here, the number density is used as the parameter for comparison;

the solution for the density in the flow field follows:

$$\frac{n(z,r)}{n_o} = \frac{1}{2} - \frac{z}{4\pi}\int_{-\pi}^{\pi}\left[\frac{z^2+r^2-rR\sin(\theta)}{(z^2+r^2\cos^2(\theta))\sqrt{z^2+r^2+R^2-2rR\sin(\theta)}}\right]d\theta, \tag{3.3}$$

where z is the axial position, r is the radial position, and θ is the angle between z and r as measured from the centerline. To emulate the physical problem, the left-side boundary is set to include an inflow condition up to $r = R$, and above this the ghost cells are set to vacuum. The centerline ($r = 0$) is set to a specular reflection condition, while the right-side ($z = L$) and upper-side ($r = H$) boundaries are set to outflow conditions.

Dimensions	2D3V
Total Time, $\boldsymbol{T_s}$ (τ)	150
Channel Length, $\boldsymbol{L}$ (λ)	.0258
Channel Height, $\boldsymbol{H}$ (λ)	.0258
Axial Velocity Boundaries, $\boldsymbol{V_z}$ (v_{th})	[0, 3.3]
Radial-Azimuthal Velocity Boundaries, $\boldsymbol{\xi}$ (v_{th})	[0, 3.3]
Angular Domain, $\boldsymbol{\omega}$ (degrees)	[0, 180]

Table 3.3: Numerical inputs for the steady, 2D-AXI jet case run using DK and DSMC. The velocity boundaries are only relevant to DK.

As for the 1D problem, multiple cases are run for each numerical method. Table 3.4 gives the details of the number of grid points used for each case. Since the problem of interest is steady, the number of time steps is chosen so the final result is found after the number of particles in the DSMC simulation and the total number density in the DK simulation have reached asymptotic limits. This steady-state time is chosen to be identical for both numerical schemes, $t = 150\tau$. However, for DSMC, time-averaging sampling steps must be taken after reaching steady-state in order to obtain a statistically meaningful solution; the number of sampling steps is increased by the same factor as all other parameters in these test cases. Both schemes utilize uniform, structured grids in physical and (for DK) velocity space.

In these cases, a few assumptions are employed to reduce the size of velocity

Parameter	C_{1D}	C_{2D}	C_{3D}	C_{1S}	C_{2S}	C_{3S}
$\boldsymbol{N_t}$	7500	15000	22500	7500	15000	22500
$\boldsymbol{N_z}$	20	40	60	20	40	60
$\boldsymbol{N_y}$	20	40	60	20	40	60
$\boldsymbol{N_{vz}}$	6	13	19	-	-	-
$\boldsymbol{N_\xi}$	32	65	98	-	-	-
$\boldsymbol{N_\omega}$	9	18	27	-	-	-
$\boldsymbol{N_p}$	-	-	-	50	100	200
$\boldsymbol{k}$	-	-	-	17500	35000	52500

Table 3.4: Grid parameters for all axisymmetric cases. DK cases are denoted by subscript D while DSMC cases are denoted by subscript S.

space: the flow is assumed to be irrotational, so the DK velocity grid in ω only includes angles 0° to 180°. In addition, since only particles with a positive axial velocity are present in the solution, the lower axial velocity bound is chosen to be $V_z = 0$. In contrast to the cases in Section 3.1, the number of particles per cell in DSMC is much lower than the total number of velocity cells in DK. In case C_{1D}, for example, the number of velocity cells per physical cell is $N_v = N_{vz} \times N_\xi \times N_\omega = 1,728$ cells; compared with the number of particles per cell in case C_{1S}, $N_p = 50$, this is a significant difference. However as will be demonstrated in Subsection 3.2.2, even with this relatively small number of particles, DSMC is able to achieve a level of error similar to that of DK.

For this problem, all cases are run in parallel on a Linux computing cluster; the number of cores is identical for each refinement: 10, 20 and 40 cores for subcases 1, 2, and 3 respectively. The DK scheme is parallelized by assigning processors purely based on axial position, z. The DSMC scheme, on the other hand, uses METIS to partition the grid based on balancing the number of particles across processors. [65] The parallel efficiencies of both codes are an important benchmark to consider; particularly, the weak parallel efficiency is important here as the problem size increases with each grid refinement. MONACO has been shown to maintain nearly 90% weak scaling efficiency for 50 processes, while, as seen in Figure 3.5, DK only demonstrates approximately 50% efficiency at this number of processes. Thus, there is a significant amount of computational overhead for DK for large problem sizes, which must be considered when interpreting wall times.

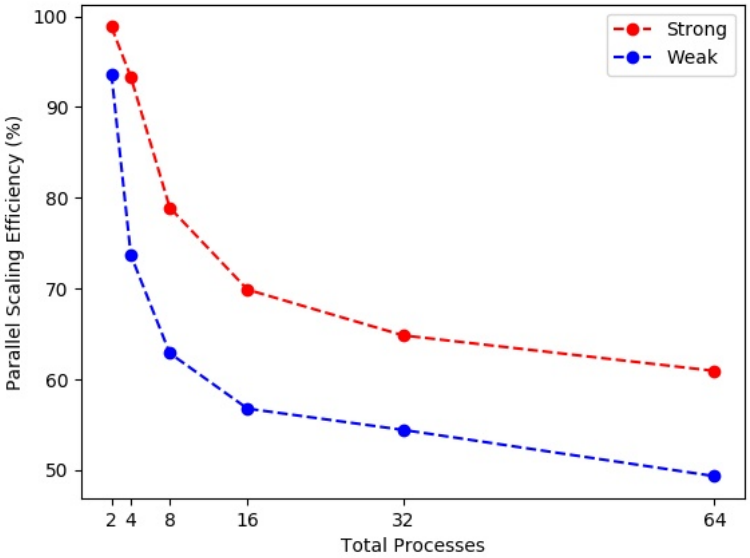

Figure 3.5: Parallel scaling efficiencies for the DK code.

3.2.2 Results: Comparing DK with DSMC

In Figure 3.6, the densities from solutions for four test cases detailed in Table 3.4 are given. An immediately noticeable feature lies near the centerline for the DK results, where for case C_{1D} there is a clear 'bump' in the density solution. This centerline behavior of DK simulations has been identified in previous studies, and is attributed to the difficulty in resolving the beam-like distribution near the centerline. [48,103] Due to the inability of the scheme to resolve this distribution, a buildup of particles near the centerline occurs. To remedy this problem, further refinement of the radial VDF is helpful; in case C_{3D} the centerline solution is much improved. Despite this difficulty with DK, good agreement with the analytic solution is otherwise found and improves with grid refinement. Another area where this improvement is notable lies in the large radial ($r = 0.6 - 1.0m$), but small axial ($z = 0.0 - 0.2m$) locations of the grid. Here, the density is over-estimated for case C_{1D}, but with refinement of the grid the error becomes nearly indiscernible.

For the DSMC solution, even the coarsest physical grid considered is able to resolve the solution to a surprising degree of accuracy when compared to the DK solution for an identical physical grid. The region with the most evident error is also along the centerline, where the solution contains fluctuations. Similar to the DK solution, this region is plagued by the difficulty in resolving the centerline beam distribution, which requires a sufficient number of particles emitted from the inflow to have zero or near zero radial velocity. Since there are relatively few particles with this property, this region is subject to greater error. Nonetheless, DSMC is able to capture the densities near the centerline with greater apparent accuracy than the DK method for the coarsest grid; for the finest grid, the difference between the two methods becomes much smaller.

In light of these results, it is important to recognize the particularly difficult nature of the present problem in resolving the centerline VDF for both schemes. Due to the absence of any collisions or any walls, there exist no particles which cross the centerline except for those which are emitted from the inlet. Thus, at ever larger axial positions, the only particles which exist near the centerline are those with very small radial speeds, which appear to be difficult for both schemes to resolve. In more realistic flows, e.g. those with collisions included, this difficulty would be less pronounced. Nevertheless, this difficulty is important to consider when approaching axisymmetric problems with both schemes.

Proving convergence of numerical error at the expected order-of-accuracy for the DK method is challenging due to the left-side boundary. The left-side boundary is a

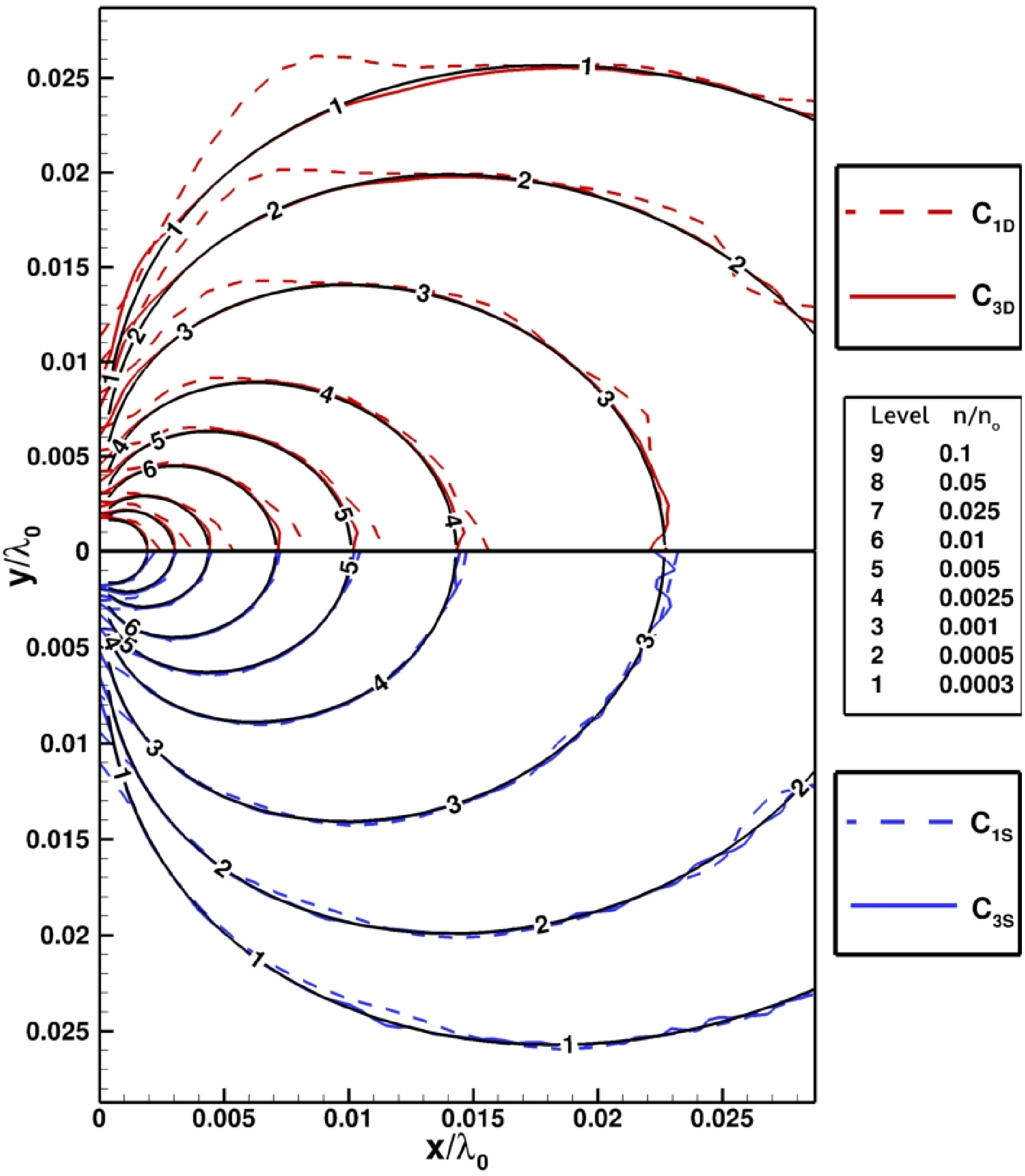

Figure 3.6: Densities of DK (red) and DSMC (blue) compared to the analytic solution (black) for the steady-state, axisymmetric rarefied jet.

vacuum condition where no particles should enter the domain; therefore, the ghost cell values here are set to zero. However, similar to the 1D problem, this amounts to a discontinuity which drives the flux-limiter function towards first-order accuracy. At the same time, for the analytic solution, values near this boundary are subject to integration error which may approach the level of the solution. [14] Therefore, for the purposes of evaluating the numerical convergence, cells near this boundary are neglected. It must be acknowledged that near-vacuum boundaries present a difficulty for retaining the desired order-of-accuracy in the DK method. However, in a more physically realistic system, e.g. one with collisions and wall boundaries, information could enter the domain from such a boundary (the ghost cells would not be set to zero, but rather a zero-flux or back-pressure condition), preventing the discontinuity and thus this difficulty. Indeed, outflow boundary conditions must be handled with care in order to preserve the desired order of accuracy. [130]

The level of spatially-averaged relative error, $\langle \epsilon_r \rangle = \langle (n_s - n_a)/n_a \rangle$, is given for all six cases in Figure 3.7. While the DK cases begin with larger error than DSMC, the error decreases with near the expected second-order accuracy, with a power fit parameter of `-1.78`. This result provides the first verification of the 2D-AXI functionality within the DK solver. Further, the DSMC solution error decreases with near the expected first-order accuracy, with a power fit of `-0.82`. Generally, in the axisymmetric case, both schemes have superior rates of convergence when compared to the 1D-unsteady case. For DK, this is due to the absence of a discontinuity in the bulk solution which caused the flux-limiting scheme to revert to 1st-order accuracy. For DSMC, this is due to the large number of sampling steps which are taken after the flow reaches steady-state, which drives down the statistical error. As the DSMC rate of convergence goes with $1/N$ rather than $1/\sqrt{N}$, in contrast to the 1D case, these results indicate the level of statistical error is less than that of the discretization error.

A final and important metric to consider is the wall time associated with each level of error attained; this data is plotted in Figure 3.8. These results demonstrate

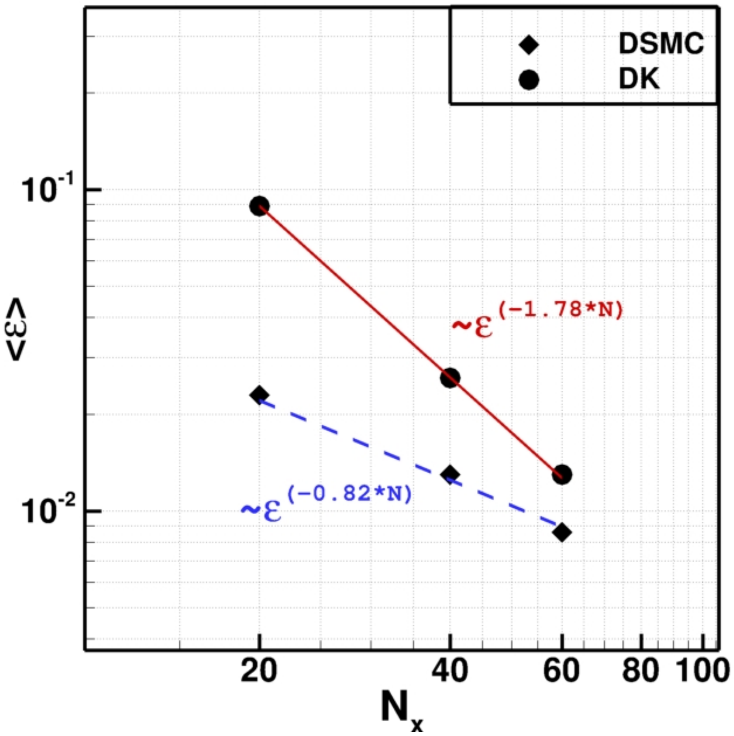

Figure 3.7: Grid convergence for DK and DSMC cases of a steady, axisymmetric rarefied jet when ignoring cells near the left-hand side vacuum boundary. The DK solver is able to converge with an order of accuracy one power greater than DSMC, but neither scheme achieves the expected order of accuracy.

the massive increase in computational expense associated with the DK method when considering this multi-dimensional problem. Although cases C_{2D} and C_{1S} achieve a similar level of error, the DK solution (using the same amount of computational resources) requires two orders of magnitude greater computational time. This computational burden is potentially restrictive and it is important to understand why there is a significant difference between the two methods. In axisymmetric coordinates, the DK method must resolve a 3D VDF for each physical cell; this means that the total grid size for, say, the C_{2D} simulation is: $N_{tot} = N_v * N_z * N_y = 24.3$M units. In contrast, the DSMC simulation carried out on the same physical grid has a total size (assuming particles to be a proxy for velocity cells) $N_{tot} = N_p * N_z * N_y = 0.16$M units. This amounts to a domain size difference of ~ 150x between the two schemes, and helps to explain the identically large increase in computational expense. These results also demonstrate that the massive increase in domain size for DK ($\sim$ 150x) has a greater impact on computational expense than the additional time steps required by DSMC ($\sim$ 3.3x) to sample the solution.

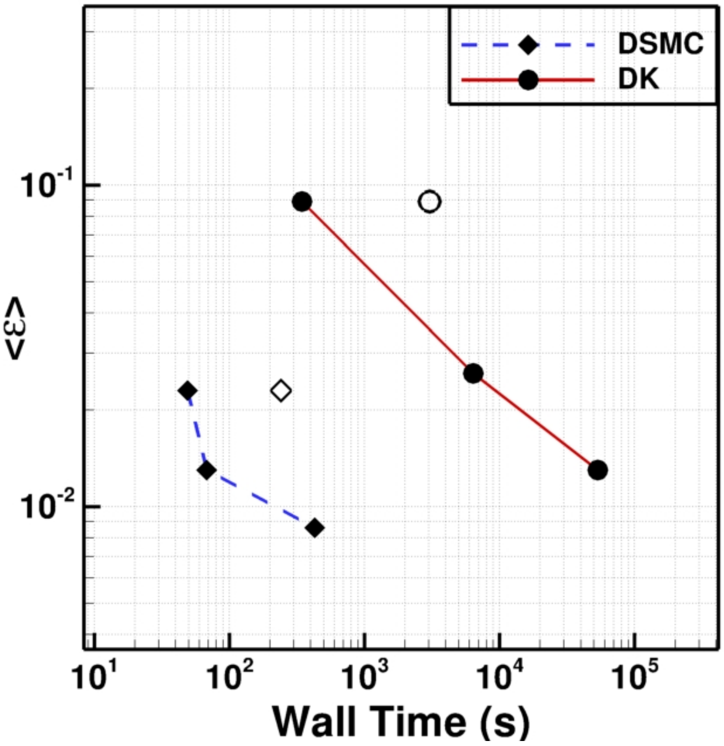

Figure 3.8: Computational effort to achieve a particular level of error for DK and DSMC cases of a steady, axisymmetric rarefied jet when ignoring the left-hand side vacuum boundary. A serial version is run for the coarsest grid and is plotted for both schemes as the unfilled symbol.

Ultimately, these results highlight the importance of exploring avenues to more efficiently utilize computational resources when applying the DK method to multi-dimensional problems. For example, the use of non-uniform meshes in velocity space or adaptive mesh refinement (AMR) would enable a more cost-effective approach. [66] AMR takes advantage of the fact that the VDF may often be described by a much smaller portion of velocity space than the entire domain, and refines the mesh only where it is useful. The method used in this study, however, requires that velocity space be uniformly represented, and therefore at any physical point there may be many velocity cells where the distribution f is very sparsely populated (and thus that are not contributing to the solution). Further, more efficient parallelization is important to drive down wall times; for example, it is possible to parallelize the algorithm in both spatial directions (axial and radial), which may provide computational cost savings for large number of spatial grid points. Finally, while the DK scheme utilized here is 2nd order accurate and makes use of uniform spatial and velocity grids, there are ways to improve the accuracy achieved for a similar computational expense. Higher order methods, such as fourth-order, have been implemented which would allow faster convergence. [128]

3.2.3 Considering Multi-Dimensional Transient Behavior

Section 3.1 demonstrated the efficacy of the DK method when considering an unsteady expansion into vacuum, particularly in its ability to provide good agreement with the analytic solution for distances far from the ‘inlet.’ By contrast, the DSMC method struggled to provide a solution in these regions due to a lack of particles. It is useful to briefly consider these effects for a multi-dimensional problem, such as considered in this section, as well. Figure 3.9 gives the density solution for both DK (C_{2D}) and DSMC (C_{2S}) at time $t = 10\tau$, overlaid on a contour which shows the number of particles per cell, N_p, from the DSMC solution. The DSMC solution has been re-run with an automatic weighting scheme to attempt reaching $N_p = 1,000$ particles per cell in order to provide better accuracy in regions advancing into vacuum, where fast VDF tails dominate the bulk properties.

While both solutions agree well near the inlet, this agreement becomes worse near the domain outflow boundaries. Indeed, the number of particles in DSMC rapidly

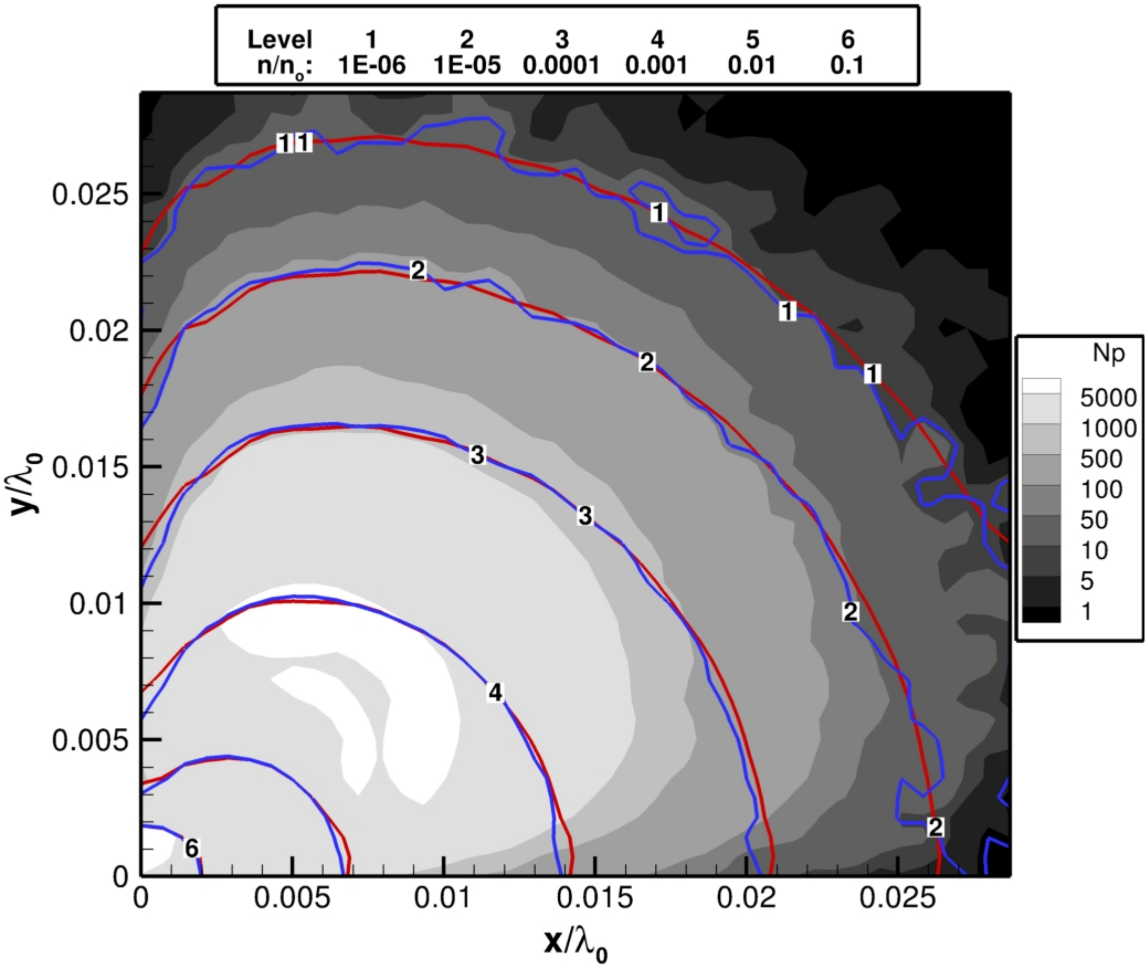

Figure 3.9: Transient density solution for the 2D-axisymmetric problem at $t = 10\tau$, with DK as the red lines and DSMC as the blue lines. The solutions are overlaid on a contour of the number of particles per cell (N_p) in the DSMC solution.

drops off near the boundaries, as the domain is initially set to a vacuum condition. Figure 3.10 demonstrates this more clearly, by sampling a line which cuts across the domain at a 45° angle. In this plot, the DSMC density drops rapidly near the domain edge, which corresponds to the region with no macroparticles. This behavior is similar to that observed in Section 3.1, and again demonstrates the difficulty for DSMC to capture a transient expansion into vacuum which requires resolving fast-moving tails of the VDF. Further increasing the number of particles may help to alleviate this problem, though as in 1D, the resolution of these tails of the VDF is more suited for the DK method as it is effectively guaranteed by simulating a sufficiently large velocity domain. Although the computational cost to achieve these solutions favors the use of DSMC, the advantage of DK in resolving VDF tails is an important consideration when weighing these numerical approaches.

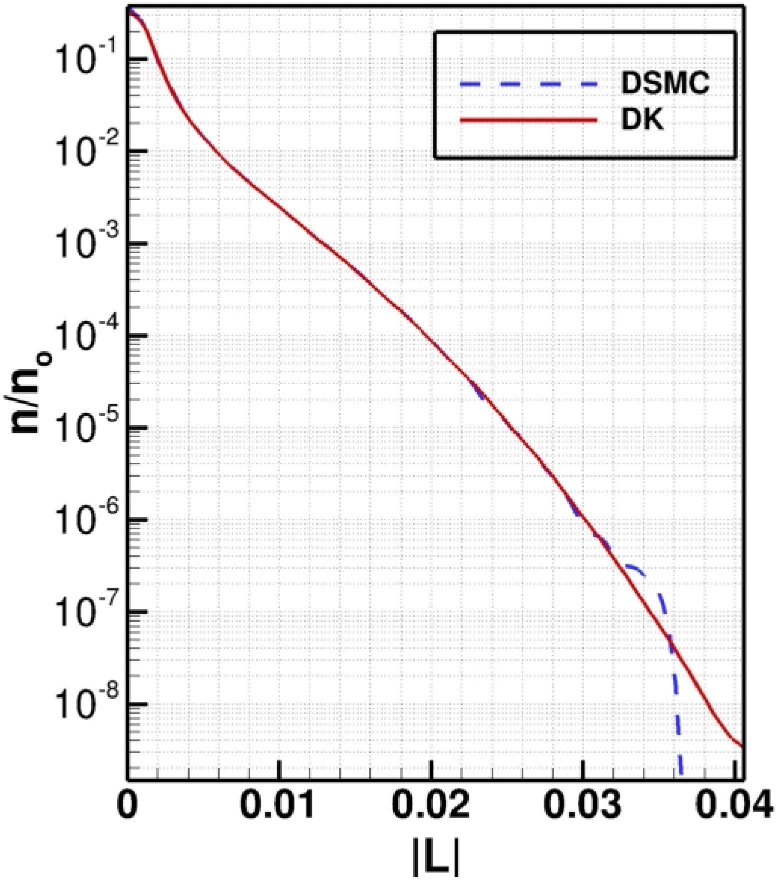

Figure 3.10: Transient density solution for the 2D-axisymmetric problem at $t = 10\tau$, taken as a 45° line across the simulation domain. $|L|$ is the position magnitude. The density solution for DSMC vanishes near the boundary, where the number of particles rapidly drops off.

3.3 The NSTAR Discharge Hollow Cathode

3.3.1 Problem Setup

Section 3.2 demonstrated the advantage of DSMC for steady problems in higher dimensions, while also serving to verify the 2D-axisymmetric DK solver with an analytic solution. With this verification of the 2D-axisymmetric DK solver, attention may now turn to simulation of a cathode geometry. Though hollow cathode operation is considered to be steady state, recent developments regarding the effect of instabilities highlight the possible importance of resolving fine-scale portions, and even transient behavior, of the VDF. Therefore, rather than particle methods, the DK method is applied to simulation of a hollow cathode geometry. The NASA Solar Electric Propulsion Technology Applications Readiness (NSTAR) project saw extensive development towards a gridded ion thruster which was eventually flown on NASA's Deep Space 1 mission. [11] The NSTAR discharge hollow cathode, which provides the ionization source to sustain the plasma discharge, has been the subject of experimental [26, 40] and numerical [84, 112] investigation partially due to high keeper erosion rates. Therefore, this cathode presents a useful testbed for the newly developed solver used in this thesis.

Similar to a hollow cathode experimental run, in these simulations the neutral gas (xenon) is allowed to flow before the plasma is lit. Therefore, in Stage I only neutral gas is simulated, while in Stage II both neutrals and charged species are simulated. The boundary conditions of the hollow cathode are given in Figure 3.11. An axis of symmetry condition is imposed at the centerline (given in blue), while the outflow conditions (given in green) are assumed to be vacuum. Since a self-consistent wall heating model is not applied in this study, the cathode wall boundary temperature, T_{wall}, is assumed to be at a steady-state operation temperature characteristic of the device. At the inflow, the neutral gas temperature, T_{in}, is assumed to be in equilibrium with the walls. The numerical properties of the spatial grid and the neutral gas are given by Table 3.5.

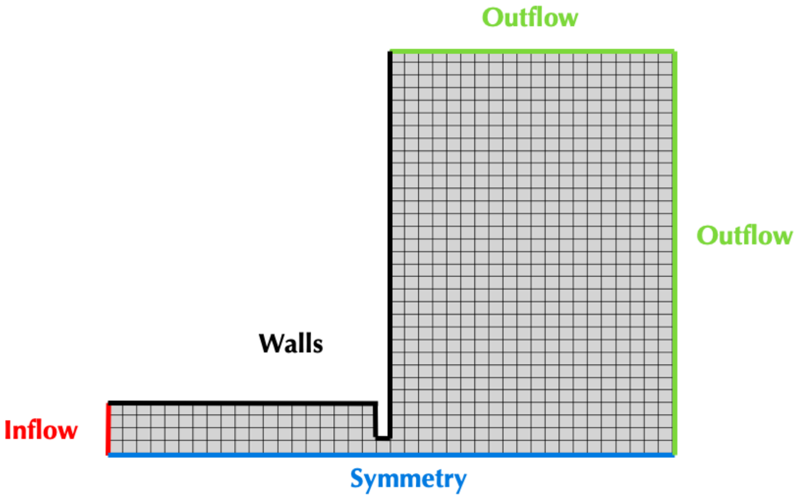

Figure 3.11: Boundary conditions for the NSTAR discharge hollow cathode geometry.

Special care has to be taken in order to obtain the proper neutral density at the inflow. Cathode operating conditions are given in terms of a volumetric flow rate, Q, in standard cubic centimeters per minute (SCCM). However, early simulation attempts demonstrated neutral densities that were below experimental values by order(s) of magnitude. This discrepancy is due to not properly accounting for backpressure within the cathode channel; a method to do so based on the cathode geometry is therefore adopted in order to remedy this: [43]

$$n_n = 9.65x10^{24} * \frac{P_n}{T_n}, \tag{3.4}$$

where T_n is the temperature of the gas and,

$$P_n = \sqrt{\frac{0.78Q\xi T_r l}{d^4}}, \tag{3.5}$$

Time Step, $\boldsymbol{\Delta t}$ (s)	5×10^{-8}
Channel Length, $\boldsymbol{L_c}$ (cm)	2.0
Channel Height, $\boldsymbol{H_c}$ (cm)	0.2
Plume Length, $\boldsymbol{L_p}$ (cm)	2.0
Plume Height, $\boldsymbol{H_p}$ (cm)	1.6
Orifice Length, $\boldsymbol{L_o}$ (cm)	1.0
Orifice Height, $\boldsymbol{H_o}$ (cm)	0.5
$\boldsymbol{V_Z}$ (v_{th})	[-4.5,4.5]
$\boldsymbol{\xi}$ (v_{th})	[0,4.5]
$\boldsymbol{\omega}$ (deg)	[0,180]
$\boldsymbol{N_t}$	25,000
$\boldsymbol{N_Z}$	40
$\boldsymbol{N_R}$	64
$\boldsymbol{N_{V_Z}}$	26
$\boldsymbol{N_\xi}$	260
$\boldsymbol{N_\omega}$	18

(a) Simulation domain conditions.

Accomodation Coefficient, $\boldsymbol{\alpha}$	1.0
VHS Power, $\boldsymbol{\delta}$	0.85
Volumetric Flow Rate, $\boldsymbol{Q}$ (SCCM)	3.6
Inlet Density, $\boldsymbol{n_{inlet}}$ (m^{-3})	2.20×10^{22}
Inlet Temperature, $\boldsymbol{T_{inlet}}$ (K)	1350
Wall Temperature, $\boldsymbol{T_{wall}}$ (K)	1350

(b) Neutral gas conditions.

Table 3.5: Numerical input conditions for the simulation domain and the neutral gas for the NSTAR discharge hollow cathode case run using DK. A DSMC case is run with identical conditions for verification of the newly implemented functionality in the DK solver.

where ξ is the viscosity of the gas, $T_r = T_{in}/289.7$, l is the length of the cathode channel, and d is the diameter of the cathode orifice. The viscosity of xenon is found from [43]:

$$\xi = 2.3 \times 10^{-4} T^{0.71+0.29/T_r}. \tag{3.6}$$

With this inlet boundary condition in place, neutral densities are found to match the experimental values to the correct order of magnitude.

In Stage II, when the plasma is 'turned on,' ions and electrons are accounted for via two methods. Singly charged ions (no multiply charged ions are considered) are simulated kinetically via the 2D-AXI DK solver. Due to the action of the Lorentz force on the ions, Equation 2.21 is solved for the ions while Equation 2.22 is solved for the neutrals. Electrons are modeled by assuming the plasma to be quasineutral ($n_e \approx n_i$), where they act as a massless fluid which exactly follows the ion motion. Neglecting resistive effects and assuming the plasma to be isothermal allows the plasma potential to be found via the Boltzmann relation:

$$\phi = \frac{k_b T_e}{e} \ln\left(\frac{n_i}{n_o}\right) + \phi_o, \tag{3.7}$$

where n_o and ϕ_o are a reference density and potential, respectively. These values are assigned such that the correct density-potential relation is found in the region of interest; they are given in Table 3.6. From the potential found from Equation 3.7, the electric field E is calculated from a second-order accurate central finite-difference stencil:

$$E = \frac{\phi_{i+1} - \phi_{i-1}}{2\Delta x}. \tag{3.8}$$

Given the use of the Boltzmann model rather than a kinetic description of electrons, this model is hybrid-kinetic. The properties of the DK ion mesh are given in Table 3.6. Two types of collisions are considered for the NSTAR simulation: neutral momentum exchange and, in Stage II only, ionization collisions. The algorithms used for both of these collisions are detailed in Section 2.5.

The assumption of quasineutrality is a good one for the cathode channel, [82] though this assumption breaks down in the cathode plume. Among other reasons, this is because a) electrons gain significant drift velocity due to acceleration by the applied voltage rise upon exiting the cathode orifice and b) classical collisions fall dramatically outside the orifice as the flow becomes rarefied. An extension of this model is important but beyond the scope of this thesis and is reserved for future work. Another shortcoming of using the Boltzmann relation for electrons is that is does not self-consistently calculate the electron temperature, T_e. Therefore, this value must be assigned in the simulation domain. In this study, the electron temperature is assumed to increase monotonically in the axial direction from 1 eV to 4 eV. This assumption

$\boldsymbol{V_Z}$ (v_{th})	[-13.5,20.5]
$\boldsymbol{V_R}$ (v_{th})	[-20.5,20.5]
$\boldsymbol{V_\theta}$ (v_{th})	[-6.8,6.8]
$\boldsymbol{N_{V_Z}}$	40
$\boldsymbol{N_{V_R}}$	48
$\boldsymbol{N_{V_\theta}}$	20
Loss Coefficient, $\boldsymbol{\beta}$	1.0
Reference Potential, $\boldsymbol{\phi_o}$ (V)	-20.0
Reference Density, $\boldsymbol{n_o}$ (m^{-3})	1×10^{16}

Table 3.6: Simulation conditions for the plasma in Stage II of the NSTAR cathode case for DK. The velocity boundaries given are for the kinetic ions, while the reference values are used for the Boltzmann relation.

is based on experimental measurements for various hollow cathode geometries which demonstrate electron heating as the plasma expands into the cathode plume (see, for example, Fig. 5 in [42]). This non-classical behavior is thought to be the result of the ion-acoustic instability, which will be discussed in detail in Chapter IV.

3.3.2 Results: Neutral Flow Verification with DSMC

As detailed in Section 3.3.1, Stage I is run with only neutral xenon flow until a steady-state is reached. A number of new additions to the solver have not yet been tested; first, the ES-BGK collision algorithm has not yet been tested when coupled with the 2D-AXI solver. In addition, the 2D-AXI solver has been modified to handle an orificed cathode geometry. Given these changes, it is important to verify the solver with DSMC once more. Thus, a 2D-AXI neutral flow simulation in MONACO is undertaken with identical boundary conditions, grid size and time step size; other important input parameters are $N_p = 100$ and $k = 350,000$. As in previous MONACO runs, the number of particles is automatically scaled to maintain N_p particles per cell.

Figure 3.12 gives the density contours for the DK and DSMC results, while Figure 3.13 gives the number density and flow velocities along the centerline of the domain. [123] The orifice exit, where the gas rapidly expands, is at location $L = 0.2$

cm. From Figure 3.12, it is clear that the two solutions agree well qualitatively. The largest apparent difference in the results is at the centerline, where the DK solution is not smooth. This behavior is similar to that noted in Section 3.2, again demonstrating the difficulty in resolving the centerline flow. Nonetheless, these results are encouraging and indicate that the DK solver is properly implemented and coupled to the collision algorithm.

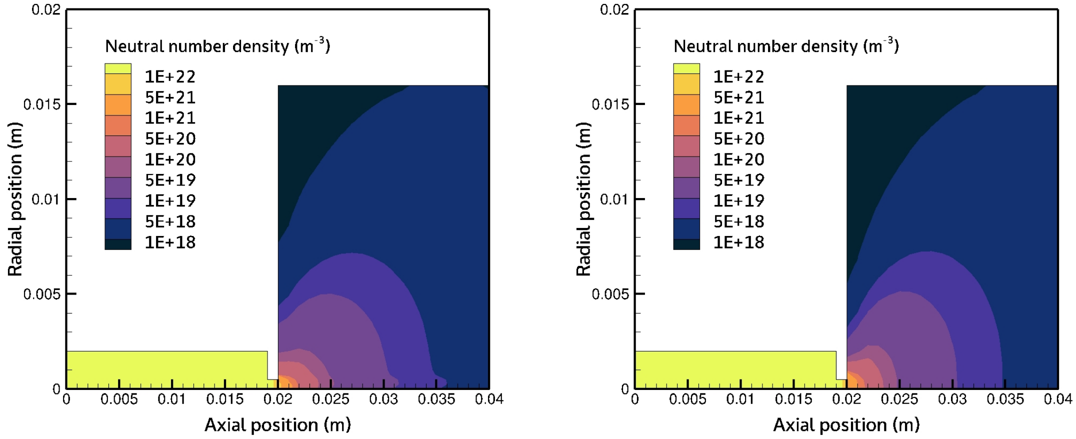

Figure 3.12: Density contours of the NSTAR neutral flow verification for the DK code (left) and DSMC (right), demonstrating the rapid expansion of the gas near the orifice. As noted in Section 3.2, the centerline of the DK results proves difficult to smoothly resolve, yet otherwise the solutions appear to be in qualitative agreement.

Along the centerline in Figure 3.13, the greatest apparent discrepancy between the DK and DSMC results is in the radial velocity just beyond the orifice exit. This region of the flow is transitional [121] and likely poses a challenge for the ES-BGK model used to simulate the collisions; similar levels of error have been reported in previous studies of transitional regimes. [78] Despite this error, the density, axial velocity, and pressure all qualitatively agree very well along the domain centerline. With these results in hand, the simulation is advanced to Stage II to include the plasma species.

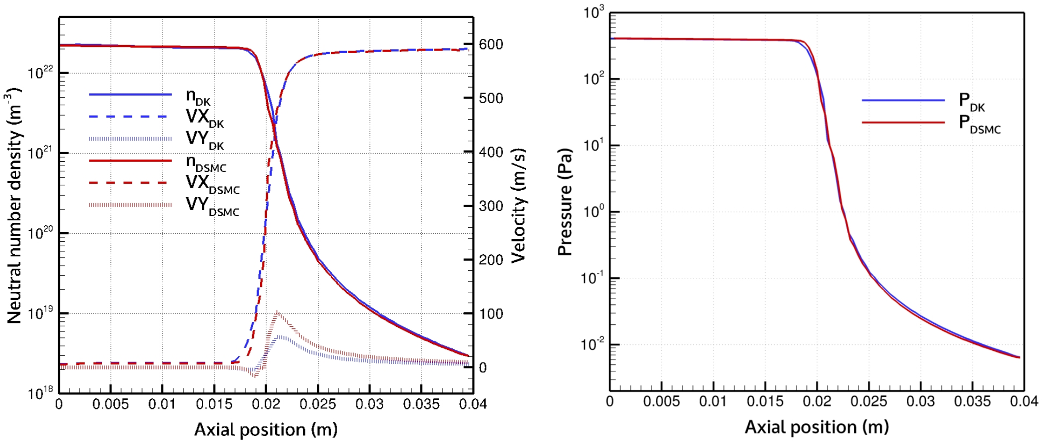

Figure 3.13: Centerline properties for NSTAR neutral flow verification; density and velocities (left), pressure (right). The largest discrepancy is in the radial velocity at the orifice, where the gas rapidly expands. This discrepancy may be attributed to the ES-BGK collision algorithm employed, which is prone to error in transitional flows.

3.3.3 Results: Validation with Experimental Plasma Measurement

In Stage II, ionization is allowed to proceed after steady-state neutral flow is realized. A floor density of ions, $n_{floor} = 1 \times 10^{15} m^{-3}$, is imposed in order to trigger ionization, which then proceeds according to the local neutral density, ion density, and the rate coefficient which depends solely on the local electron temperature (see Equation 2.33). The simulation is allowed to progress until the ion population reaches a steady-state.

The plasma properties found from Stage II are plotted along the domain centerline in Figure 3.14. In this plot, comparisons have been made with both experimental values and numerical values. The experimental values are those taken by Langmuir probe by the Jet Propulsion Laboratory [41], while the numerical data labelled “Fluid” are the results of a multi-fluid hollow cathode code developed at the University of Toulouse. [111, 112] Two cases of the DK code are given here: i) where the Boltzmann relation is used to calculated the local plasma potential (given in blue) and ii) where the potential beyond the orifice is assigned in an attempt to better

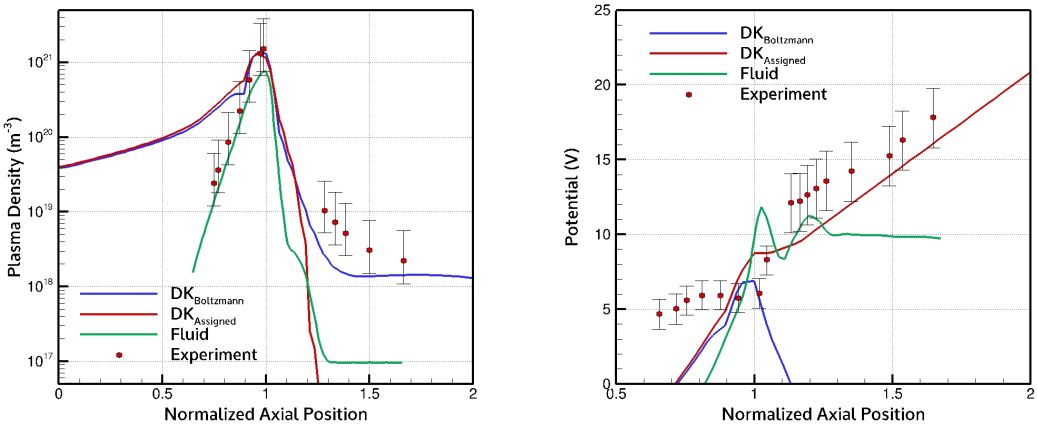

Figure 3.14: Comparison of centerline plasma properties for the NSTAR discharge hollow cathode. Results are plotted versus axial position normalized to orifice entrance. The dots are experimental data taken from Ref. [41], while the green lines are numerical data taken from the code described in Ref. [112].

match experimental data.

The densities given in Figure 3.14 demonstrate that the DK code is only able to achieve good agreement with experiment near the orifice. Upstream of the orifice, the DK code overestimates the density, while downstream, DK underestimates the density. There are a number of reasons for these disagreements: beginning with the upstream (channel) region, the DK code does not include the effects of many other collisions which may be important to the plasma, such as charge-exchange (CEX) collisions. In addition, the plasma sheath is not resolved in the DK simulations, nor are the boundary conditions adjusted to artificially account for the presence of a sheath. Finally, a self-consistent electron model is not used here but rather the Boltzmann relation with an assumed electron temperature; inclusion of a more sophisticated electron model is likely necessary to capture the plasma evolution within the channel. All three of these sets of physics are included in the multi-fluid code used for comparison, which is able to capture a much better agreement with the experimental data.

Downstream of the cathode orifice, neither the DK code nor the multi-fluid code achieve agreement with the data, although the DK code performs better. An important reason for this superior agreement is likely that a fluid description breaks down for both the gas and the plasma beyond the orifice. For the gas, this is because the flow rapidly becomes rarefied outside of the orifice [82], and therefore collisions are too sparse to maintain a Maxwellian distribution. While a fluid description of the plasma may also suffer from this shortcoming, the existence of the ion-acoustic instability in the hollow cathode plume has also been identified. [83] The existence of such an instability further invalidates the use of a fluid model, as its effect on the electron and ion distributions is to drive them further from the Maxwellian distribution (though it should be noted that the code from Ref. [112] has implemented closure models to include the macroscopic effects of the ion-acoustic instability). The DK code used here cannot inherently capture this instability, because the instability is kinetic in nature and thus requires a fully-kinetic (both ions and electrons) description. Such a pursuit will be the focus of Chapter IV.

A further shortcoming of the hybrid-DK model used here is the inability to capture the potential gradient due to the experimental anode. In the experimental setup, the experimental anode is set up as a conical and cylindrical section around the cathode and biased positively to sustain the discharge. Although the boundary value of the potential may be assigned in the Boltzmann relation, a self-consistent calculation of the potential is necessary to capture the potential rise towards the anode. The second DK case aims to remedy this shortcoming by assigning the plasma potential outside of the orifice to increase monotonically. Figure 3.14 demonstrates that while this allows much better agreement with the plasma potential value, it drives down the plasma density to even poorer agreement with experiment. Again, these results demonstrate the need for a self-consistent electron model to better capture the hollow cathode discharge.

Despite the observed discrepancies with the experimental data, it is useful to demonstrate the ability of the DK code to assess keeper erosion rates. High-energy ions, the source of which is thought to be the ion-acoustic instability, are the likely culprit for keeper erosion in hollow cathodes. [60] Given that a fluid description of the ions is insufficient in the plume, a kinetic method such as DK may provide insight into the incident ion energies at the keeper location. For simplicity in these simulations, a keeper is not explicitly included; however, in experiment the keeper is placed around the cathode body and the downstream-facing region is sputtered. Figure 3.15 gives the ion energy distribution functions along a few locations at the radial wall boundary. In this plot, the measured axial ion energies are far below the threshold energy for sputtering molybdenum (a common keeper material) of 30 eV. [49] Therefore, the predicted sputter yield is negligible; this, however, is expected as the ion-acoustic instability is not accounted for in these simulations.

In order to provide an avenue to estimate erosion rates due to the ion-acoustic instability, a closure model must be implemented to provide ion heating. [67] This is beyond the scope of the current study and is thus reserved for future work. Despite currently lacking an ion-heating model to account for the ion-acoustic instability, these results demonstrate the ability of the solver to simulate a hollow cathode system via a hybrid-kinetic approach. This work provides an important milestone towards a predictive hollow cathode simulation by laying the groundwork for the solver. The inclusion of additional relevant physics will aid agreement with experiment in the plume and emitter regions, with the ultimate goal of allowing the solver to predict keeper erosion rates in the future.

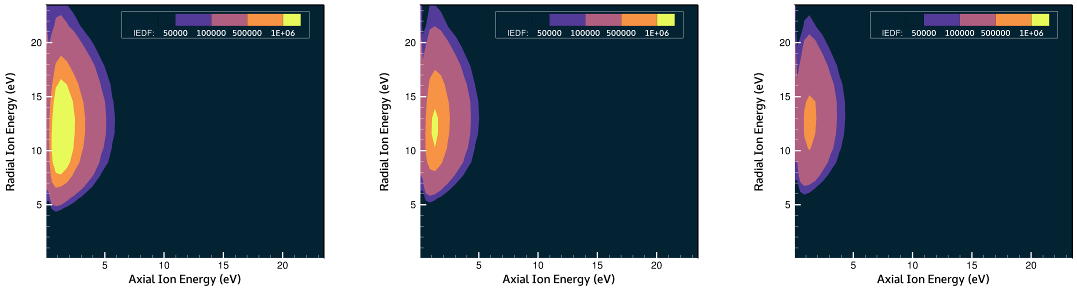

(a) r = 0.65cm (b) r = 0.75cm (c) r = 0.85cm

Figure 3.15: 2V IEDFs along the simulation plume wall boundary, demonstrating the use of the DK method in estimating erosion rates. The axial ion energies are key to erosion estimates of the keeper face; without the inclusion of the ion-acoustic instability, high-energy tails are not observed.

3.4 Summary

In this chapter, analytic solutions of an unsteady, one-dimensional and a steady, two-dimensional axisymmetric rarefied neutral jet flow were used to benchmark the DK method with the DSMC method. Grid convergence studies were conducted, where the level of error was compared with refinement, while the level of error was also compared with the computational wall time necessary to achieve it. It was found that the DK method is better suited for low-dimensional (1D) and unsteady problems, due to its ability to resolve a wide range of velocity space. In higher dimensions, however, the computational cost of DK scales poorly, and particularly for steady problems, the DSMC method becomes more efficient. Unsteady problems in higher dimensions may warrant the cost of DK, especially if the tails of the VDF are important to capturing the physics.

Benchmarking DK with DSMC in 2D-axisymmetric coordinates provided verification for the newly implemented DK solver. The solver was then applied to the simulation of a hollow cathode geometry, where the Boltzmann relation was used to simulate the electrons and the ions were accounted for kinetically. An attempt to validate the solver with experimental data yielded mixed results in which good agreement was found only in the near-orifice region of the cathode. The discrepancy with experiment elsewhere in the domain was attributed to missing physics models in the solver, which are presented as avenues for future work. Finally, ion energy distributions were presented from the results of the hybrid-DK simulations to demonstrate the ability of the solver to provide keeper erosion estimates. To capture high-energy ion formation due to plasma instabilities, closure models for the ion-acoustic instability are crucial but beyond the scope of this thesis; the inclusion of an ion heating model was thus presented as future work.

These results demonstrate important progress towards developing a predictive hybrid-kinetic simulation framework for the hollow cathode system that may ultimately address lifetime estimates through erosion rates. A particularly important next step towards achieving agreement with experiment is the coupling of the solver with closure models for the ion-acoustic instability. The DK code has the distinct advantage of being able to study the ion-acoustic instability directly through fully-kinetic simulations, allowing a benchmarking of the various closure models for the ion-acoustic instability. Therefore, the next chapter in this thesis focuses on the development and consequences of plasma current-carrying instabilities, studied through the lens of deterministic-kinetic simulation.

CHAPTER IV

Plasma Current-Carrying Instabilities

The previous chapter demonstrated the need for a better understanding of the ion-acoustic instability (IAI), which has important consequences for the properties of the hollow cathode plume plasma. Therefore, in this chapter, the deterministic-kinetic method is applied to the study of plasma current-carrying instabilities. This class of instabilities, of which the ion-acoustic instability belongs to, is of importance to a variety of different plasmas. The use of kinetic methods to simulate these so-called micro-instabilities, even in idealized geometries, provides an important piece of the puzzle when attempting to characterize how the plasma behaves macroscopically. In Sections 4.2 and 4.3, one-dimensional (1D1V) and two-dimensional (2D2V) fully-kinetic simulations are carried out to better understand the nature of current-carrying instabilities. A particular emphasis is placed on these instabilities' role in driving enhanced resistivity and high-energy ion formation, which both have important implications for the hollow cathode plume plasma and other classes of current-carrying plasmas. In order to drive towards a predictive, reduced-order model of the hollow cathode, a thorough understanding of the efficacy of their closure models is essential. Further, the rate of production of energetic ions in the cathode plume due to these instabilities must be understood in order to predict keeper erosion rates. Avenues for future work are discussed in light of the results from these analyses.

4.1 The Ion-Acoustic Instability

4.1.1 Theory

The ion-acoustic instability, sometimes called the ion-sound instability, exists in the more general category of current-carrying instabilities which arise when a plasma carries a net current. The IAI is known as a micro-instability, meaning that the effects of the instability depend on the particular structure of the VDF and therefore kinetic simulation is necessary to capture its evolution. This is in contrast to fluid, or macro-instabilities, which depend on the bulk structure of the plasma; the Rayleigh-Taylor and Kelvin-Helmholtz instabilities are well-known macro-instabilities. The IAI has been thoroughly investigated for many decades [13] as it appears in the context of fusion plasmas [21, 76, 117] and space plasmas. [52, 95–97] More recently, there has been renewed interest in the instability as it relates to stimulated Brillouin scattering in plasmas [16,17] as well as its discovery in the hollow cathode device used in electric propulsion. [58, 62]

Many existing forays into numerical simulation of the hollow cathode device have utilized multi-fluid descriptions of the plasma, which inherently cannot capture the formation of the IAI. However, in part due to a lack of agreement with numerical results and experimental data in early multi-fluid cathode simulation attempts by the Jet Propulsion Laboratory, the existence of the IAI in the cathode plume was proposed; indeed, further study found that inclusion of IAI closure models significantly aided agreement with experiment. [83–85] Later experimental efforts to identify ion-acoustic waves in the cathode plume have confirmed their existence, lending further credibility to the theory that the IAI is present in the plume plasma. [61, 62] More recent attempts to model the cathode have found success by increasing the physical fidelity (and complexity) of the IAI closure models from an algebraic closure to a one-equation closure. [94, 111, 112] Given the documented importance of the IAI in the cathode plume, it is prudent to delve into the basic theory of this instability.

To understand the IAI, consider a collisionless plasma with a single ion population and an electron population, both described by equilibrium Maxwell-Boltzmann distributions f_{M_e} and f_{M_i}, which are characterized by temperatures T_e and T_i, respectively. If there is a sufficiently large drift velocity between electrons and ions, $V_e^{'} = V_e - V_i$, the real frequency ω_r and growth rate γ of the resulting plasma waves are given by [21]:

$$\omega_r = \sqrt{k^2 c_s^2 \left(\frac{1}{1 + (\lambda_{de} k)^2} + \frac{3T_i}{T_e} \right)}, \tag{4.1}$$

and

$$\gamma = \sqrt{\frac{\pi}{8}} \frac{k c_s}{(1 + (\lambda_{de} k)^2)^2} \left[\frac{V_e^{'} - c_s}{v_{th,e}} - \sqrt{\frac{m_e}{m_i}} - \left(\frac{T_e}{T_i} \right)^{3/2} \exp\left(- \frac{T_e}{2T_i (1 + (\lambda_{de} k)^2)} \right) \right], \tag{4.2}$$

where c_s is the ion-acoustic speed and k is the wavenumber; see Figure 4.1a for a canonical sketch of an initial configuration of the plasma unstable to the IAI. In a hollow cathode plume plasma, the following hierarchy of velocities often holds: $v_{th,i} \ll c_s \ll V_e \ll v_{th,e}$, such that $V_e^{'} - c_s \approx V_e^{'}$. Defining the electron-to-ion temperature ratio as $\Gamma = \frac{T_e}{T_i}$ and the electron-to-ion mass ratio as $\Pi = \frac{m_e}{m_i}$, and in the limit of small wavenumbers $\lambda_{de} k \ll 1$ and large ion mass, clearer representations for the frequency and growth rate are given as:

$$\omega_r = \sqrt{k^2 c_s^2 \Big(1 + 3/\Gamma \Big)}, \tag{4.3}$$

$$\gamma = \sqrt{\frac{\pi}{8}} k c_s \left[M_e - \Gamma^{3/2} \exp\left(-\frac{\Gamma}{2} \right) \right], \tag{4.4}$$

where $M_e = \frac{V_e'}{v_{th,e}}$ is the electron Mach number. In Equation 4.2, the first term represents inverse electron Landau damping and the second term ion Landau damping.

Thus, it is understood that the IAI is triggered when enough energy exists in the electron drift to excite inverse electron Landau damping and overcome the effects of ion and electron Landau damping. In terms of the necessary values of macroscopic quantities in order for waves to grow, the electron drift V_e' and temperature ratio Γ must be sufficiently large. [119] A few important takeaways from these expressions are: at small wavenumbers, the wave frequency simplifies to $\omega_r \approx k c_s$, and Equation 4.2 admits a simple expression to determine linear stability of the plasma to ion-acoustic waves based on a threshold electron Mach number:

$$M_{thr} = \Gamma^{3/2} \exp\left(-\frac{\Gamma}{2} \right). \tag{4.5}$$

Should the electron Mach number be sufficiently large, generally $M_e > 1.3$, the IAI is superseded by another current-carrying instability known as the Buneman instability. [22] This instability is able to produce larger magnitude plasma waves and may generate abrupt heating of plasma particles. The dispersion relation of the Buneman instability is given by [53]:

$$1 = \frac{\omega_{p,i}^2}{\omega^2} + \frac{\omega_{p,e}^2}{(\omega - k V_e)^2}. \tag{4.6}$$

where $\omega_{p,i}$ is the ion plasma frequency and $\omega_{p,e}$ is the electron plasma frequency. Generally, given the consensus of the IAI's existence in the hollow cathode by the electric propulsion community, [25, 36, 94] the ion-acoustic instability will be the focus in this thesis, but the Buneman instability is also discussed as a possible factor important to the cathode plume.

The ion-acoustic instability generates plasma waves which travel near the ion-acoustic speed. The instability is known to undergo three distinct phases during its evolution: i) linear growth, ii) quasi-linear saturation, and iii) nonlinear saturation. [13,96] In the course of the development of the IAI, the average wave potential amplitude reaches an asymptotic limit in a process known as saturation. This saturation may be described by quasi-linear theory when the growth rate of the instability is larger than the time-rate-of-change of the mean VDF value, $\langle f \rangle^{-1} \partial_t \langle f \rangle < \gamma$. This quasi-linear assumption breaks down when the bounce frequency becomes larger than the growth rate of the wave:

$$\nu_b = \frac{1}{\tau_b} = k\sqrt{e\phi/m_s} > \gamma, \tag{4.7}$$

where ϕ is the wave potential magnitude and m_s is the species mass. [49] The bounce frequency is the rate at which a particle, trapped by an electrostatic potential perturbation, will execute an oscillatory motion within the extent of the perturbation. At the breakdown of the quasi-linear assumption, nonlinear effects become important.

The process of quasi-linear saturation is marked by the formation of a plateau in the electron VDF near the velocity of the ion-acoustic waves. [97] During such a process, the electrons are heated while also losing drift energy, as particles faster than the waves (which are present to a larger degree than those slower than the waves, see Figure 4.1b) are slowed down. At the same time, as there exist more ions with velocities below the wave phase velocity than above, ions interact with the waves by forming a high-energy tail (again see Figure 4.1b). [76] It is precisely this ion tail formation which may be of importance to the hollow cathode system in driving erosion rates. [60]

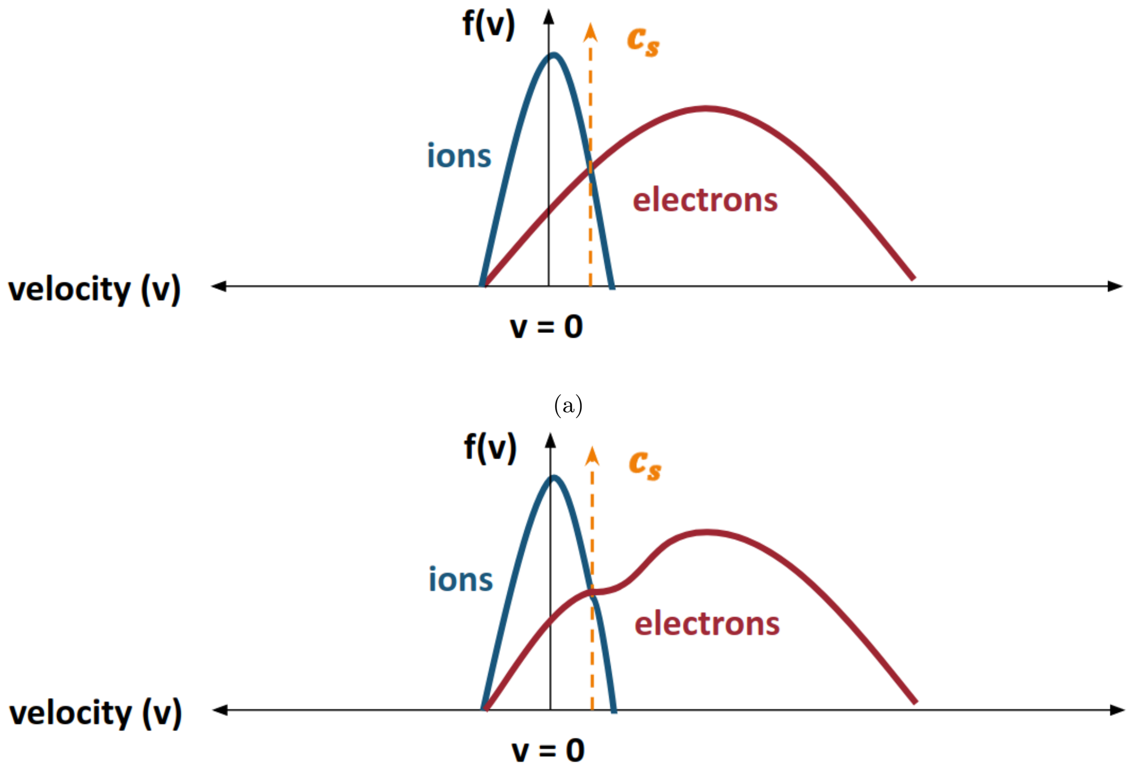

(a)

(b)

Figure 4.1: Velocity space of (a) a system unstable to the ion-acoustic instability and (b) the system during quasi-linear saturation of the instability (b). The ion VDF is given in blue and the electron VDF is given in red, and the ion-acoustic speed is given as the orange line marked c_s. In (b), the electrons demonstrate a plateau near c_s while the ions form a high-energy tail.

Beyond quasi-linear saturation, should the condition of Equation 4.7 be satisfied, nonlinear effects become important. Such nonlinear effects include that of particle trapping [92] and ion resonance broadening [116]. The nonlinear process which dominates depends on the conditions of the plasma. A useful tool in understanding the state of the plasma instability is that of the wave spectrum. Viewing the content of the plasma potential (or electric field) in the frequency domain allows for a deeper understanding of the state of the instability; see Figure 4.2. During the linear growth phase of IAI, analytic theory predicts a fastest-growing mode with wavenumber k. [119] During the quasi-linear saturation phase, a range of wavenumbers are excited and the spectrum broadens while maintaining an apparent peak. Finally, in the nonlinear saturation phase, the spectrum is characterized by a power law decay where the wave energy follows a power law form for large wavenumbers. [62] Thus, the nonlinear state of the IAI is a state of turbulence [17] often referred to as ion-acoustic turbulence (IAT).

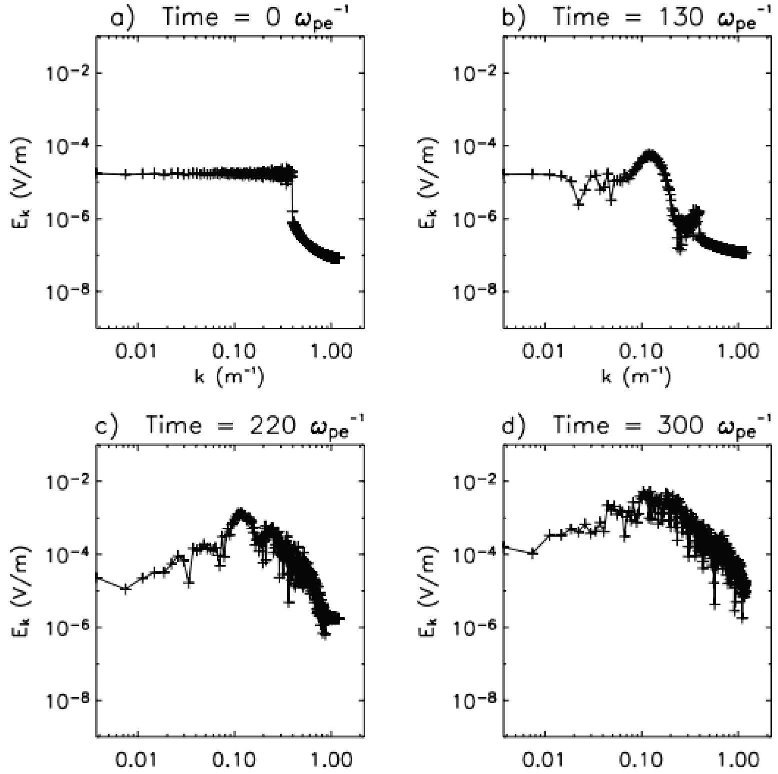

Figure 4.2: Evolution of the electric field spectrum during the course of the ion-acoustic instability. (a) The initial white-noise field spectrum, (b) the linear growth phase with an apparent fastest-growing mode, (c) the quasi-linear saturation phase, and (d) the non-linear saturation phase. Reproduced from Ref. [96] with permission.

4.1.2 IAI Closure Models

The existence of the IAI has consequences for macroscopic properties of the plasma. In order to translate these kinetic effects on the VDFs to changes in bulk properties of the plasma, the concept of an anomalous collision rate, ν_a, is introduced. Even in a collisionless plasma, that is, in the absence of classical particle collisions, ν_a may exist as a result of virtual collisions caused by the presence of plasma waves. This collision term may then be included in fluid plasma models as an additional collision mechanism, supplementing classical collisions between particles. Similar to fluid turbulence theory, there are a variety of levels of fidelity incorporated into these closure models; [99] algebraic (zero-equation) models are the simplest to implement, while one-equation models provide further physical fidelity at the cost of increased complexity.

For the IAI, an initial foray into closure model development was offered by Sagdeev and Galeev, which assumes the instability is in a saturated state: [108]

$$\nu_a^{SG} = \omega_{p,i} \Gamma \frac{V_e}{c_s}, \tag{4.8}$$

This model has been shown to overpredict the collision frequency by many orders of magnitude, and a more popular version of the closure model introduces α, a free parameter that may be tuned to better match experimental data:

$$\nu_a^{SGm} = \alpha \omega_{p,i} \Gamma \frac{V_e}{c_s}. \tag{4.9}$$

This parameter is often set to $\alpha = 10^{-2}$ to achieve better agreement with experiment. [83] An apparent shortcoming of this model is its inability to capture the growth and decay of the instability (due to lack of time-dependence) and an inability to capture the propagation of wave energy (due to lack of spatial-dependence).

More recent attempts to model the hollow cathode plume plasma have applied one-equation models of IAT to simulations. [94, 112] These models concurrently solve a conservation equation for the wave energy, ϵ_W, alongside the plasma simulation, which has spatio-temporal dependence. These equations have the general form:

$$\frac{\partial \epsilon_W}{\partial t} + \nabla \cdot \left(\frac{V_e}{|V_e|} c_s \epsilon_W \right) = 2\gamma \epsilon_W, \tag{4.10}$$

which describes the spatio-temporal evolution of the wave energy, driven by a source term which depends on the growth rate γ. The model used for the IAI growth rate varies; for example, the model used in Ref. [112] assumes the rate of the fastest growing mode γ_F:

$$\gamma_F = \frac{\sqrt{\pi}}{9} \omega_{p,i} \left(\sqrt{\Pi} \left[\sqrt{\frac{3}{2}} M_e - 1 \right] - \Gamma^{3/2} \exp(-\Gamma/3) \right), \tag{4.11}$$

where here collision terms are neglected. Indeed, inclusion of these higher fidelity models has proven effective in capturing dynamic processes in the cathode plume, such as the spot-to-plume mode transition. [36, 87, 111]

4.1.3 Motivating Kinetic Simulations

There exists a notable gap in attempts to understand the possible role of current-carrying instabilities in the hollow cathode plume. While many experimental campaigns have been carried out and reduced-order models have been successfully applied to simulation of hollow cathode devices, there have been few efforts to model the inherently kinetic IAI with the use of kinetic methods. Modeling the IAI in such a way serves to provide an important piece of the hollow cathode puzzle, allowing for a better understanding of the effects on macroscopic properties of the plasma and how non-linear behavior such as particle trapping may affect closure models. This approach has precedence in the broader electric propulsion community, where kinetic simulations have gained traction in recent years as a means of understanding instabilities which may significantly influence bulk properties of the thruster plasma. [9, 18, 88] These simulations are often conducted in idealized geometries, yet still provide valuable insight into the evolution of the instabilities and how they may affect the plasma discharge as a whole.

For example, the ability of kinetic simulations to resolve the spectral content of plasma waves enables a useful tool for probing the wave energy per mode, which may be used to calculate the anomalous collision rate ν_a by [37, 63]:

$$\nu_a = \sum_k \sqrt{\frac{\pi m_i}{2m_e}} \omega_k \left(\frac{q\phi_k}{T_e} \right)^2, \tag{4.12}$$

which utilizes the quasi-linear growth rate for the IAI, assuming the waves are of large wavelength ($k\lambda_D \ll 1$). The terms ϕ_k and ω_k are the wave potential and frequency for a given wavenumber, respectively. Another important question which remains to be solved in the hollow cathode community is that of keeper erosion; while the IAI has been postulated as the source of enhanced erosion rates, formal ties between IAI-enhanced ion energies and erosion rates remain elusive. A recent attempt to kinetically model the current-carrying plasma of a hollow cathode demonstrated the useful nature of kinetic simulations by observing high-energy ion VDF 'tail' formation and using these VDFs to predict erosion rates; notably, significant counter-streaming ion tail formation (ions which would theoretically stream back towards the cathode keeper) was only observed for electron Mach numbers in excess of the threshold for the Buneman instability, $M_e > 1.3$. [49] While this result provides evidence of energetic ion production by current-carrying instabilities, it presents questions about whether the ion-acoustic instability is alone sufficient to explain experimentally measured erosion rates.

In this Chapter, a fully-kinetic approach is taken to study the ion-acoustic instability in detail. The first objective of this chapter is to study the anomalous resistivity of the plasma subject to the IAI and compare with existing closure models used in reduced-order fluid codes. A secondary objective is to investigate the presence of high-energy ion tail formation which could lead to erosion of the cathode keeper. To accomplish the goal of fully-kinetic simulations, the DK Boltzmann solver is coupled to the Poisson solver detailed in Chapter II.

4.2 1D1V Current-Carrying Instability Simulations

4.2.1 Problem Setup

In order to study the ion-acoustic instability with kinetic methods, two types of approaches are considered. The first approach, here referred to as triggered cases, assumes that the plasma electrons begin the simulation with some finite drift corresponding to a Mach number, M_e, that is above the threshold for linear stability given in Equation 4.5. The second approach, referred to as spontaneous cases, applies an external electric field, E_{ext}, to the system in order to accelerate electrons to $M_e > M_{thr}$. In order to prevent E_{ext} from accelerating electrons out of the velocity domain, collisions are included in these spontaneous cases using a BGK operator.

In both triggered and spontaneous cases, even when the electron drift velocity exceeds that of the linear threshold for stability, the noise-free nature of the DK simulations means that there are virtually no electrostatic perturbations in the plasma which would grow in an unstable configuration. In order to initiate the instability in a way that minimizes the effect of an initial perturbation, a white-noise electric field is applied to the system in the form of a superposition of various sinusoidal wavemodes [12]:

$$E(z,0) = \sum_{i=1}^{N_{cut}} E_{tf} \sin(k_i z - \theta_i), \tag{4.13}$$

where N_{cut} is the index of the largest wavenumber k_{MAX}, set to the electron Debye length λ_D, and the smallest wavenumber k_{MIN} is set to the length of the domain. E_{tf} is the thermal noise level, set to $E_{tf} = 1 \times 10^{-10}$ V/m in the simulations herein so as to be much smaller than the electrostatic field strength of the waves generated by the IAI. The phase of each wave, θ_i, is set randomly. The action of the white-noise field is applied to the plasma species as:

$$f_s(z, v) = f_{M_s}(v)(1 + \delta f_s(z, v)), \tag{4.14}$$

where the species distributions are initially assumed to be Maxwellian:

$$f_{M_s}(v) = \sqrt{\frac{m_s}{2\pi k_b T_s}} \exp\left(\frac{m_s(v - U_s)^2}{2k_b T_s}\right), \tag{4.15}$$

and

$$\delta f_s(z, v) = \mp \frac{qE(z, 0)}{m_s} \frac{\partial f_s}{\partial v_z}, \tag{4.16}$$

where s designates the plasma species, T_s is the temperature of species s, and U_s is the initial drift velocity of species s. [125]

For the cases considered here, in addition to any CFL restrictions on the time step, there are important physical restrictions that must be followed to properly resolve the spatio-temporal characteristics of the plasma. The electron Debye length, λ_D, must be resolved such that $\Delta z < \lambda_D$. The electron plasma frequency must also be resolved, such that $\Delta t < \omega_{p,e}$. In order to ease the computational burden of these simulations, a sub-stepping method is employed which utilizes an electron time step Δt_e and a larger ion time step Δt_i. With these restrictions in mind, simulations here are set up with the parameters given in Table 4.1. The only parameters which change between cases are the ion species mass m_i and electron Mach number M_e. All cases are run with periodic boundary conditions.

Table 4.1: Numerical inputs for periodic 1D1V simulation of the ion-acoustic instability.

Physical Cell Size	Δz	$\lambda_d/5$
Electron Velocity Bounds	V_e $(v_{th,e})$	[-6.75,6.75]
Electron Velocity Cell Count	N_{V_e}	1600
Electron Velocity Cell Size	Δv_e $(v_{th,e})$	0.00844
Ion Velocity Bounds	V_i $(v_{th,i})$	[-32,32]
Ion Velocity Cell Count	N_{V_i}	1600
Ion Velocity Cell Size	Δv_i $(v_{th,i})$	0.040
Electron Time Step	Δt_e $(\Delta t\omega_{pe}/2\pi)$	0.0037
Ion Time Step	Δt_i $(\Delta t\omega_{pe}/2\pi)$	0.30
Temperature Ratio	Γ	10

4.2.2 Verification with Drift-Diffusion Model

The spontaneous cases considered here assume two types of collisions are important to the plasma: (i) Coulomb collisions between electrons and ions with a collision rate ν_{ei} and (ii) inelastic collisions between electrons and neutrals ν_{inel}. Both of these collisions are modeled with the BGK collision operator given in Equation 2.5.2. For the Coulomb collisions, the target (equilibrium) distribution drift and temperature are given as [90]:

$$\bar{V}_{ei} = \frac{m_i V_i + m_e V_e}{m_e + m_i}, \tag{4.17}$$

and

$$\bar{T}_{ei} = T_e + \frac{2 m_i m_e}{(m_e + m_i)^2}\left(T_i - T_e + \frac{m_i}{6k_b}(V_e - V_i)^2\right), \tag{4.18}$$

while the inelastic target properties are chosen as:

$$\bar{V}_{inel} = V_e, \tag{4.19}$$

and

$$\bar{T}_{inel} = T_{e_0}, \tag{4.20}$$

where T_{e_0} is the initial electron temperature. Due to this choice of target properties for inelastic collisions, it is important to recognize that the spontaneous simulations do not conserve bulk energy, as the linear addition of energy from the external field E_{ext} is not identically removed by the non-linear BGK collision operator.

However, the advantage of this methodology is that it allows the simulation to reach a steady state in the absence of instability growth. By coupling the BGK collision operators to the 1D1V Boltzmann equation, the 0th, 1st, and 2nd moments provide the fluid conservation equations. Then, the steady-state electron drift velocity and temperature may be found:

$$V_{eq} = \frac{-eE_{ext} + m_e \bar{V}_{ei} \nu_{ei} + m_e \bar{V}_{inel} \nu_{inel}}{m_e \nu_{eff}}, \tag{4.21}$$

and

$$T_{eq} = \frac{2(eE_{ext})^2 + \Big(m_e(\bar{V}_{ei}^2 - V_e^2) + k_b \bar{T}_{ei}\Big) m_e \nu_{ei}^2 + \Big(m_e(\bar{V}_{inel}^2 - V_e^2) + k_b \bar{T}_{inel}\Big) m_e \nu_{inel} \nu_{ei}}{2 k_b m_e \nu_{ei} \nu_{eff}}, \tag{4.22}$$

where $\nu_{eff} = \nu_{ei} + \nu_{inel}$. As the inelastic collision target is set to $\bar{V}_{inel} = V_e$, Equation 4.21 reduces to:

$$V_e = \frac{eE_{ext}}{m_e \nu_{ei}}, \tag{4.23}$$

which is the common drift-diffusion approximation. With knowledge of these steady-

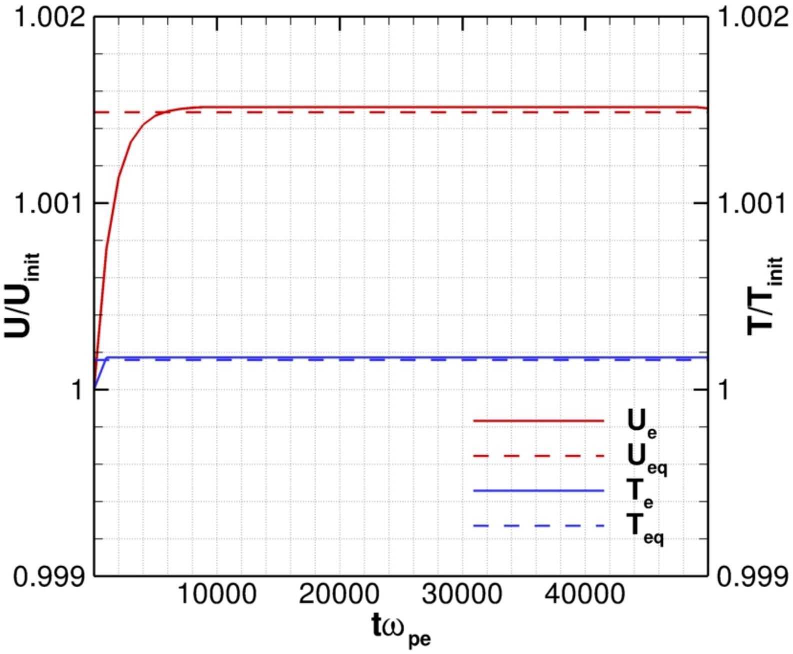

Figure 4.3: Verification of the drift-diffusion assumption for calculation of the anomalous collision frequency for an external field of $E_{ext} = -10$ V/m. Analytic predictions are given as dashed lines while numerical results are given as solid lines.

state values, a verification case is run for electrons, assuming ions form a constant background, to test that the drift-diffusion assumption is valid. An external electric field E_{ext} is imposed and added to the value calculated from Poisson's equation, E_{int}. Electrons are initialized with an initial drift velocity V_{init} and temperature T_{init}. The evolution of the electron values of drift velocity and temperature are compared with the theoretical steady-state values predicted by Equations 4.21 and 4.22. This comparison is given in Figure 4.3. Discretization error in the DK scheme prevents exact agreement with theory, yet the results achieve a steady relative error of $\epsilon_r < .003\%$ and thus demonstrate a satisfactory agreement between the theoretical and numerical results.

The results of Figure 4.3 demonstrate that the drift-diffusion assumption is valid for this system when no instabilities are present. Therefore, any deviation from drift-diffusion theory may be assumed to be a result of instabilities causing anomalous resistivity in the plasma. Thus, to find the anomalous collision rate, the following expression is used:

$$\nu_a = \frac{eE_{ext}}{m_e V_e} - \nu_{ei}. \tag{4.24}$$

Equation 4.24 provides a method to calculate ν_a in simulations with classical collisions, while Equation 4.12 provides a method to calculate ν_a in simulations without classical collisions. Armed with these expressions, kinetic simulations of the IAI may be carried out and the anomalous collision rate compared with closure models.

4.2.3 Results: Anomalous Resistivity

Collisionless simulations of a xenon plasma are run on a domain length of $L = 100\lambda_D$ for electron Mach numbers $M_e = 0.5$, $M_e = 1.0$, and $M_e = 1.5$; as the last value for M_e is above the threshold for transition to the Buneman instability, this case is not be used for analysis of ν_a but is rather to confirm the transition to this instability for $M_e > 1.3$. Figure 4.4 gives the spatially-averaged electrostatic energy, $\langle\epsilon\rangle = \frac{1}{2}\epsilon_0\langle E^2\rangle$, as a function of time during the simulation, demonstrating the increase in energy with increasing M_e. Notably, increasing M_e by a factor of 1.5 from 1.0 to 1.5 results in a larger increase in electrostatic energy in the system than the twofold increase from 0.5 to 1.0. Figure 4.5 gives the plasma potential in a space-time diagram, and demonstrates the increasing wave energy for increasing M_e. [124] In addition, the figure shows that the nature of wave dispersion for the $M_e = 1.5$ case is markedly different than in the cases where $M_e = 0.5, 1.0$. This is expected to be due to the different dispersion relation of the Buneman instability, found in Equation 4.6. Thus this result suggests that, commensurate with previous investigations, the Buneman instability takes hold in the region of $1.0 < M_e < 1.5$.

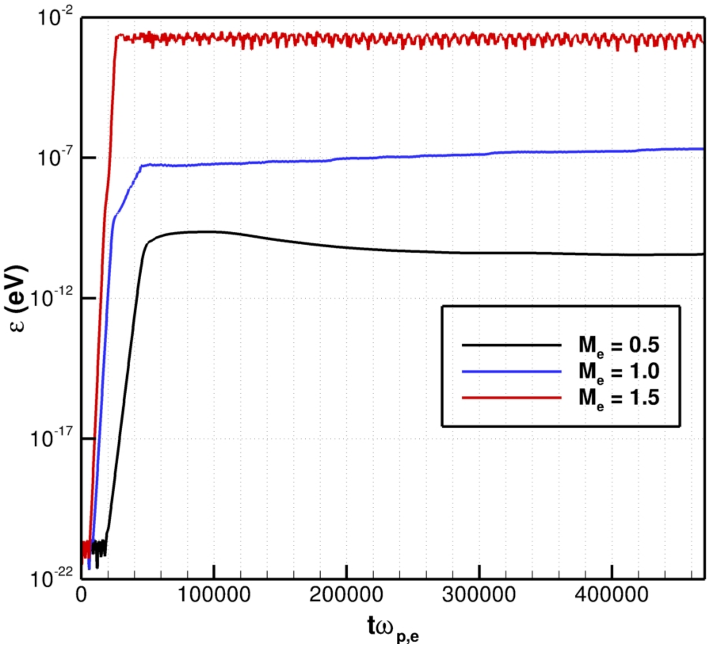

Figure 4.4: Spatially-averaged electrostatic energy against time with increasing M_e for $L = 100\lambda_D$ in a xenon plasma. Note the large increase in wave energy from $M_e = 1.0$ to $M_e = 1.5$, compared with the increase from $M_e = 0.5$ to $M_e = 1.0$.

This transition will be further investigated in Subsection 4.2.4.

Focusing now only on the results from the $M_e = 0.5$ and $M_e = 1.0$ cases, the anomalous collision rate is plotted with time in Figure 4.6 and compared with the Sagdeev-Galeev closure of Equation 4.9. Results are initially taken from the $L = 100\lambda_D$ cases, yet for $M_e = 0.5$ the results for ν_a are orders of magnitude lower than the value predicted by the SG closure. Since an assumption used in calculation of ν_a is that of large wavelengths (see Equation 4.12), the domain length is extended to $L = 2000\lambda_D$ and the cases re-run. For the extended domain, the agreement with the SG closure in the $M_e = 0.5$ case is much improved. For the $M_e = 1.0$ case, however, the agreement becomes poor on the extended domain during the long-time saturation of the instability. A closer investigation of this phenomenon determined that this large secondary increase in ν_a is the result of double layer formation, [125]

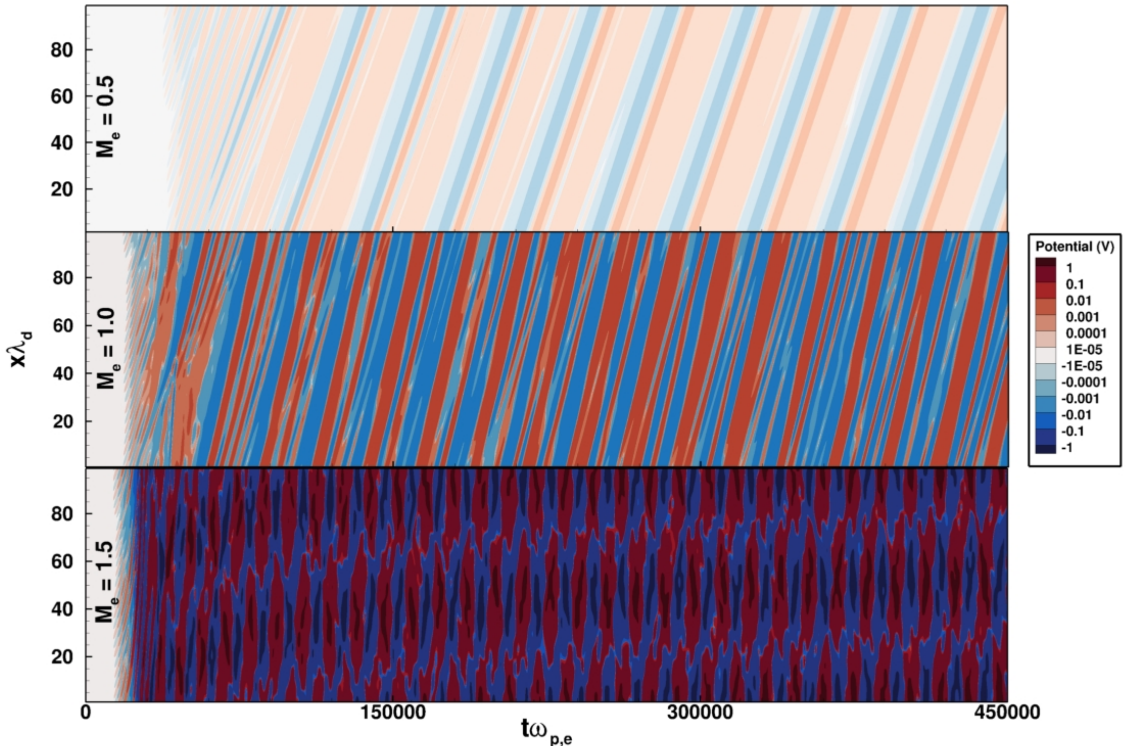

Figure 4.5: Potential space-time diagrams for current-carrying instabilities in a xenon plasma for $L = 100\lambda_D$. The case for $M_e = 1.5$ corresponds to the Buneman instability while the other cases correspond to the ion-acoustic instability. The nature of the wave dispersion becomes much different for the Buneman instability, as expected from Eq. 4.6.

which invalidates the calculation beyond the point of initial saturation marked with a red arrow in Figure 4.6. Nonetheless, ν_a at initial saturation agrees with the SG closure to within a factor of two for the $M_e = 1.0$ case and a factor of four for the $M_e = 0.5$ case. These results suggest that the saturation wave energy, and thus the anomalous collision rate, do not scale linearly with the electron drift V_e; therefore, a dynamic value for α may be necessary to obtain better agreement with the SG closure model, or another closure model may be better suited to capture the proper collision rate.

The large increase in ν_a for extended domain lengths is important to understand from spectral analysis. An FFT of the plasma potential at the point of initial saturation, for all four cases shown in Figure 4.6, is given in Figure 4.7. For both

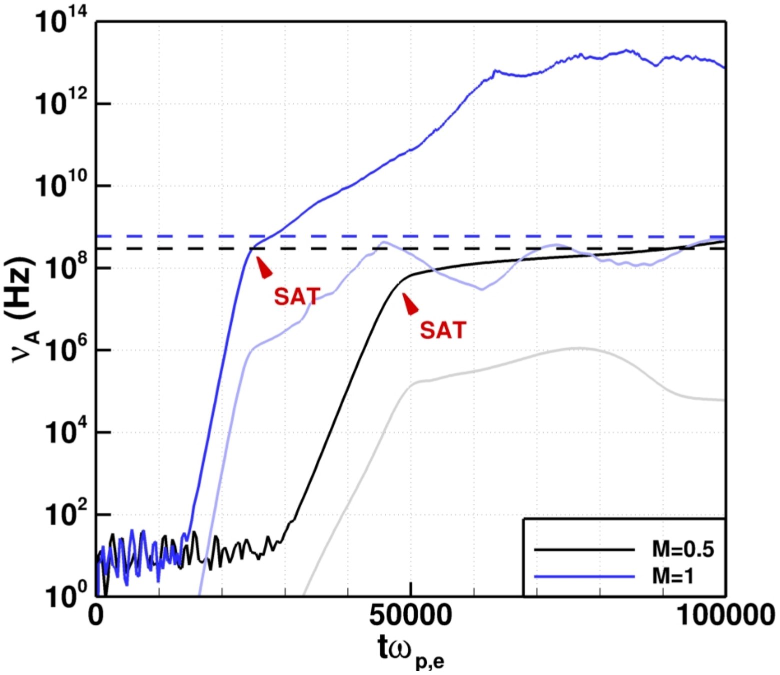

Figure 4.6: Domain-averaged anomalous collision rate due to the ion-acoustic instability in a current-carrying plasma, calculated from Eq. 4.12, for domain lengths of $L = 100\lambda_D$ (light lines) and $L = 2000\lambda_D$ (dark lines). The expected value from the Sagdeev-Galeev closure model (Eq. 4.9) is plotted as the dashed lines for comparison, with $\alpha = 10^{-2}$. Initial saturation is marked by the red arrows.

values of M_e, the extension of the domain length reveals significantly more content at small wavenumbers (large wavelengths) that is not resolved by the $L = 100\lambda_D$ case, indicating the importance of properly resolving such wavemodes. In addition, the nature of the potential spectra differs with an increase in M_e. By comparing with Figure 4.2, it is apparent that the saturation in the $M_e = 0.5$ case is quasi-linear, while in the $M_e = 1.0$ case it is nonlinear, taking on a power law decrement for large wavenumbers. The reason for this change may be attributed to the increase in the average wave energy for $M_e = 1.0$, which would tend more easily to satisfy the condition of Equation 4.7, that trapping effects become important.

The large wavenumber region of Figure 4.7, especially for the $M_e = 0.5$ case, demonstrates what appears to be the presence of wave harmonics. This may be a signature of two-ion decay (TID), a process identified as an important driver for transitioning the ion-acoustic instability to a state of turbulence. [16] A further important aspect of Figure 4.7 is the presence of a secondary peak near $k\lambda_D = 0.1$. This peak was not observed in Figure 4.2 of Ref. [96], and indicates a nonlinear growth of large wavelength modes after initial saturation of the instability. Indeed, this growth is associated with double layer formation, and will be the focus of Chapter V.

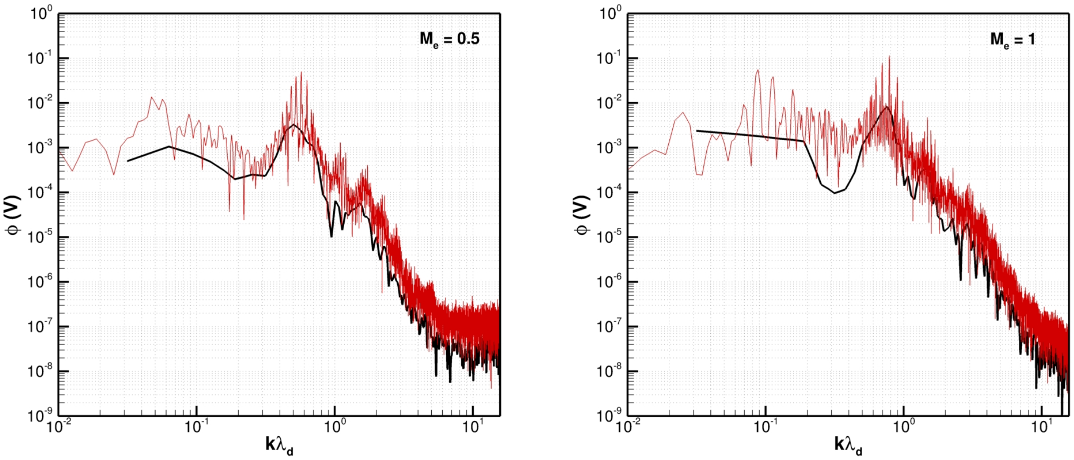

Figure 4.7: Wave potential amplitude spectra at initial saturation. Black lines to the $L = 100\lambda_D$ cases and red lines correspond to the $L = 2000\lambda_D$ cases.

4.2.4 Results: Anomalous Heating and the Buneman Transition

Figure 4.5 demonstrated the transition of the wave dispersion to that of the Buneman instability for $M_e = 1.5$. A commonly accepted notion is that when $M_e > 1.3$, the Buneman instability, rather than the ion-acoustic instability, is active. [22] Additionally, a recent 1D1V numerical study found that beyond this transition point, there is evidence of counter-streaming ion tails which would theoretically impinge upon the hollow cathode keeper. [49] This result has significant implications for hollow cathode keeper erosion, suggesting that the Buneman instability may play an important role in producing the counter-streaming energetic ions necessary to erode the cathode keeper. It is thus important to investigate the ion-acoustic-to-Buneman transition regime of current-carrying instabilities, where $M_e \approx 1.3$. For this purpose, a hydrogen plasma is simulated on a $L = 300\lambda_D$ domain for $M_e = 1.2$. While hydrogen is not usually the propellant for hollow cathode devices in electric propulsion, choosing this ion mass allows for much lower simulation wall times, particularly for higher dimensions. Investigation of a xenon plasma is reserved for future work.

Figure 4.8 gives $\langle \epsilon \rangle$, the spatially-averaged electrostatic energy of the system, atop the spatially-averaged electron VDF, $\langle f_e \rangle$, and the logarithm of the spatially-averaged ion VDF $LOG(\langle f_i \rangle)$, over time. From this figure, it can be seen that once the wave energy begins to saturate, a plateau begins to form in the electron VDF suggesting quasi-linear saturation. As the wave energy further progresses into nonlinear saturation, a secondary peak in the electron VDF appears in the negative velocity direction. This suggests that the system is susceptible to inverse Landau damping of ion-acoustic waves in the negative direction, as the streaming energy of such a secondary peak could provide energy to growth of further, back-streaming ion-acoustic waves. At the same time, the ion VDF demonstrates significant high-energy tail formation with positive velocity, while also developing a smaller high-energy tail with negative velocity. Indeed, the formation of the negative tail in the ion VDF lags that of the positive tail formation by many plasma frequencies, only forming once the electrons exhibit a reflected population in the VDF plateau region and the instability enters nonlinear saturation. The presence of a negative ion tail suggests that counter-streaming waves are present during nonlinear saturation.

To verify whether such counter-streaming waves are present, a spatio-temporal FFT of the system is taken during quasi-linear saturation of the instability and again during nonlinear saturation; Figure 4.9 gives the result of these two FFTs.

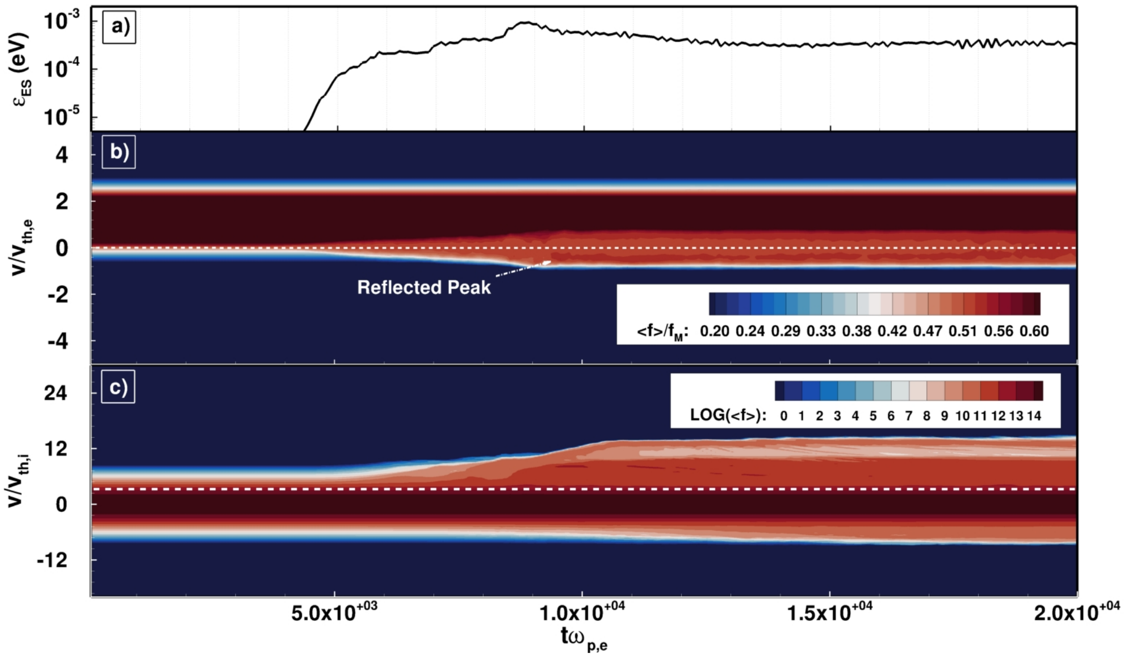

Figure 4.8: Spatially-averaged field energy, electron VDF, and ion VDF plotted with time for a hydrogen plasma with $M_e = 1.2$ on a $L = 300\lambda_D$ domain. Upon nonlinear saturation of the wave energy, there is a signature of a reflected peak in the electron VDF with negative velocity. A high-energy ion tail forms with positive velocity while a smaller tail forms with negative velocity, suggesting counter-streaming waves. The white dashed line gives the ion acoustic velocity, c_s.

The Buneman dispersion relation is solved from Equation 4.6 and the ion-acoustic dispersion from Equation 4.1, and both are overlaid in the plots as BI and IAI, respectively. During quasi-linear saturation, Figure 4.9a demonstrates that there is an ion-acoustic-like signature in the forward direction. During nonlinear saturation, the dispersion becomes much more complex. A fast branch appears in the positive direction, which agrees well with the Buneman dispersion relation. The slow, ion-acoustic-type branch remains as well, and more notably, negative-streaming wave branches are identified. [57] The slow branch in the negative direction agrees reasonably well with an overlaid ion-acoustic dispersion curve marked CS-IAI, while there also appears to be faster wave content that may be related to the Buneman instability.

These results confirm that counter-streaming waves appear for values near the

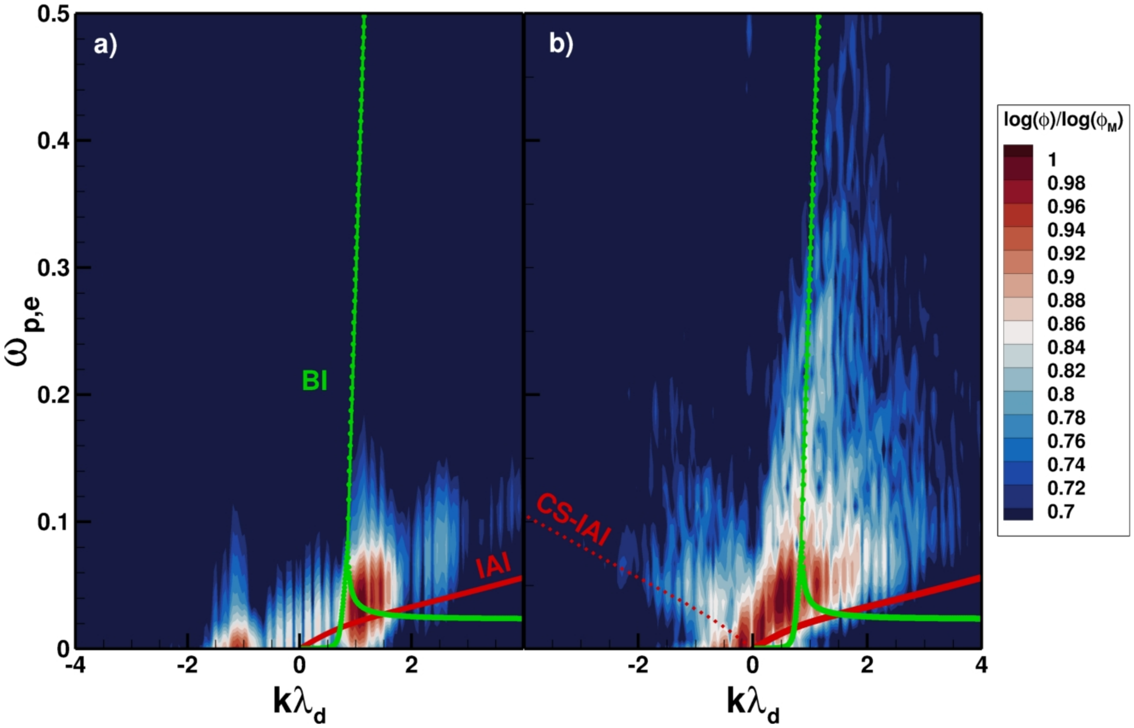

Figure 4.9: Spatio-temporal FFTs of the plasma potential for the hydrogen plasma with $M_e = 1.3$ and $L = 300\lambda_D$. a) is taken during the quasi-linear saturation phase, while b) is taken during nonlinear saturation. The linear dispersion relation for the Buneman instability is overlaid in green (BI) while the ion-acoustic dispersion is given in red (IAI). In b), a counter-streaming ion-acoustic-like wave signature appears and is marked with CS-IAI.

Buneman transition, $M_e \approx 1.3$. The cause for this wave growth is not immediately clear, though due to the appearance only for large wave amplitudes, nonlinear phenomena are the likely culprit. Possible explanations include a negative-mass-instability [24] or the result of wave-wave coupling. [104] The results also demonstrate that the Buneman instability is active for $M_e = 1.2$, below the commonly accepted threshold for this instability. Ultimately, in the context of hollow cathode keeper erosion, these 1D1V results suggest that high-energy counter-streaming ion tail formation is only possible when the Buneman instability is active. However, it is important to recognize that these simulations have been conducted on a 1D1V domain, and therefore may be missing important physics which occurs in higher dimensions. For this reason, these simulations have been extended to consider a 2D2V plasma.

4.3 2D2V Current-Carrying Instability Simulations

The dynamics of current-carrying instabilities in higher dimensions differs greatly from those in one dimension. Early simulations demonstrated that the nature of IAI saturation changes when considering a 2D domain, finding the saturation wave energies to be much larger in 2D [6] and larger still in 3D. [7] This finding was attributed to the growth of off-axis modes (wavemodes which grow at an angle from the direction of the current), which prevent a plateau formation in the electron VDF from being as effective in quenching the instability. This phenomenon has been recently termed the off-axis instability (OAI). [16] Further, later simulations demonstrated that the Buneman instability transitions to the IAI after saturation, yet the effects of this transition are not properly resolved in 1D simulations. [29] Therefore, in this section, 2D2V simulations of the Buneman and ion-acoustic instabilities are conducted in order to provide a comparison with the 1D1V simulations in Section 4.2. A particular emphasis is placed on anomalous heating of ions and electrons due to the instabilities.

4.3.1 Problem Setup

The 2D2V cases are in many respects the same as their 1D1V counterparts, with the numerical parameters detailed in Table 4.2. All cases are 'triggered' by setting the initial electron Mach number $M_{z,e}$ to a linearly unstable value; $M_{z,e}$ is varied between cases, while $M_{r,e}$ is always set to zero. In other words, the electrons are set to drift in only the axial direction so-as to trigger instability. The simulation is seeded with white-noise electrostatic perturbations as detailed in Subsection 4.2.1, simply extended to two dimensions. All boundary conditions are periodic. For these cases, the ion species is hydrogen, as computational requirements are very demanding for higher dimensions. Due to the restrictive computational demands of the problem, the domain size is set to $L_z = 100\lambda_D$ and $L_r = 100\lambda_D$.

Table 4.2: Numerical inputs for doubly-periodic 2D2V simulation of the ion-acoustic instability in a hydrogen plasma.

Axial Physical Cell Size	Δz	$\lambda_d/2$
Radial Physical Cell Size	Δr	λ_d
Electron Axial Velocity Bounds	$V_{z,e}$ $(v_{th,e})$	[-6,6]
Electron Radial Velocity Bounds	$V_{r,e}$ $(v_{th,e})$	[-6,6]
Electron Axial Velocity Cell Count	$N_{V_{z,e}}$	100
Electron Radial Velocity Cell Count	$N_{V_{r,e}}$	100
Electron Velocity Cell Size	Δv_e $(v_{th,e})$	0.12
Ion Axial Velocity Bounds	$V_{z,i}$ $(v_{th,i})$	[-20,20]
Ion Radial Velocity Bounds	$V_{r,i}$ $(v_{th,i})$	[-20,20]
Ion Axial Velocity Cell Count	$N_{V_{z,i}}$	200
Ion Radial Velocity Cell Count	$N_{V_{r,i}}$	200
Ion Velocity Cell Size	Δv_i $(v_{th,i})$	0.2
Electron Time Step	Δt_e $(\Delta t\omega_{pe}/2\pi)$	0.014
Ion Time Step	Δt_i $(\Delta t\omega_{pe}/2\pi)$	0.75
Temperature Ratio	Γ	10

4.3.2 Results: The Effect of Off-Axis Modes

Cases are run for $M_{z,e} = 0.5, 1.0$, and 1.5, which is in excess of the threshold for linear stability of the IAI (in this case, $M_{thr} = 0.236$); in the case of $M_e = 1.5$, this corresponds to the Buneman instability. The spatially-averaged electrostatic energy is plotted in Figure 4.10 for all three cases. In this figure, it is evident that the axial electrostatic energy grows first, while the radial electrostatic energy remains at the initial noise level. This would be expected from linear theory of the IAI, as the electron drift is purely axial. However, after the axial energy has saturated, the radial energy begins to grow and eventually saturates near, but below, the level of the axial energy. This growth of radial energy is attributed to the growth of the OAI. For the $M_{z,e} = 0.5$ case, the radial energy does begins to grow within the time of the simulation, but does not saturate. Due to the computational expense associated with these 2D simulations, the number of time steps is kept small; an extension of the simulation time is needed for all cases considered here and is reserved for future work. Nonetheless, examination of these results provides important insight into the value of higher-dimensional simulations of the IAI.

Analytic formulations of the angular spectrum of the IAI predict that the peak angular wave energy will occur around $\theta_w \approx 35°$, which has been qualitatively verified by PIC simulation. [13] To compare with these observations, a 2D FFT of the spatial content of the plasma potential is taken and the average energy along angles θ_w found; the result of this analysis for the $M_{z,e} = 1.0$ case is given in Figure 4.11. In this figure, the angular spectrum during linear growth of the wave energy and after its saturation is plotted. Before saturation, virtually all of the wave energy is contained in the axial direction ($\theta_w = 0$), while after saturation, an angular distribution is apparent with a peak in energy near $\theta_w \approx 30$. This is in reasonable agreement with

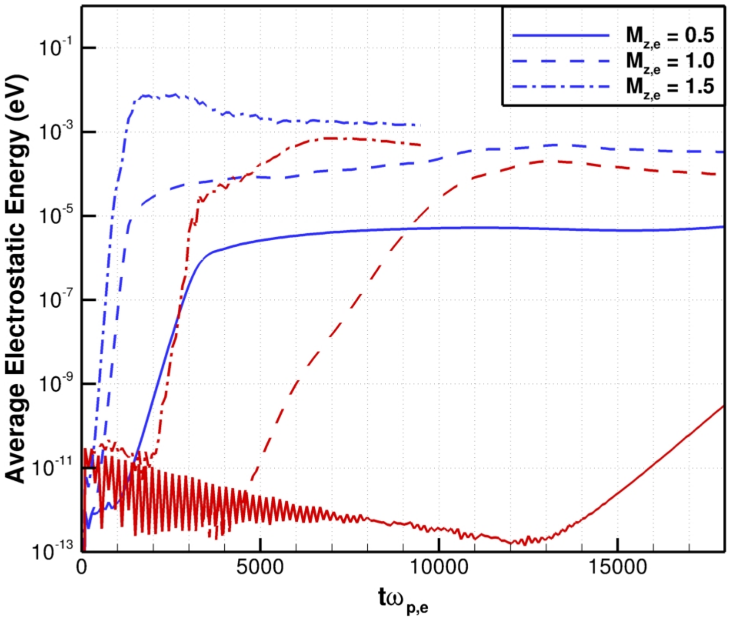

Figure 4.10: Spatially-averaged axial (blue) and radial (red) electrostatic field energy for a hydrogen plasma with $M_{z,e} = 0.5, 1.0$, and 1.5 on a 2D2V domain. Note that the number of time steps is smaller for the $M_{z,e} = 1.5$ case.

the theoretical predictions and prior PIC analysis.

The effect of the OAI on saturation of the instability has significant consequences for macroscopic properties of electrons. The spatially-averaged axial drift velocity and temperature of electrons in the simulation is given in Figure 4.12. Upon saturation of the instability, the electron axial drift velocity drops significantly while the electron temperature simultaneously rises. These are known effects of the ion-acoustic instability as discussed for 1D1V: to drive an anomalous resistivity while heating both electrons and ions. However, in 2D2V these effects are much more pronounced; the 1D1V case from Subsection 4.2.4 is given for comparison, demonstrating the drastic increase in resistivity and heating in higher dimensions.

The overall effect of the resistivity and heating is to drive the electron Mach number below the threshold of linear stability, M_{thr}. Figure 4.13 gives $M_{z,e}$ for the three cases detailed in Figure 4.12, with M_{thr} given for reference. Indeed, in 2D2V,

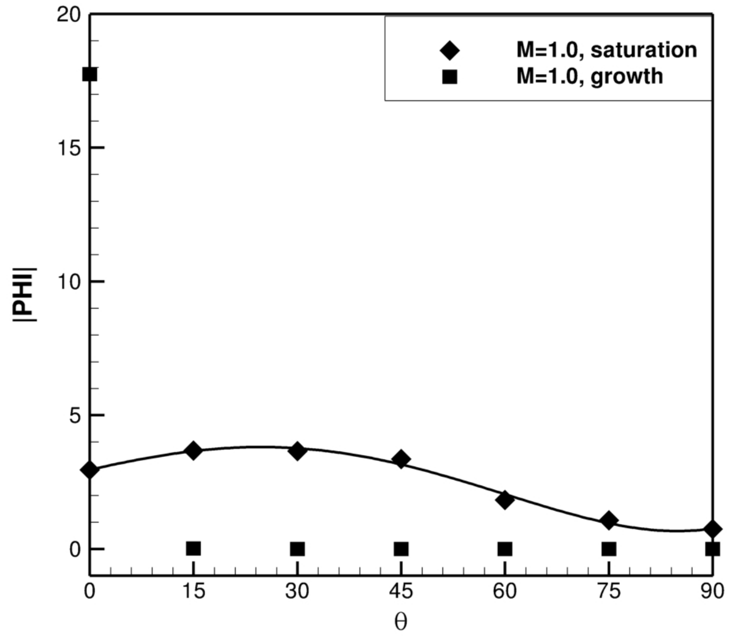

Figure 4.11: Angular distribution of electrostatic wave energy due to the ion-acoustic instability for a hydrogen plasma with $M_{e,z} = 1.0$ on a 2D2V domain. The angle θ is as measured from the purely axial direction.

$M_{z,e}$ is driven below M_{thr}; in 1D1V, however, this is not the case, which has been demonstrated in previous PIC simulations. [6] It is also interesting to note that in the $M_{z,e} = 1.5$ case, the electron Mach number initially declines very rapidly, and is then followed by a more gradual decline similar to the $M_{z,e} = 1.0$ case. This provides evidence that the Buneman instability is rapidly quenched and serves to pre-heat the electrons for transition to the IAI. [28] A calculation of the anomalous collision rate from these 2D2V results is saved for future work; it is important to consider the anomalous collision rate for a xenon plasma as well in order to provide a better analog to the hollow cathode plasma.

It is useful now to observe the evolution of the electron and ion VDFs in 2D2V due to the altered manner of saturation, as this can affect the high-energy ion tail formation (possibly responsible for cathode erosion) as well as the plateau formation

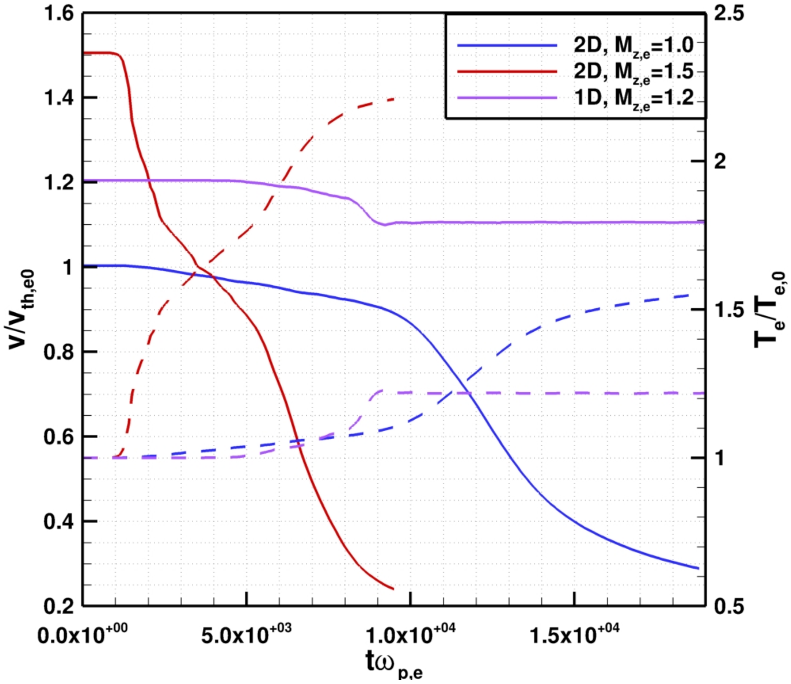

Figure 4.12: Spatially-averaged axial electron drift velocity and temperature for hydrogen plasmas on a 2D2V domain. Drift velocities are given as solid lines while temperatures are given as dashed lines. For comparison, results from the 1D1V $M_e = 1.2$ case are given, highlighting the much larger effect on macroscopic properties in 2D which results from a different saturation mechanism.

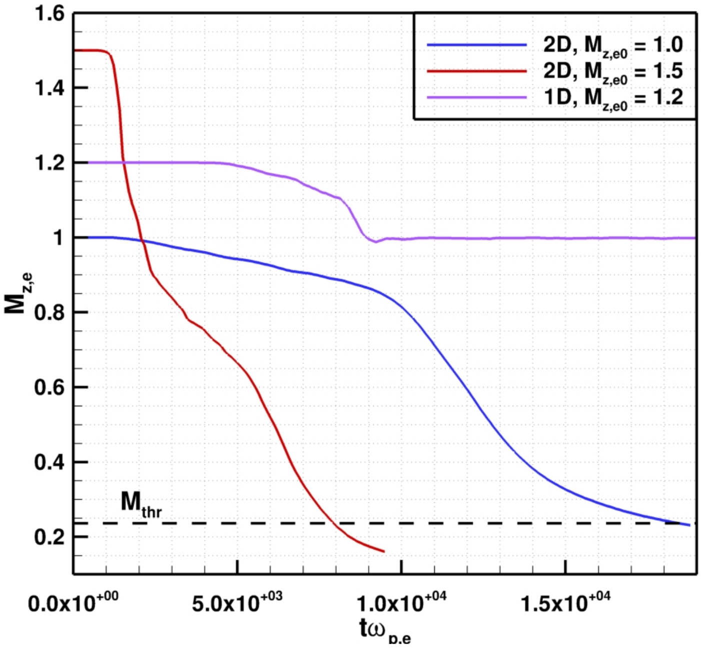

Figure 4.13: Evolution of the axial electron Mach number for a hydrogen plasma in 2D2V. For reference, the 1D1V case of $M_e = 1.2$ is given. The effect of the instability is to drive $M_{z,e}$ below M_{thr} in 2D; 1D simulations do not capture this phenomenon.

in the electrons (which affects the saturation M_e and thus resistivity). For the case of $M_{z,e} = 1.0$, the spatially averaged axial and radial VDFs, for electrons and ions, are plotted in Figures 4.14, and 4.15. In Figure 4.14, it is evident that the axial electron VDF forms a plateau, as in 1D1V, while only the axial electrostatic energy has saturated. However, upon saturation of the radial electrostatic energy, the axial VDF rapidly shifts to lower bulk velocity. At the same time, the radial VDF heats isotropically. This phenomenon is a result of the OAI causing a spread of waves to form, which renders the plateau formation ineffective.

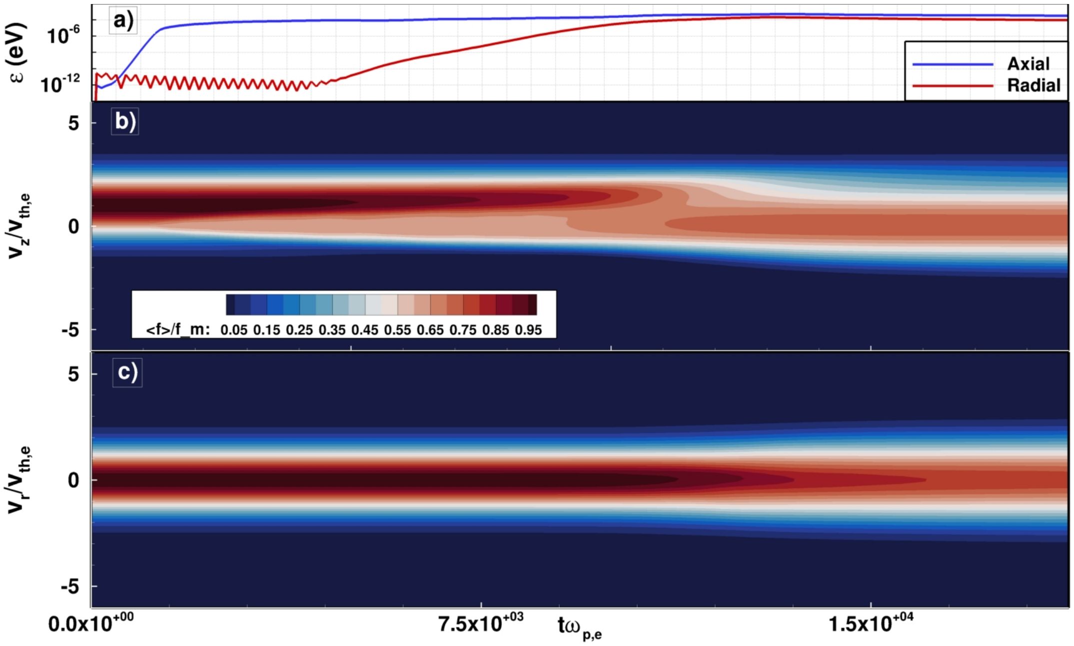

Figure 4.14: Axial (b) and radial (c) spatially-averaged electron VDF given with time for a hydrogen plasma with $M_{z,e} = 1.0$ in 2D2V. The spatially-averaged electrostatic field energies (a) are given as reference. After the axial electrostatic energy has saturated, the axial electron VDF forms a plateau as in 1D1V. Once the radial electrostatic energy saturates, the bulk of the axial VDF rapidly decelerates. At the same time, the radial VDF heats yet remains at near-zero drift.

For Figure 4.15, the axial ion VDF forms a positive axial tail while only the axial electrostatic energy has saturated. Once the radial energy saturates, the positive axial tail becomes more pronounced, while a smaller negative axial tail forms. In the radial VDF, as for electrons, saturation of the radial electrostatic energy causes

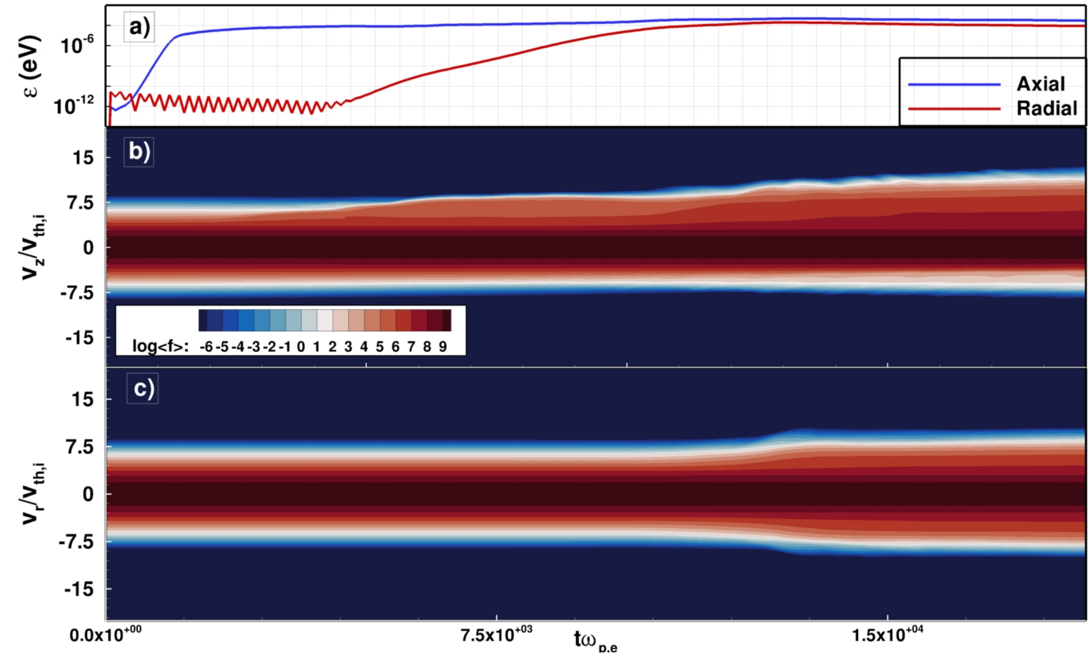

Figure 4.15: Axial (b) and radial (c) spatially-averaged ion VDF given with time for a hydrogen plasma with $M_{z,e} = 1.0$ in 2D2V. The spatially-averaged electrostatic field energies (a) are given as reference. During saturation of the axial electrostatic field, a positive axial tail forms; after the radial electrostatic energy saturates, the positive tail becomes even more pronounced, while a smaller negative tail becomes evident. At radial saturation, the radial VDF heats isotropically.

isotropic heating. It is interesting to note that the ions form a negative axial VDF tail even in 2D2V, and that this tail formation is not necessarily for cases above the Buneman threshold, $M_{z,e} > 1.3$. This counter-streaming tail formation is weak for the case considered here, and indeed for xenon it may be weaker still. However, a further investigation of counter-streaming tail formation in 2D2V kinetic simulations of xenon is important to address the question of cathode keeper erosion and should be considered for future work.

4.4 Summary

In this chapter, current-carrying instabilities of the Buneman and ion-acoustic type were evaluated via deterministic-kinetic simulations. The motivation for these studies was laid out, explaining the gap in kinetic studies of the ion-acoustic instability when addressing anomalous resistivity and energetic ion production for the hollow cathode plasma. 1D1V simulations for a xenon plasma were carried out to compare with the 0D closure model of Sagdeev-Galeev for the anomalous collision rate, finding varying levels of agreement based on domain length and duration of saturation, and motivating the use of more sophisticated, 1D closure models. A later growth of long-wavelength modes was found to be important in the extended domain simulations in 1D1V. Additionally, counter-streaming ion formation was explored for a hydrogen plasma in 1D1V in the Buneman transition regime, finding evidence of counter-streaming ions. The confirmed presence of counter-streaming ions, as found via previous numerical investigations, is of particular importance for predicting hollow cathode keeper erosion rates. Notably, dispersion analysis suggests that the Buneman instability was active for $M_e = 1.2$, below the commonly accepted threshold of $M_e = 1.3$.

The investigations of these instabilities was carried further to 2D2V simulations. Even for a purely axial electron Mach number, $M_{z,e}$, radial field energy growth was observed for all cases considered. This phenomenon has been termed the off-axis instability, or OAI; an analysis of the angular distribution of wave energy found a peak at an angle $\theta \approx 30$ off axial, in agreement with prior investigations. The OAI caused the nature of the ion-acoustic instability's saturation to be significantly altered when compared to 1D1V simulations, with the heating rate and reduction in $M_{z,e}$ far greater in the 2D2V simulations. Contrary to 1D1V simulations, $M_{z,e}$ was found to decrease below the threshold for linear stability M_{thr} in 2D2V. Analysis of the spatially-averaged VDFs in 2D2V demonstrated that plateau formation in the axial electron VDF is disrupted when the radial electrostatic energy saturates, leading to a rapid reduction in the bulk drift energy. Positive axial ion tail formation was observed and found to be bolstered by the growth of the OAI, while a small negative ion tail was observed for $M_e = 1.0$, well below the Buneman instability threshold.

A few avenues for future work were discussed, including a careful analysis of the anomalous resistivity and heating rates in 2D2V simulations. Extension to a xenon plasma is important to provide a better comparison with the hollow cathode plasma, and erosion estimates could then be derived. Finally, an important avenue to consider is the analysis of the wavenumber spectrum in 2D2V. Sophisticated reduced-order models make use of an assumed power-law form of the wave-energy spectrum during saturation, with the exact power depending on the physics driving the spectrum. Kinetic simulations provide an avenue to investigate the spectrum and determine its shape during nonlinear saturation, which could then inform reduced-order modeling efforts and improve their accuracy.

These analyses have provided another angle of attack to the problem of hollow cathode predictive simulation and keeper erosion estimates. By comparing with the Sagdeev-Galeev model used in hollow cathode fluid codes, the importance of benchmarking closure models against the results of kinetic simulation was demonstrated. Further, by having observed generation of high-energy ion tails in 1D and 2D, this work has also demonstrated the utility of kinetic simulations in predicting erosion rates for engineering systems. An extension of this work to quantitative predictions of heating and erosion rates from multi-dimensional kinetic simulations will provide the field with important tools which can be implemented in reduced-order modeling efforts.

CHAPTER V

Weak Plasma Double Layers

Chapter IV revealed that nonlinear saturation of the ion-acoustic instability was capable of generating plasma double layers. Given the existence of the ion-acoustic instability in the hollow cathode plume and the standing need to provide a definitive answer to the problem of keeper erosion, this motivates the need to better understand this phenomenon. Double layers are kinetic in nature and may only be resolved through kinetic simulation. Therefore, in this chapter, Section 5.1 details what a double layer is and the motivations for studying them with respect to the hollow cathode system. In Section 5.2, 1D1V simulations of a current-carrying plasma for extended domain lengths are conducted, enabling the growth of double layers. Phase space analysis, in conjunction with spectral analysis, help to characterize the formation and consequences of double layers in the plasma. In Section 5.3, conclusions are drawn and avenues for future work, particularly in determining their possible connection to the hollow cathode system, are detailed.

5.1 The Plasma Double Layer

5.1.1 Theory

While a plasma is generally considered to be quasi-neutral, there may exist regimes where the plasma is non-neutral on scales larger than the Debye length. One such region is the plasma sheath, which is known to form at the interface of a plasma with a solid object. Electrons tend to be lost to solid boundaries at a much faster rate than their slower ion counterparts, giving rise to a net positive potential of the bulk plasma compared to the solid boundary which spans multiple electron Debye lengths. In this chapter, another potential non-neutral region of plasma is discussed: the plasma double layer.

Contrary to the plasma sheath, the double layer may form in a non-bounded plasma. Similar to the sheath, however, the double layer is characterized by a potential gradient which spans multiple electron Debye lengths. Double layers have been identified in laboratory, [70, 101] from spacecraft measurements, [8, 22] and from numerical simulation. [56, 74] The presence of a localized potential gradient in the plasma results in particle reflections and accelerations, therefore making a double layer inherently kinetic.

Double layers are often split into two distinct classes which depend on their potential magnitude relative to the electron temperature, ϕ_{DL}/T_e. For strong double layers, the ratio $\phi_{DL}/T_e > 1$ while for weak double layers, $\phi_{DL}/T_e \leq 1$. Within weak double layers, there exists a class known as non-monotonic double layers (NDLs), named so because their potential gradient exhibits a non-monotonic structure. [114] This type of double layer has also been termed an ion-acoustic double layer, as it is known to arise from the ion-acoustic instability; this was first demonstrated from simulation and later experimentally verified. [15, 113]

As coherent phase space structures, the formation of non-monotonic double layers from the chaotic state of ion acoustic turbulence remains an open question with various existing interpretations. Generally, this transition of the plasma to an organized state requires a selective growth of small-k modes, as the double layers are found to be of $\mathcal{O}(10\lambda_d)$ wide. Possible mechanisms for this process include the growth of a negative solitary wave, [51] growth of a slow ion acoustic mode, [114] and growth of an ion acoustic wave packet. [3] Each interpretation is subject to apparent inconsistencies; for example, ion acoustic solitons (self-reinforcing waves which propagate at constant velocity) in a single-ion plasma are always compressive (of positive potential), [77] and ion acoustic wave packets are subject to dispersion which tends to damp selective wavemode growth. [3] A more recent study has found that an ion acoustic wave packet may indeed grow selectively at small-k modes should the linear growth rate of the ion acoustic instability exceed that of the packet dispersion rate for a particular k. [45].

In the case of the ion-acoustic double layer, growth begins after saturation of the ion-acoustic instability and initially manifests as growing negative potential wells (see Figure 5.1). The negative potential regions grow in magnitude until they are able to trap ions, resulting in an ion hole(s). At the same time, electrons are reflected off of both sides of the potential well. Since the plasma is current-carrying, however, a greater buildup of electrons occurs on the side opposite the current's direction. This causes a charge imbalance to grow across the potential well, leading to a net potential difference across it and forming an asymmetric ion hole; this asymmetric ion hole is also known as the non-monotonic double layer.

Not all electrons are reflected, however, as some have sufficient kinetic energy to overcome the potential barrier of the double layer. Electrons with sufficient energy are characterized by a cutoff velocity, v_c, given by:

$$v_c = \sqrt{\frac{2e\phi_L}{m_e}}. \tag{5.1}$$

Due to the current-carrying state of the plasma, more electrons streaming in the

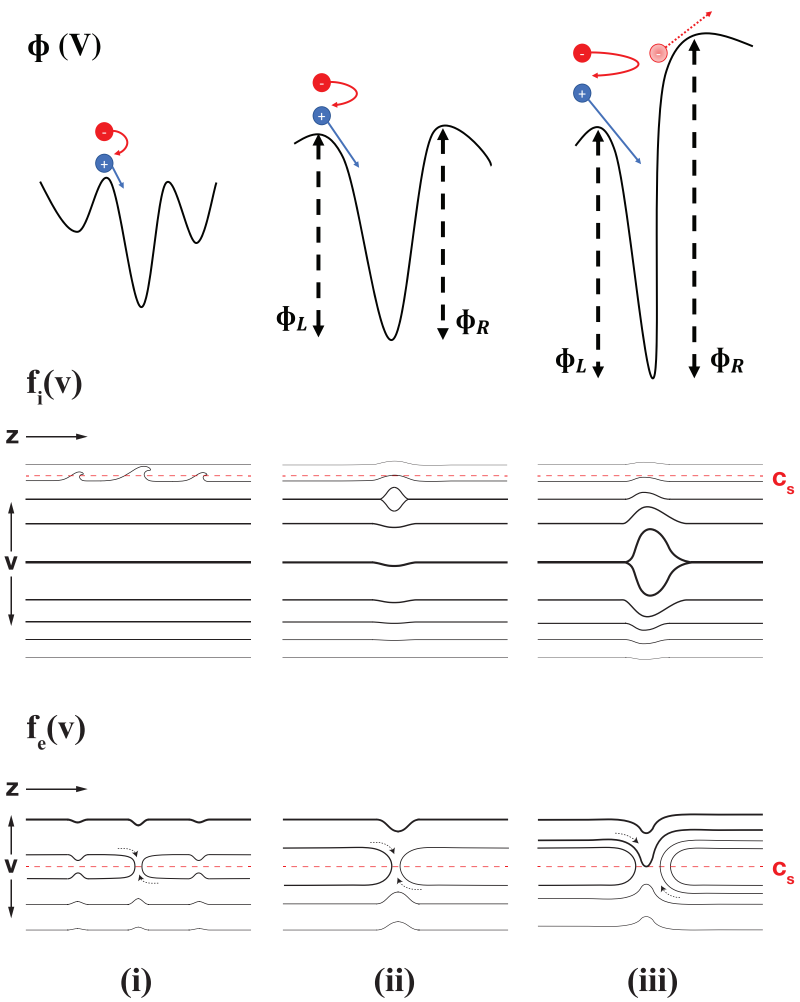

Figure 5.1: Sketch of ion-acoustic double layer growth, considering the plasma potential, ion phase space, and electron phase space. Reproduced from Physics of Plasmas, 27(11), 112303, with the permission of AIP Publishing.

current's direction have the energy required to traverse the asymmetric potential well. The asymmetry of the well leads to a net acceleration of electrons which traverse it in the current's direction, resulting in a two-stream distribution of electrons downstream of the double layer. A simple yet effective expression for the resulting beam velocity of accelerated electrons based on the double layer's potential is given by:

$$v_D = \sqrt{v_c^2 + \frac{2e\phi_{DL}}{m_e}} = \sqrt{\frac{2e(\phi_L + \phi_{DL})}{m_e}} = \sqrt{\frac{2e\phi_R}{m_e}}. \tag{5.2}$$

A two-stream distribution is known to be an unstable configuration in the plasma, resulting in the two-stream instability (TSI). This instability causes plasma wave growth with phase velocity corresponding to the distribution beam velocity, or $\omega/k = v_D$. Therefore, this expression allows for an estimate of the plasma waves which would be generated by the presence of a NDL.

5.1.2 Motivations: Implications for Hollow Cathodes

The implications of these phenomena for hollow cathodes are important to consider, as the ion-acoustic instability is known to exist in the cathode plume. The ion acoustic instability has been investigated as the potential source for this erosion; however, experimental estimates of erosion rates found plasma potential fluctuations in excess of established wave energy limits of the ion-acoustic instability. [84] These oscillations were rather attributed to the ionization instability of the cathode plume mode, which has been linked to the increased resistivity generated by the ion-acoustic instability. On the other hand, a recent 1D numerical investigation of current-carrying instabilities found that high-energy, back-streaming ions are only generated when the electron Mach number M_e is driven to levels associated with the Buneman instability, which is capable of generating larger amplitude plasma waves. [49] Therefore, these investigations both suggest that the ion-acoustic instability alone may not be sufficient to explain measured erosion rates of the hollow cathode keeper. In addition to the Buneman instability and the ionization oscillations of the plume mode, which have been previously investigated, double layers represent another mechanism capable of generating large amplitude potential oscillations which could be important to the hollow cathode plume plasma.

Furthermore, wave measurements in the hollow cathode plume have identified wave packets traveling orders of magnitude faster than the ion acoustic speed. [34,35]

As the NDL has been reported to generate an electron TSI, these waves may provide a possible culprit for these fast-moving waves. The formation of an NDL has been experimentally confirmed for ion and electron temperatures relevant to the hollow cathode [15, 115], while Vlasov [12] and particle [44] simulations have demonstrated that double layers may form with a realistic mass ratio. However, formation of an NDL has not been studied for a xenon plasma, nor has the resulting two-stream instability been characterized and compared with theory. Therefore, in this chapter, the aim is to perform fully-kinetic simulations in order to understand whether an NDL forms for a xenon plasma and, if an electron TSI is observed, quantify the resulting phase speed of the TSI waves in the plasma.

5.2 1D1V Non-Monotonic Double Layer Simulations

5.2.1 Problem Setup

A variety of simulations are carried out to understand whether NDLs form for the heavy ion plasmas of argon and xenon, while also to test the theory relating the NDL potential to generation of an electron TSI. For all of the cases considered here, both ions and electrons are modeled kinetically, according to Equation 2.2, the Vlasov equation. Therefore, the plasma is assumed to be collisionless. The system is assumed to be electrostatic (no magnetic fields are considered) with the electric field calculated self-consistently from Poisson's equation. Boundary conditions are periodic, both for Vlasov's and Poisson's equation. The simulation is initiated according to the same method as in Chapter IV, where the densities of electrons and ions are perturbed by a superposition of white-noise electric fields with random phase.

The simulation conditions given in Table 4.1 are applied here as well, for ions with an artificial mass ratio $m_i/m_e = 50$, as well as hydrogen (these are referred to as the light ions), argon, and xenon (these are referred to as the heavy ions). The domain

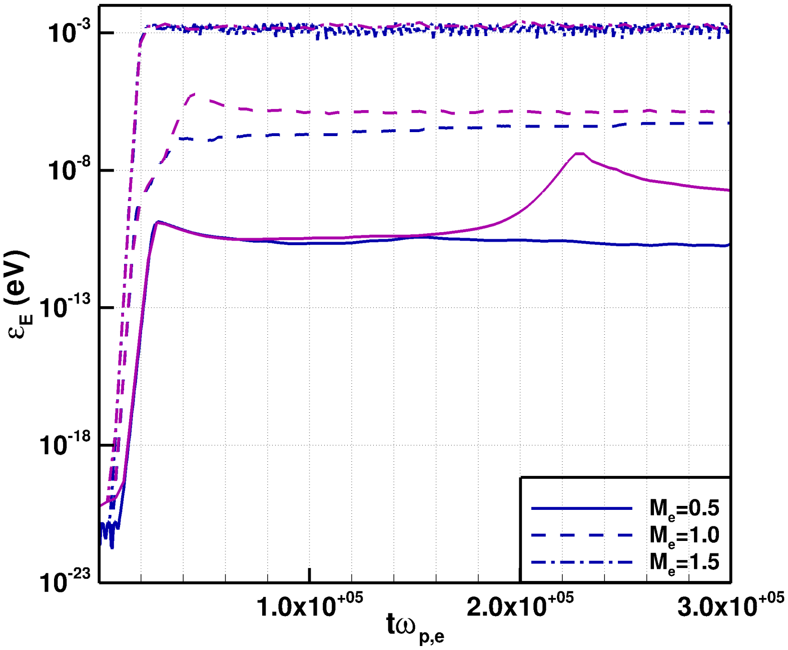

Figure 5.2: Average electrostatic field energy for an argon plasma with varying M_e on the $L = 100\lambda_D$ (blue) and $500\lambda_D$ (purple) domains.

length is varied between $L = 100, 500, 1000$ and 2000 electron Debye lengths, $\lambda_{d,e}$. An initial sweep of cases with varying electron Mach numbers, M_e, is conducted for the argon plasma, the results of which are given in Figure 5.2. In this figure, the spatially-averaged electrostatic field energy is given, defined by: $\varepsilon_E = \frac{1}{2}\langle\epsilon_o|E|^2\rangle$, where ϵ_o is the vacuum permittivity.

In Figure 5.2, it is evident that a secondary growth period in the field energy occurs when the domain length is $L = 500\lambda_D$. The relative magnitude of this secondary growth is most apparent for the lowest Mach number, $M_e = 0.5$, while for the highest Mach number, $M_e = 1.5$, no secondary growth occurs. Therefore, to most clearly study the mechanism(s) behind this secondary growth, the electron Mach number is set to $M_e = 0.5$ in the subsequent cases considered here. This is in excess of the threshold Mach number M_{thr} for linear stability of the ion acoustic instability given in Equation 4.5 for all species considered.

5.2.2 Results: Ion and Electron Phase Space

Figure 5.3 gives the spatially-averaged electrostatic energy, ϵ_E, over the course of all simulations conducted. For all ion species considered and when the domain length exceeds $L = 500\lambda_D$, after the initial growth (Phase I) and saturation (Phase II) of the ion acoustic instability, a secondary growth period occurs (Phase III) followed by a secondary saturation (Phase IV). For the heavy mass ions, this second growth phase occurs with a longer delay than for the light ions; additionally, the secondary saturation occurs at lower energies. Furthermore, for the heavy ions, there does not appear to be an asymptotic limit to the energy at which this saturation occurs, whereas for the light ions, such an asymptote becomes evident.

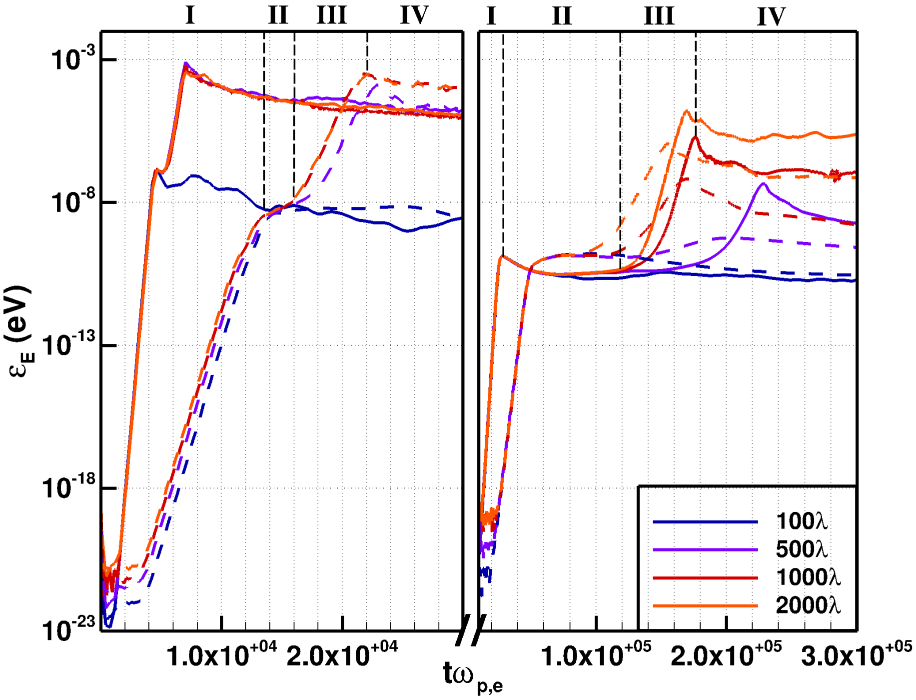

Figure 5.3: Average electrostatic field energy progression for the artificial mass and hydrogen plasmas (left) and the argon and xenon plasmas (right) for an initial electron Mach number $M_e = 0.5$ with varying domain length. The artificial mass and argon lines are bold while the hydrogen and xenon lines are dashed. Reproduced from Physics of Plasmas, 27(11), 112303, with the permission of AIP Publishing.

Examination of ion (Figure 5.4) and electron (Figure 5.5) phase spaces provides evidence that growth of the NDL(s) and the resulting TSI are responsible for this secondary increase in electrostatic energy. The phase space snapshots are taken during growth of the NDL(s), which is marked as Phase III in Figure 5.3. For the ions, this growth begins in Figure 5.4a as perturbations around the ion acoustic speed, c_s. Multiple packets of perturbations, groups of trapping signatures marked by the acceleration of ions, may be seen growing simultaneously. In Figure 5.4b, a single perturbation has grown to become an ion hole, while also slowing down to near zero velocity. A zoomed in view of the ion hole shows that it is asymmetric, meaning there is a net potential difference across it and is therefore also classified as a double layer. The other ion acoustic perturbations appear to separate from the VDF and accelerate positively, evidence of de-trapping of these ions. [107] Finally, in Figure 5.4c, the NDL reverses direction and decays, while the other ion acoustic perturbations further accelerate positively. This analysis of ion phase space suggests, qualitatively, that ion phase space packets are the precursors to the NDL.

For the electrons in Figure 5.5a, the ion acoustic perturbations result in reflections in both the positive and negative velocities. Positive streaming electrons are also accelerated through the potential well of the perturbation packets, resulting in an apparent electron beam associated with each packet. In Figure 5.5b, the largest perturbation, which becomes the NDL, generates a large amount of electron reflection while also resulting in a fast electron beam. Downstream of the NDL's location, a large number of electron holes are observed traveling far faster than the ion acoustic speed, c_s. This is evidence of the TSI initiated by acceleration due to the NDL. Finally in 5.5c, there is no longer a large reflection/acceleration region as the NDL has decayed. There are, however, electron holes still evident which have propagated toward the domain boundary. Additionally, there are electron holes at lower velocities

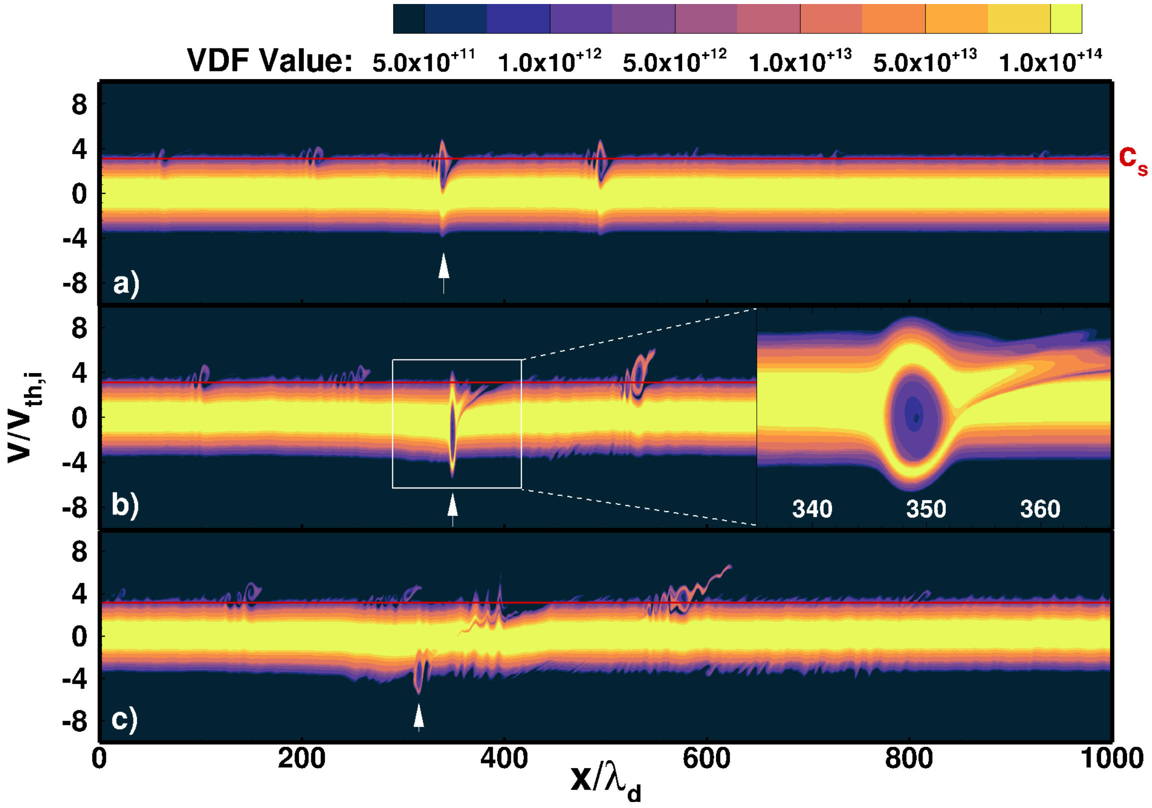

Figure 5.4: Ion phase space showing growth and saturation of the NDL for the artificial mass plasma. a), b), and c) correspond to times of $t\omega_{pe}$ = [6630, 7020, 7410]. In b), a zoom-in of the developed asymmetric ion hole associated with the NDL is given. Reproduced from Physics of Plasmas, 27(11), 112303, with the permission of AIP Publishing.

closer to the location of the decaying double layer, suggesting that the plasma waves from the TSI become slower as the NDL decays in magnitude and generates a slower electron beam.

Observing electron phase space indeed indicates that the electron populations are subject to acceleration by the NDL, resulting in a beam which produces a two-stream distribution. Figure 5.6 gives an example progression of plasma potentials, corresponding with Figures 5.5 and 5.4, which demonstrates the non-monotonic structure of the observed double layers. The maximum potential magnitude of the NDL, along with the expected resulting beam velocity, are compared across a variety of cases in Table 5.1. By measuring the maximum potential magnitude of the NDL in each

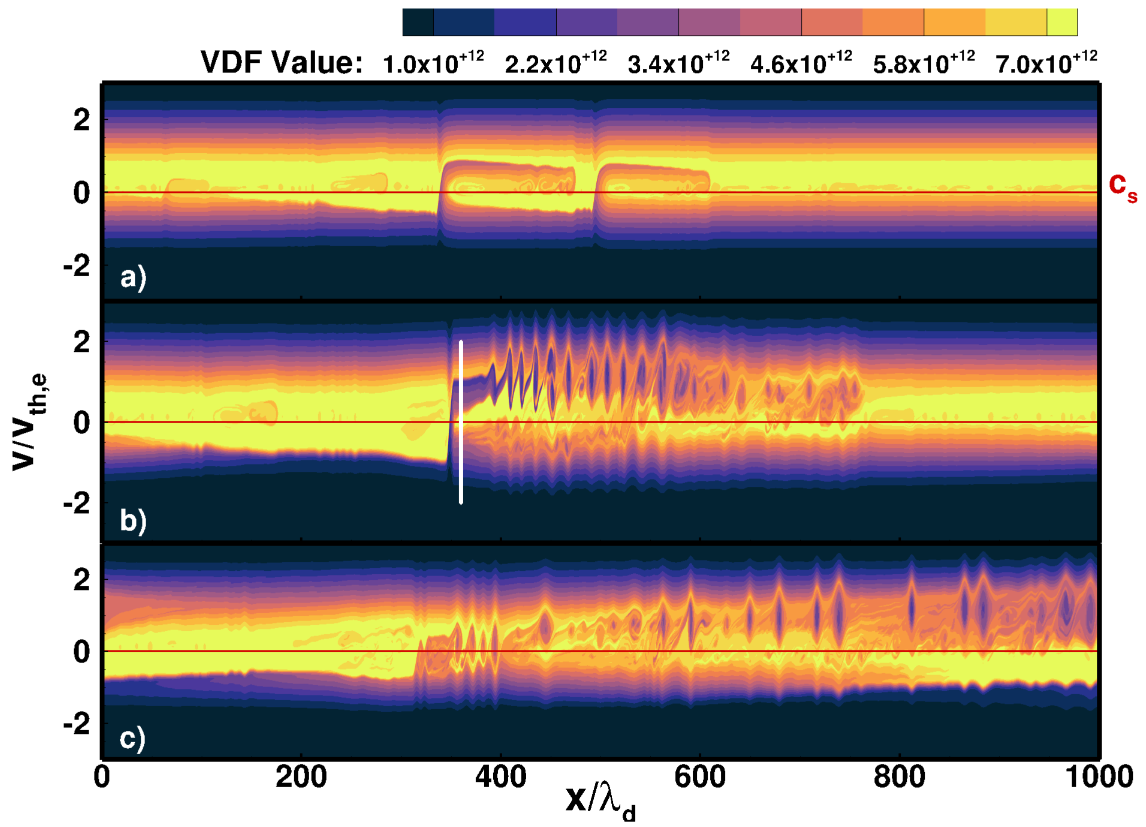

Figure 5.5: Electron phase space showing growth and saturation of the NDL for the artificial mass plasma on the $L = 1000\lambda_d$ domain for $M_e = 0.5$. a), b), and c) correspond to times of tω_{pe} = [6630, 7020, 7410]. The white line indicates the location of the distribution function given in Figure 5.7a. Reproduced from Physics of Plasmas, 27(11), 112303, with the permission of AIP Publishing.

case, it is evident that the light mass ions approach the weak double layer limit of $\phi_R = eT_e$, resulting in a beam velocity which approaches the limit $v_D = \sqrt{2}v_{th}$. For the heavy mass ions, values approaching this limit are not realized for the domain lengths considered, suggesting that longer domain lengths are necessary to determine whether an asymptotic limit exists at or near the weak double layer limit.

Closer examination of 1V electron VDFs downstream of the NDLs, in Figure 5.7, helps to clarify how the TSI forms for a variety of ion masses. For the lighter ions species, a large gap has appeared separating the primary, thermal electron VDF and the beam generated by the NDL. For argon, however, the weaker magnitude of the NDL results in a more modest perturbation which generates a beam with only a frac-

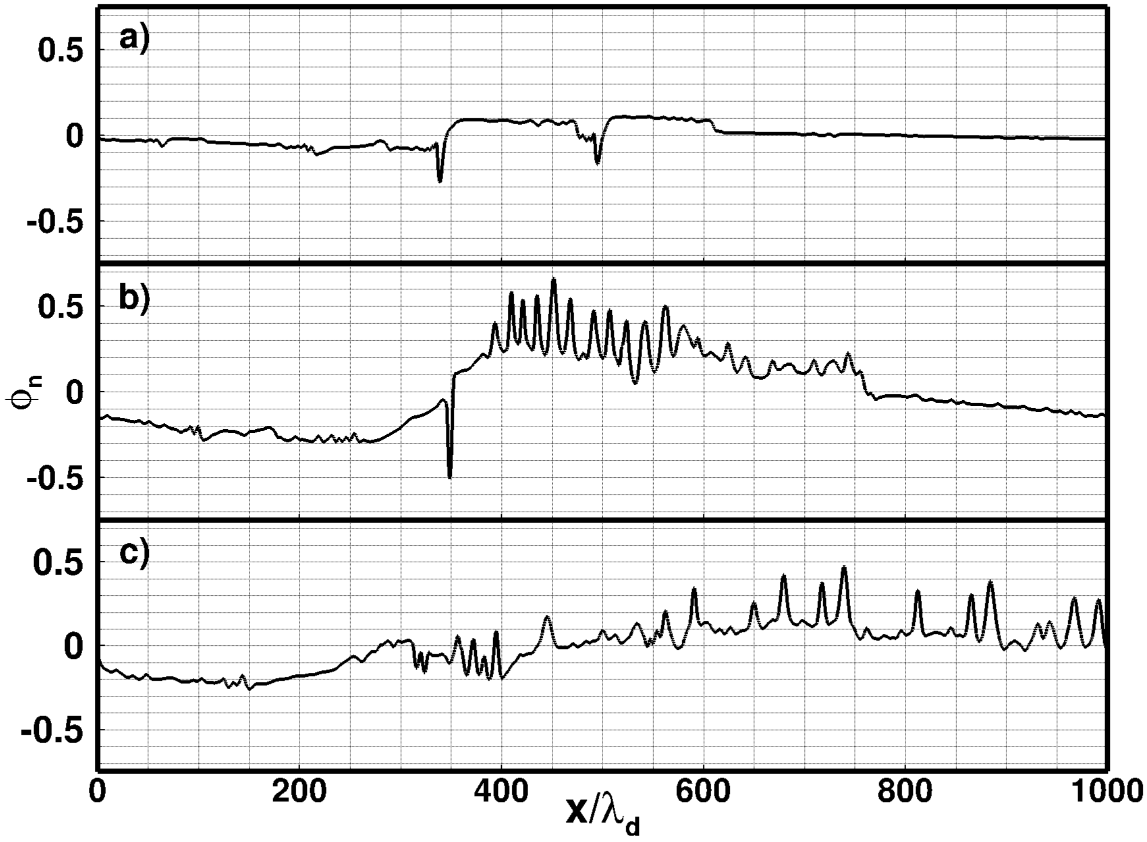

Figure 5.6: Example double layer potential progression corresponding with Figures 5.4 and 5.5. ϕ_n is the normalized plasma potential, $e\phi/T_{e0}$. Reproduced from Physics of Plasmas, 27(11), 112303, with the permission of AIP Publishing.

Table 5.1: Two-stream-driven phase velocity estimates at the time of maximum potential magnitude for the double layer.

Species	L (λ_d)	t$\omega_{p,e}$	ϕ_R (V)	v_D (km/s)
Artificial	1000	6.96×10^3	1.60	750
Artificial	2000	6.96×10^3	1.60	750
Hydrogen	1000	2.24×10^4	1.40	701
Hydrogen	2000	2.24×10^4	1.60	750
Argon	1000	1.76×10^5	8.00×10^{-2}	167
Argon	2000	1.68×10^5	3.00×10^{-1}	325
Xenon	1000	1.62×10^5	1.60×10^{-2}	75.0
Xenon	2000	1.52×10^5	8.00×10^{-2}	167

tion of the electron thermal velocity. The nearly identical two-stream distributions for the artificial mass and hydrogen plasmas suggests that, for a sufficiently long domain, the NDL affects real mass ratio plasmas in the same way as it affects artificial ones. Additionally, it is worth noting that there is a flattening of the electron VDF close to zero velocity which may be a result of both reflection of the back-streaming population by the NDL and trapping by ion-acoustic waves.

5.2.3 Results: Spectral Analysis

With the presence of waves in the system, a great amount of information may be gleaned from analyzing data in the Fourier domain. By doing this, it is possible to determine the phase velocity of waves present in the system, as well as their wavelengths and frequencies. This work utilizes the SciPy FFT library in Python in order to process the data in the Fourier domain. [127] Spatio-temporal Fast Fourier Transforms (FFTs) are taken of the plasma potential data from the artificial mass ratio and argon plasma simulations for the $1000\lambda_D$ domain; these results are plotted in Figures 5.8 and 5.9.

Figure 5.8a gives data taken during Phase II of the simulation, where the only evident signature is found to agree well with the theoretical dispersion for ion-acoustic waves (IAWs) given in Equation 4.1. On the other hand, Figure 5.8b, taken during

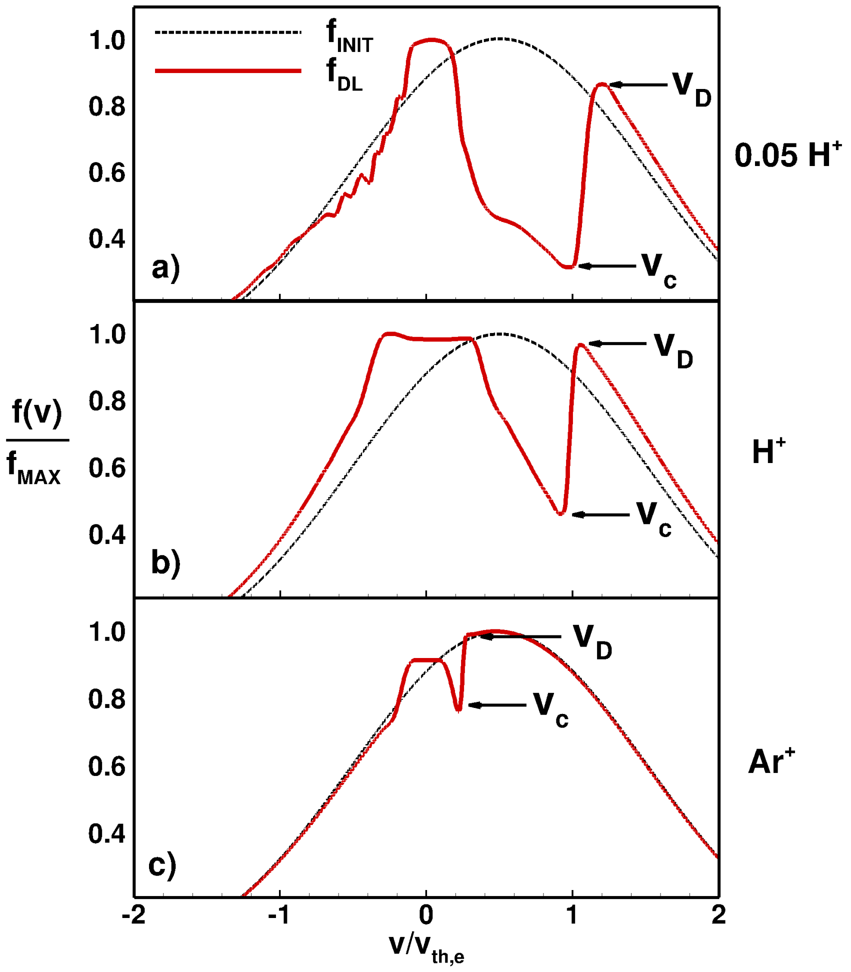

Figure 5.7: Example electron VDFs downstream of NDL for the artificial, hydrogen, and argon plasmas at times tω_{pe} = [7.41×10^3, 2.12×10^4, 1.75×10^5], respectively, for a domain length $L = 1000\lambda_d$. The initial VDF is given as the dashed black line (f_{INIT}), while the VDF downstream of the NDL is given as the solid red line (f_{DL}). All VDFs have been normalized by their maximum value, f_{MAX}. Reproduced from Physics of Plasmas, 27(11), 112303, with the permission of AIP Publishing.

Phase III, has two wave branches. The slower of the two appears nearly identical to that from Phase II: the ion-acoustic branch. The fast branch is compared with the theoretical electron two-stream phase velocity due to the NDL for this case, ω/k = 750 km/s, where good agreement with this theory is found. For Figures 5.9a-b, the same wave branches are evident, though their associated phase velocities are much lower (note the different scaling of the y-axis). Again, the ion-acoustic theory and the NDL-generated TSI theory both agree well with the data. Therefore, these results provide verification for the proposed mechanism of TSI generated by the NDL.

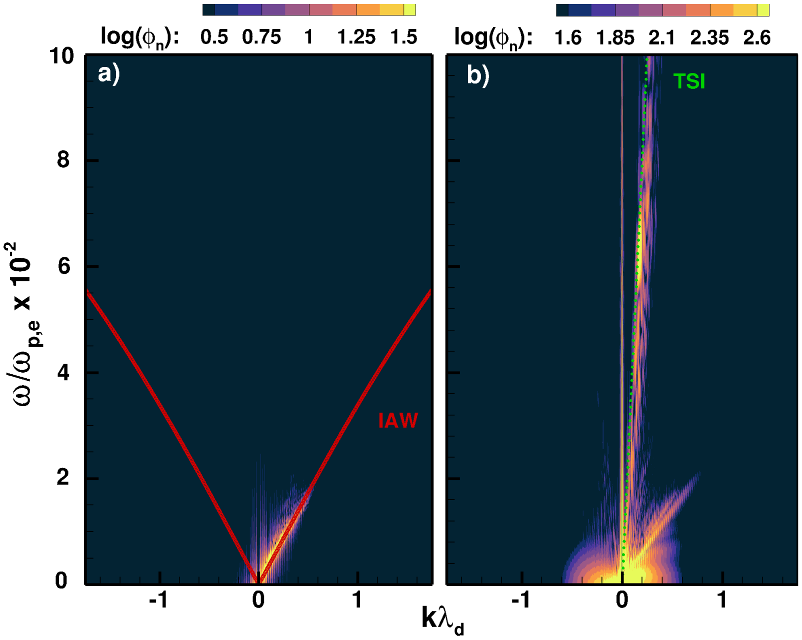

Figure 5.8: Dispersion plots for Phases II (a) & III (b) for the artificial plasma, L = $1000\lambda_d$. The theoretical ion-acoustic dispersion (Eq. 4.1) is plotted in red and marked IAW, while the theoretical two-stream instability dispersion ($\omega = kv_D$) is plotted in green and marked TSI. Reproduced from Physics of Plasmas, 27(11), 112303, with the permission of AIP Publishing.

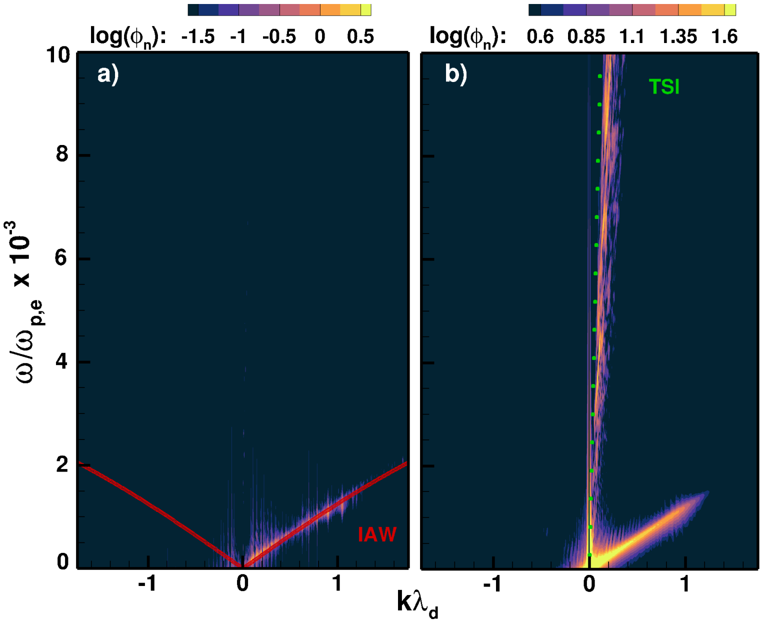

Figure 5.9: Dispersion plots for Phases II (a) & III (b) for the argon plasma, L = $1000\lambda_d$. Note the change in the scale of the y-axis from Figure 5.8. Reproduced from Physics of Plasmas, 27(11), 112303, with the permission of AIP Publishing.

Given the variety of theories regarding NDL formation, it is useful to observe the progression of wavemodes during the growth of the NDL, as this may provide evidence to support any of the existing theories of formation. Figure 5.10 gives the wavemodes in the argon plasma plotted with time in the simulation; the various Phases of the simulation are denoted. In Phase I, the ion-acoustic instability grows, where initially very little wave content is evident; eventually, the plasma enters Phase II when waves with a range of wavenumbers between $k\lambda_d = 0.4$ and $k\lambda_d = 1.6$ grow in strength. During Phase II, there is an apparent transition towards small wavenumber content within the turbulent spectrum around $k_P\lambda_d = 0.1$. This marks the growth of the supposed ion acoustic wave packets, which lead to ion hole formation and eventually the non-monotonic double layer. Later, this process transitions to Phase III, where the NDL has formed. During this phase, the electron TSI is triggered by the presence of the double layer; coupled with the continued growth of the ion acoustic modes, this results in a wide range of strengthening wavemodes. The extended spectrum of waves grow in strength throughout Phase III until reaching a peak, marking the transition to Phase IV.

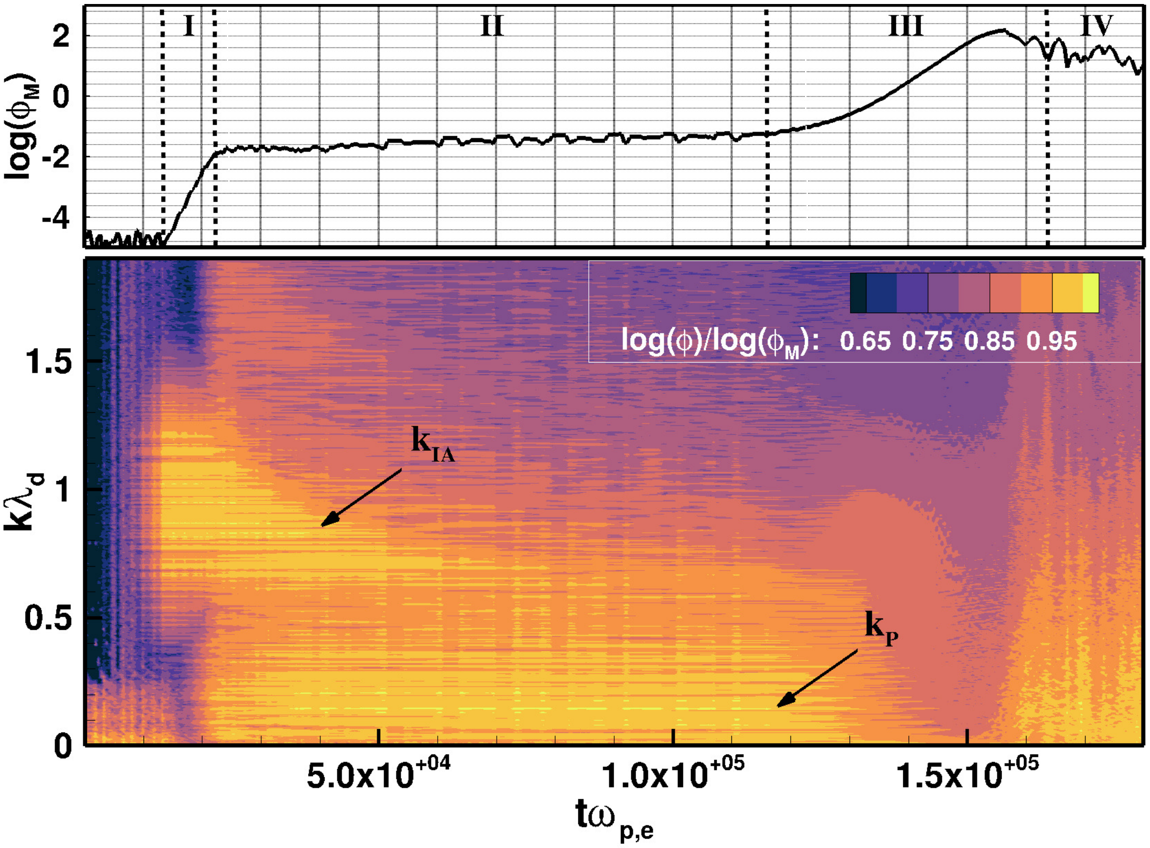

Figure 5.10: Wavenumber analysis for the argon plasma, L = $2000\lambda_d$ and $M_e = 0.5$. Values are normalized by the maximum potential value at each time step, ϕ_M, given in the line plot. Phases corresponding to those marked in Figure 5.3 are denoted by the dashed lines. k_{IA} corresponds to the region of growing wavemodes during linear growth of the ion acoustic instability, while k_P corresponds to the growing wavemodes of the ion acoustic wave packets. Reproduced from Physics of Plasmas, 27(11), 112303, with the permission of AIP Publishing.

5.3 Summary

This chapter described the investigation of the rise of non-monotonic double layers, or NDLs, from a plasma subject to the ion-acoustic instability (IAI). The maximum potential magnitude of the NDL was found to differ for varying ion mass and domain length, and an asymptotic maximum potential near the weak double layer limit was found for the artificial mass and hydrogen, the lightest of the four ion species considered. The initiation of an electron two-stream instability (TSI) due to the presence of an NDL was examined for a variety of ion masses and found to agree well with a derived theoretical prediction. Finally, a Fourier analysis demonstrated the transition to smaller wavenumbers associated with the rise of ion-acoustic wave packets which appeared to lead to the eventual emergence of the NDL.

Avenues for future work with regards to double layer modeling include the use of open-boundary simulations, which would eliminate the confounding effect of recycling due to the periodic boundaries used here. Higher dimensional simulations are also important to undertake, as the formation of double layers in multiple dimensions is known to be suppressed. In addition, the inclusion of a magnetic field is useful to investigate, particularly as the hollow cathode plume is often subject to the magnetic field of a Hall thruster and magnetic fields have been shown to stabilize double layer formation. [2]

NDLs are of possible import to the hollow cathode system, given that the IAI is capable of generating them and their ability to produce large-amplitude plasma waves through spawning an electron two-stream instability. Double layers have not been identified experimentally in the plume of the hollow cathode, and due to their small size and transient nature, their existence may be difficult to prove experimentally.

However, fast-moving waves, whose origin has not been concretely identified, have been observed in the cathode plume. This work has demonstrated that, at least in 1D, ion-acoustic double layer formation is feasible in conditions relevant to the hollow cathode plume plasma. Extension of this work to higher dimensions with more physically realistic boundaries will provide a more definitive prediction of whether these double layers could be sustained in the cathode plume and the role they would then play in keeper erosion

CHAPTER VI

Conclusions

"An expert is a person who has found out by his own painful experience all the mistakes that one can make in a very narrow field."

– Niels Bohr, as quoted by Edward Teller

This thesis set out to advance the predictive modeling capabilities of the electric propulsion discipline through kinetic simulation of expansion flows and current-carrying plasmas. In this chapter, the findings of the thesis are summarized and novel contributions are laid out. Avenues for future work are provided which would further the developments achieved in this thesis.

6.1 Dissertation Summary

The first topic addressed, in Chapter II, was the application of the direct-simulation Monte Carlo method and the deterministic-, or direct-kinetic method. The existing schemes and boundary conditions of these methods were elucidated. Development of a 2D-axisymmetric capability within the DK solver was detailed. For fully-kinetic simulations, the procedure for coupling of Maxwell's equations was given. The addition of two types of collision operators, the BGK and ES-BGK operators, was laid out; further, the process for ionization collisions and a new phase-space mapping algorithm was detailed. With the implementation of various new numerical schemes to the DK framework, a variety of verification problems were undertaken. A manufactured solution for the coupled Poisson's equation solver demonstrated the expected second-order convergence, while application of the coupled DK-BGK solver to the one-dimensional Sod shock tube problem found good agreement with theory. Further, the fully-kinetic, coupled DK-Poisson solver was tested with the Landau damping problem in one- and two-dimensions, again finding good agreement with theoretical values.

The second topic was the application of kinetic methods to neutral gas and plasma expansion flows. Analytic solutions of rarefied gas expansion in one-dimensional and 2D-axisymmetic geometries were used as a benchmark to compare the efficacy of the statistical DSMC method and the determinstic DK method. These simulations demonstrated the useful nature of DK simulations in resolving fine-scales of the VDF, such as the tails, which may dominate in early times of an unsteady expansion. However, the computational efficiency of DSMC proved important in higher dimensions, finding a higher degree of accuracy for significantly less computational expense for the steady 2D-axisymmetric flow.

The DK and DSMC solvers were then used to simulate a hollow cathode geometry, the NSTAR discharge cathode. The Boltzmann relation was described, which is used to calculate the plasma potential in the plasma phase of this simulation. First, DSMC was used to verify the neutral flow results of DK, finding good agreement. Then, from a steady-state neutral flow, the plasma was allowed to evolve; in the plasma phase, DK results were compared with both fluid code results and experimental Langmuir probe data for the plasma density and potential. Agreement was only achieved in the near-orifice region of the cathode; the reasons for disagreement in other regions were discussed, highlighting the importance of the ion-acoustic instability in the cathode plume.

In Chapter IV, fully-kinetic simulations were applied to study plasma current-carrying instabilities; of particular interest was the ion-acoustic instability, known to exist in the hollow cathode plume. One-dimensional simulations were carried out to study the anomalous resistivity and anomalous heating caused by current-carrying instabilities. 1D1V simulations demonstrated the importance of the simulation domain's spatial extent and the electron Mach number, especially when comparing with the algebraic closure model of Sagdeev and Galeev often used in hollow cathode fluid codes. During nonlinear saturation, the case where $M_e = 1.0$ was found to agree well with the closure, while the $M_e = 0.5$ case did not agree with the closure. Extending the domain caused the opposite trend, where the $M_e = 1.0$ case no longer was in agreement with the closure while the $M_e = 1.0$ case was; these results motivate the necessity of further exploring the efficacy of fluid closure models for the ion-acoustic instability.

Further one-dimensional results demonstrated the onset of counter-streaming ion tail formation, the possible culprit for hollow cathode keeper erosion, for a case where $M_e = 1.2$. This region is slightly below the commonly accepted Mach number for Buneman transition, $M_e = 1.3$, and indicates that there is a transitory Buneman instability regime where counter-streaming ion tail formation is possible. Finally, in agreement with previous PIC simulation, two-dimensional simulations of a current-carrying plasma found that the nature of saturation for the ion-acoustic instability vastly differs from the one-dimensional saturation. Rather than the formation of a plateau in the electron VDF, a secondary growth of radial (or off-axis) wavemodes known as the off-axis instability results in an axial-radial isotropization of the electron

VDF. In further agreement with theory and prior PIC simulation, the peak wave energy was found to lie at an off-axis angle of $\theta \approx 35^\circ$.

Chapter V pursued a phenomenon, identified during nonlinear saturation in one-dimensional simulations of the ion-acoustic instability, known as a plasma double layer. The formation of weak double layers, with a potential energy maximum equivalent to the electron thermal energy, was found to be ubiquitous for artificial mass, hydrogen, argon, and xenon plasmas if the physical domain length was sufficiently large. The presence of the weak double layer was found to spawn an electron two-stream instability in all cases considered as well, and a simple theoretical expression was derived to estimate the phase velocity of the resulting plasma waves. Spectral analysis demonstrated the transition from wavemodes characteristic of the ion-acoustic instability ($k\lambda_D \approx 1$) to smaller wavelengths ($k\lambda_D \approx 0.1$), signalling the onset of the double layer; phase space analysis suggested the growth of an ion-acoustic wave packet(s) into ion phase space hole(s) was the precursor mechanism for the double layer.

6.2 Discussion

The work of this thesis was conducted with the goal of realizing predictive simulation of thermionic hollow cathodes used for spacecraft propulsion. Two separate but complementary avenues were pursued towards this end: hybrid-kinetic simulation of the engineering-scale hollow cathode device and fully-kinetic simulation of current-carrying instabilities and resulting plasma double layers which may be important to the operating characteristics of the hollow cathode plume plasma. The hybrid-kinetic platform was applied to simulate the NSTAR hollow cathode, finding, as previous fluid codes have found, that inclusion of closure models for the ion-acoustic instability are crucial to obtaining agreement with experimental measurements. While not yet realized in this work, the utility of the hybrid-kinetic solver developed herein lies in its ability to include a kinetic, ion-heating closure model based on the ion-acoustic instability. The inclusion of such a model, in addition to an anomalous collision closure, would allow this tool to provide useful predictions of erosion rates for the cathode keeper.

Fully-kinetic simulations conducted here demonstrated the use of kinetic simulation in benchmarking existing closure models for conditions relevant to the hollow cathode plasma. The algebraic model of Sagdeev-Galeev was shown to only agree with the kinetic simulation results in certain cases, and demonstrated the need for use of a more sophisticated model. An important capability of kinetic simulation is its ability to identify the dominant saturation process of the ion-acoustic instability; this could then inform development of a new closure model(s) which are more relevant to the hollow cathode plume plasma. Further, this work explored the possible roles of the ion-acoustic and Buneman instabilities in generating high-energy ions which could erode the cathode keeper. Notably, the Buneman instability may play an important role in generating these high-energy ions; in multiple dimensions, previous simulations have shown that the Buneman instability relaxes relatively quickly, preheating the plasma and leading to the ion-acoustic instability. In the cathode plume, it is feasible that the Buneman instability similarly preheats the plasma before the onset of the ion-acoustic instability; the Buneman instability may also be responsible for the fast-traveling plasma waves which have been measured in the cathode plume. The effects of the Buneman instability may be particularly important in the case of the cathode plume mode, where the ion-acoustic instability is known to alternate between activity and inactivity due to ionization oscillations. Further investigations with 2D2V simulations are needed to understand the effect of the Buneman instability and its role in anomalous resistivity as well as driving high-energy ion formation.

Finally, fully-kinetic simulations of the ion-acoustic instability also demonstrated the emergence of non-monotonic double layers during nonlinear saturation of the instability. These double layers were predicted to be approximately $10\lambda_D$ wide, meaning that in the cathode plasma they could measure on the order of microns across and would be very difficult to resolve experimentally. However, measurements of the presence of plasma waves with a phase velocity on the order of the electron thermal velocity may lend credit to the possibility of their existence. Further, measurements of the spectral wavelength content of the cathode plume would help to identify whether there exists a peak in the long wavelength region. However, it is important to run 2D2V simulations of the ion-acoustic instability with an extended domain to determine whether double layer formation still occurs, or whether their prevalence in 1D1V simulations is due to the focusing effect of lower dimensionality.

6.3 Contributions

Here, the contributions which this thesis offers to the greater scientific community are detailed:

- A 2D-axisymmetric deterministic-kinetic solver was implemented, with unique schemes for neutral and charged particles. The solver was verified via comparisons with direct-simulation Monte Carlo as well as an analytic solution for a rarefied jet flow.
- The stochastic kinetic method of direct-simulation Monte Carlo was benchmarked with the direct-kinetic deterministic method via analytic solutions. Grid convergence was demonstrated for both methods and a comparison of compu-

tational cost was conducted.

- The 2D-axisymmetric deterministic-kinetic solver was compared with experimental Langmuir probe data for the NSTAR discharge hollow cathode, finding validation in the near-orifice region while highlighting the importance of properly modeling plasma instability(s) in the cathode plume region.
- Deterministic-kinetic, one-dimensional simulations of the ion-acoustic instability found the efficacy of the Sagdeev-Galeev fluid closure model to vary based on domain length and electron Mach number. Further, the formation of counter-streaming ion tails was attributed to the development of the Buneman instability via phase space and spectral analyses.
- Deterministic-kinetic, two-dimensional simulations of current-carrying instabilities demonstrated a significant deviation in the manner of nonlinear saturation for the ion-acoustic instability by way of the off-axis instability.
- The formation and consequences of weak double layers from the ion-acoustic instability was elucidated via one-dimensional, deterministic simulations. The subsequent development of an electron two-stream instability was identified and characterized via a theoretical expression.

6.4 Future Work

There are many available paths to further the work laid out in this thesis. In this section, some of these possible avenues are detailed.

6.4.1 2D-Axisymmetric Fluid Electron Model

The hollow cathode simulation(s) carried out in Chapter II made use of the Boltzmann relation to calculate the plasma potential, with an assigned electron temperature distribution based on experimental data. For these simulations to further move towards being predictive, a self-consistent electron model is critical. For example, the 2D-axisymmetric electron model developed in Ref. [27] would provide the necessary physics. However, it is important to note that recent efforts have demonstrated the commonly used drift-diffusion approximation in fluid electron models is inconsistent with the physics of the plasma when kinetic energy is large. [47] Therefore, the use of a full-fluid moment model for the electrons may provide more accurate results. [109]

6.4.2 Hybrid-Kinetic Ion-Acoustic Instability Closure Models

The effect of the ion-acoustic instability is critical to obtain the proper physics in the hollow cathode plume plasma. Therefore, with the inclusion of an electron fluid model, the addition of a closure model for the anomalous collision rate due to the ion-acoustic instability is necessary. Ideally, a one-equation model in the form of Equation 4.10 would be incorporated to capture spatio-temporal variation of the ion-acoustic wave energy. Further, as in Ref. [67], the addition of a closure model for ion heating due to the ion-acoustic instability would allow for informed erosion lifetime estimates.

6.4.3 Multiply Charged Ions

Fully-kinetic and hybrid-kinetic simulations detailed in this thesis only considered singly charged ions. Doubly charged ions may play an important role in hollow cathode keeper erosion, being doubly affected by electric field accelerations; they are indeed present in non-negligible concentrations in ion thrusters and Hall thrusters. [33] Though the ion-acoustic instability is believed to be the chief culprit of keeper erosion, the coupling of doubly charged ions with the presence of the ion-acoustic instability has not been investigated and could produce erosion rates higher than previously estimated. Further, the presence of multiply charged ions has been shown to trigger secondary instabilities in recent kinetic simulations. [50] Kinetic simulations including doubly charged ions could provide valuable insight into any such couplings between doubly charged ions and plasma instabilities.

6.4.4 Two-Dimensional, Kinetic Analysis of the Buneman and Ion-Acoustic Instabilities

Chapter IV demonstrated the importance of extending kinetic simulations of the ion-acoustic instability to higher dimensions, as the mechanism for saturation changes significantly and thus affects the evolution of bulk properties at saturation. To be more relevant to the electric propulsion community, the work carried out in this thesis must be furthered by: considering a xenon plasma, measuring anomalous resistivities, and finding erosion rates due to counter-streaming ion tail formation. Further, analysis of the wave energy spectrum to determine the driving mechanism during nonlinear saturation of the ion-acoustic instability would inform deployment of closure models in reduced-order modeling efforts.

6.4.5 Open Boundary Simulations of the Ion-Acoustic Instability

This thesis made use of periodic boundary conditions for simulation of the ion-acoustic instability and resulting non-monotonic double layers. In order to better understand the development of the plasma during nonlinear saturation of the ion-acoustic instability, open boundary simulations are important as they would remove any possible confounding effects of recursion due to periodic boundary conditions. In conjunction with a two-dimensional domain, open boundary kinetic simulations would provide a much closer analog to the physical plasma of the hollow cathode plume, making any conclusions drawn less muddled by computational considerations.

6.4.6 Improving the Computational Efficiency of the DK Method

While leaps in computational power have enabled the use of the DK method for larger and more complex problems, Chapter III demonstrates that it still remains very computationally costly when considering higher dimensional problems. There are a few possible avenues to explore for improving the DK method in this realm: further parallelization and more efficient velocity discretization methods. The DK solver currently utilizes MPI to split the domain purely based on number of axial cells; further parallelizing the code, and using a tool such as METIS to do so automatically, could see large gains in computational efficiency. Further the velocity space discretization is currently uniform; methods such as adaptive mesh refinement [66] or manual refinement based on the relevant physics [30] could save the simulation from utilizing massive amounts of memory.

6.4.7 Implementation of External Grid Loading

Finally, the DK code is currently configured such that only structured, Cartesian grids are possible and these grids must be set up manually. In order to advance the current DK framework such that it may more easily handle a variety of problem types, the capability to accept grids generated in external softwares is critical. Further, implementing a method to handle unstructured grids in physical space would allow the DK solver to tackle problems with complex geometries.

BIBLIOGRAPHY

BIBLIOGRAPHY

[1] M. Arora and P. L. Roe. A well-behaved TVD limiter for high-resolution calculations of unsteady flow. *Journal of Computational Physics*, 132(1):3–11, 1997.

[2] C. Barnes, M. K. Hudson, and W. Lotko. Weak double layers in ion-acoustic turbulence. *Physics of Fluids*, 28(4):1055–1062, 1985.

[3] R. H. Berman, T. H. Dupree, and D. J. Tetreault. Growth of nonlinear intermittent fluctuations in linearly stable and unstable simulation plasma. *Physics of Fluids*, 29(9):2860–2870, 1986.

[4] G. A. Bird and J. M. Brady. *Molecular gas dynamics and the direct simulation of gas flows*, volume 5. Clarendon Press Oxford, 1994.

[5] C. K. Birdsall and A. B. Langdon. *Plasma physics via computer simulation.* IOP Publishing, 1991.

[6] D. Biskamp and R. Chodura. Computer simulation of anomalous dc resistivity. *Physical Review Letters*, 27(23):1553–1556, 1971.

[7] D. Biskamp, K. Von Hagenow, and H. Welter. Computer studies of current-driven ion-sound turbulence in three dimensions. *Physics Letters A*, 39(5):351–352, jun 1972.

[8] L. P. Block. A double layer review. *Astrophysics and Space Science*, 55(1):59–83, 1978.

[9] J. P. Boeuf and M. Takahashi. New insights into the physics of rotating spokes in partially magnetized E x B plasmas. *Physics of Plasmas*, 27(8):083520, 2020.

[10] I. D. Boyd and T. E. Schwartzentruber. *Nonequilibrium gas dynamics and molecular simulation.* Cambridge University Press, Cambridge, 2017.

[11] J. R. Brophy. NASA's deep space 1 ion engine (plenary). *Review of Scientific Instruments*, 73(2 II):1071, 2002.

[12] J. Büchner and N. Elkina. Anomalous resistivity of current-driven isothermal plasmas due to phase space structuring. *Physics of Plasmas*, 13(8), 2006.

[13] V. Bychenkov, V. Silin, and S. Uryupin. Ion-acoustic turbulence and anomalous transport. *Physics Reports*, 164(3):119–215, jul 1988.

[14] C. Cai and I. D. Boyd. Theoretical and Numerical Study of Free Molecular-Flow Problems. *Journal of Spacecraft and Rockets*, 44(3):619–624, 2007.

[15] C. Chan, M. H. Cho, N. Hershkowitz, and T. Intrator. Laboratory Evidence for Ion-Acoustic Type Double Layers. *Physical Review Letters*, 52(20):1782–1785, 1984.

[16] T. Chapman, R. L. Berger, B. I. Cohen, J. W. Banks, and S. Brunner. Longitudinal and Transverse Instability of Ion Acoustic Waves. *Physical Review Letters*, 119(5):1–5, 2017.

[17] T. Chapman, S. Brunner, J. W. Banks, R. L. Berger, B. I. Cohen, and E. A. Williams. New insights into the decay of ion waves to turbulence, ion heating, and soliton generation. *Physics of Plasmas*, 21(4):42107, 2014.

[18] T. Charoy, J. P. Boeuf, A. Bourdon, J. A. Carlsson, P. Chabert, B. Cuenot, D. Eremin, L. Garrigues, K. Hara, I. D. Kaganovich, A. T. Powis, A. Smolyakov, D. Sydorenko, A. Tavant, O. Vermorel, and W. Villafana. 2D axial-azimuthal particle-in-cell benchmark for low-temperature partially magnetized plasmas. *Plasma Sources Science and Technology*, 28(10):105010, oct 2019.

[19] F. F. Chen. *Introduction to Plasma Physics and Controlled Fusion.* Springer International Publishing, third edition, 2018.

[20] G. Chen and I. D. Boyd. Statistical error analysis for the direct simulation monte carlo method. *1995 Fluid Dynamics Conference*, 448(126):1–13, 1996.

[21] R. C. Davidson and N. A. Krall. Anomalous transport in high-temperature plasmas with applications to solenoidal fusion systems. *Nuclear Fusion*, 17(6):1313–1372, 1977.

[22] J. S. DeGroot, C. Barnes, A. E. Walstead, and O. Buneman. Localized Structures and Anomalous dc Resistivity. *Physical Review Letters*, 38(22):1283–1286, may 1977.

[23] S. Dietrich and I. D. Boyd. Scalar and Parallel Optimized Implementation of the Direct Simulation Monte Carlo Method. *Journal of Computational Physics*, 126(2):328–342, jul 1996.

[24] I. Y. Dodin, P. F. Schmit, J. Rocks, and N. J. Fisch. Negative-mass instability in nonlinear plasma waves. *Physical Review Letters*, 110(21):1–5, 2013.

[25] C. A. Dodson, B. A. Jorns, and R. E. Wirz. Measurements of ion velocity and wave propagation in a hollow cathode plume. *Plasma Sources Science and Technology*, 28(6):065009, jun 2019.

[26] M. T. Domonkos, J. E. Foster, M. J. Patterson, and J. George J. Williams. Investigation of Keeper Erosion in the NSTAR Ion Thruster. In *27th International Electric Propulsion Conference*, Pasadena, California, 2001.

[27] H. C. Dragnea. *Development and Application of Multidimensional Computational Models for Hall Thrusters.* Dissertation, University of Michigan, 2018.

[28] C. T. Dum. Anomalous electron transport equations for ion sound and related turbulent spectra. *Physics of Fluids*, 21(6):956–969, 1978.

[29] C. T. Dum and R. Chodura. Anomalous Transition from Buneman to Ion Sound Instability. In *Wave Instabilities in Space Plasmas*, pages 135–147. D. Reidel Publishing, 1979.

[30] N. V. Elkina and J. Büchner. A new conservative unsplit method for the solution of the Vlasov equation. *Journal of Computational Physics*, 213(2):862–875, apr 2006.

[31] V. Fuka. PoisFFT - A free parallel fast Poisson solver. *Applied Mathematics and Computation*, 267:356–364, sep 2015.

[32] C. Galitzine and I. D. Boyd. An analysis of the convergence of the direct simulation monte carlo method. *Journal of Computational Physics*, 289:196–223, 2015.

[33] A. D. Gallimore, J. L. Rovey, and D. A. Herman. Erosion processes of the discharge cathode assembly of ring-cusp gridded ion thrusters. *Journal of Propulsion and Power*, 23(6):1271–1278, 2007.

[34] M. P. Georgin, B. A. Jorns, and A. D. Gallimore. Experimental Evidence for Ion Acoustic Solitons in the Plume of a Hollow Cathode. In *Space Propulsion Conference*, 2018.

[35] M. P. Georgin, B. A. Jorns, and A. D. Gallimore. Plasma instabilities in the plume of a hollow cathode. In *AIAA Propulsion and Energy Forum*, 2018. Paper no. 4427.

[36] M. P. Georgin, B. A. Jorns, and A. D. Gallimore. Correlation of ion acoustic turbulence with self-organization in a low-temperature plasma. *Physics of Plasmas*, 26(8):82308, 2019.

[37] M. P. Georgin, B. A. Jorns, and A. D. Gallimore. Time-varying non-classical electron resistivity in a hollow cathode plume. In *AIAA Propulsion and Energy Forum*, Indianapolis, 2019. Paper no. 4079.

[38] M. P. Georgin, B. A. Jorns, and A. D. Gallimore. Transient non-classical transport in the hollow cathode plume I: measurements of time-varying electron collision frequency. *Plasma Sources Science and Technology*, aug 2020.

[39] S. Godunov. Finite difference method for numerical computation of discontinuous solutions of the equations of fluid dynamics. *Matematicheskii Sbornik*, 47(89)(3):271–306, 1959.

[40] D. M. Goebel, K. K. Jameson, I. Katz, and I. G. Mikellides. Energetic Ion Production and Keeper Erosion in Hollow Cathode Discharges. In *29th International Electric Propulsion Conference*, 2005. Paper no. 266.

[41] D. M. Goebel, K. K. Jameson, I. Katz, and I. G. Mikellides. Plasma potential behavior and plume mode transitions in hollow cathode discharges. In *30th International Electric Propulsion Conference*, Florence, Italy, 2007. Paper no. 277.

[42] D. M. Goebel, K. K. Jameson, R. M. Watkins, I. Katz, and I. G. Mikellides. Hollow cathode theory and experiment. I. Plasma characterization using fast miniature scanning probes. *Journal of Applied Physics*, 98(11), 2005.

[43] D. M. Goebel and I. Katz. Fundamentals of Electric Propulsion: Ion and Hall Thrusters. *Fundamentals of Electric Propulsion: Ion and Hall Thrusters*, pages 1–507, 2008.

[44] J. Guo, Q. Yang, G. Zhu, and B. Li. A particle-in-cell simulation of double layers and ion-acoustic waves. *Plasma Science and Technology*, 15(11):1088–1092, 2013.

[45] A. M. Hamza. On the development and evolution of nonlinear ion acoustic wave packets. *Annales Geophysicae*, 23(6):2249–2257, 2005.

[46] K. Hara. *Development of Grid-Based Direct Kinetic Method and Hybrid Kinetic-Continuum Modeling of Hall Thruster Discharge Plasmas.* Dissertation, University of Michigan, 2015.

[47] K. Hara. An overview of discharge plasma modeling for Hall effect thrusters. *Plasma Sources Science and Technology*, 28(4), 2019.

[48] K. Hara and K. Hanquist. Test cases for grid-based direct kinetic modeling of plasma flows. *Plasma Sources Science and Technology*, 27(6):065004, jun 2018.

[49] K. Hara and C. Treece. Ion kinetics and nonlinear saturation of current-driven instabilities relevant to hollow cathode plasmas. *Plasma Sources Science and Technology*, 28(5), may 2019.

[50] K. Hara and S. Tsikata. Cross-field electron diffusion due to the coupling of drift-driven microinstabilities. *Physical Review E*, 102(2):23202, 2020.

[51] A. Hasegawa and T. Sato. Existence of a negative potential solitary-wave structure and formation of a double layer. *Physics of Fluids*, 25(4):632–635, 1982.

[52] P. Hellinger, P. Trávníček, and J. D. Menietti. Effective collision frequency due to ion-acoustic instability: Theory and simulations. *Geophysical Research Letters*, 31(10):2–5, 2004.

[53] A. Hirose. On amplitude saturation of Buneman instability and anomalous resistivity. *Plasma Physics*, 20(5):481–485, may 1978.

[54] T. Hokazono, S. Kobayashi, T. Ohsawa, and T. Ohwada. On the Time Step Error of the DSMC. In A. D. Ketsdever and E. P. Muntz, editors, *AIP Conference Proceedings*, pages 390–397. AIP, 2003.

[55] K. Holste, P. Dietz, S. Scharmann, K. Keil, T. Henning, D. Zschätzsch, M. Reitemeyer, B. Nauschütt, F. Kiefer, F. Kunze, J. Zorn, C. Heiliger, N. Joshi, U. Probst, R. Thüringer, C. Volkmar, D. Packan, S. Peterschmitt, K. T. Brinkmann, H. G. Zaunick, M. H. Thoma, M. Kretschmer, H. J. Leiter, S. Schippers, K. Hannemann, and P. J. Klar. Ion thrusters for electric propulsion: Scientific issues developing a niche technology into a game changer. *Review of Scientific Instruments*, 91(6), 2020.

[56] M. K. Hudson, W. Lotko, I. Roth, and E. Witt. Solitary Waves and Double Layers on Auroral Field Lines. *Journal of Geophysical Research*, 88(A2):916–926, feb 1983.

[57] N. Jain, T. Umeda, and P. H. Yoon. Modeling nonlinear development of Buneman instability with linear dispersion theory. *Plasma Physics and Controlled Fusion*, 53(2), 2011.

[58] B. A. Jorns, S. E. Cusson, Z. Brown, and E. T. Dale. Non-classical electron transport in the cathode plume of a Hall effect thruster. *Physics of Plasmas*, 27:22311, 2020.

[59] B. A. Jorns, C. A. Dodson, J. R. Anderson, D. M. Goebel, R. R. Hofer, M. J. Sekerak, A. Lopez Ortega, and I. G. Mikellides. Mechanisms for Pole Piece Erosion in a 6-kW Magnetically-Shielded Hall Thruster. In *52nd AIAA/SAE/ASEE Joint Propulsion Conference*, 2016. Paper no. 4839.

[60] B. A. Jorns, D. M. Goebel, I. G. Mikellides, and D. M. Goebel. Investigation of energetic ions in a 100-A hollow cathode. In *50th AIAA/ASME/SAE/ASEE Joint Propulsion Conference 2014*, 2014. Paper no. 3826.

[61] B. A. Jorns, I. G. Mikellides, and D. M. Goebel. Temporal Fluctuations in a 100-A LaB6 Hollow Cathode. In *33rd International Electric Propulsion Conference*, 2013. Paper no. 385.

[62] B. A. Jorns, I. G. Mikellides, and D. M. Goebel. Ion acoustic turbulence in a 100-A LaB6 hollow cathode. *Physical Review E - Statistical, Nonlinear, and Soft Matter Physics*, 90(6):1–10, 2014.

[63] B. A. Jorns, A. L. Ortega, I. G. Mikellides, A. Lopez Ortega, and I. G. Mikellides. First-principles modeling of the IAT-driven anomalous resistivity in hollow cathode discharges I: Theory. In *52nd AIAA/SAE/ASEE Joint Propulsion Conference*, 2016. Paper no. 4626.

[64] L. H. H. Jr. Kinetic Theory of Shock Structure Using an Ellipsoidal Distribution Function. In *Rarefied Gas Dynamics*, volume 1, page 193, Toronto, Canada, 1965. Academic Press.

[65] G. Karypis and V. Kumar. METIS* A Software Package for Partitioning Unstructured Graphs , Partitioning Meshes , and Computing Fill-Reducing Orderings of Sparse Matrices, 1998.

[66] V. I. Kolobov, R. R. Arslanbekov, and A. A. Frolova. Boltzmann solver with adaptive mesh in velocity space. In *AIP Conference Proceedings*, volume 1333, pages 928–933, 2011.

[67] K. Kubota, Y. Oshio, H. Watanabe, S. Cho, and I. Funaki. Numerical Simulation of Hollow Cathode with Hybrid-PIC Coupled with Growth Model of Ion Acoustic Turbulence. In *2018 Joint Propulsion Conference*, 2018. Paper no. 4513.

[68] K. Kubota, Y. Oshio, H. Watanabe, S. Cho, Y. Ohkawa, and I. Funaki. Numerical and Experimental Study on Discharge Characteristics of High-Current Hollow Cathode. In *52nd AIAA/SAE/ASEE Joint Propulsion Conference*, 2016. Paper no. 4628.

[69] L. Landau. On the Vibrations of the Electronic Plasma. *Journal of Physics*, 10(1):445–460, 1946.

[70] P. Leung, A. Y. Wong, and B. H. Quon. Formation of double layers. *Physics of Fluids*, 23(5):992–1004, 1980.

[71] D. Lev, R. M. Myers, K. M. Lemmer, J. Kolbeck, H. Koizumi, and K. Polzin. The technological and commercial expansion of electric propulsion. *Acta Astronautica*, 159:213–227, 2019.

[72] I. Levchenko, S. Xu, G. Teel, D. Mariotti, M. L. Walker, and M. Keidar. Recent progress and perspectives of space electric propulsion systems based on smart nanomaterials. *Nature Communications*, 9(1), 2018.

[73] R. Liang. *The Combination of Two Concentric Discharge Channels into a Nested Hall-Effect Thruster*. Dissertation, University of Michigan, 2013.

[74] D. M. Malaspina, J. R. Wygant, R. E. Ergun, G. D. Reeves, R. M. Skoug, and B. A. Larsen. Electric field structures and waves at plasma boundaries in the inner magnetosphere. *Journal of Geophysical Research: Space Physics*, 120(6):4246–4263, 2015.

[75] G. Manfredi. Long-time behavior of nonlinear landau damping. *Physical Review Letters*, 79(15):2815–2818, 1997.

[76] W. M. Manheimer and R. W. Flynn. Formation of nonthermal ion tails in the ion acoustic instability. *Physics of Fluids*, 17(2):409–415, 1974.

[77] J. F. McKenzie, F. Verheest, T. B. Doyle, and M. A. Hellberg. Compressive and rarefactive ion-acoustic solitons in bi-ion plasmas. *Physics of Plasmas*, 11(5):1762–1769, 2004.

[78] J. Meng, Y. Zhang, N. G. Hadjiconstantinou, G. A. Radtke, and X. Shan. Lattice ellipsoidal statistical BGK model for thermal non-equilibrium flows. *Journal of Fluid Mechanics*, 718:347–370, 2013.

[79] L. Mieussens. Discrete-Velocity Models and Numerical Schemes for the Boltzmann-BGK Equation in Plane and Axisymmetric Geometries. *Journal of Computational Physics*, 162(2):429–466, aug 2000.

[80] I. G. Mikellides and I. Katz. Wear Mechanisms in Electron Sources for Ion Propulsion, I: Neutralizer Hollow Cathode. *Journal of Propulsion and Power*, 24(4):855–865, jul 2008.

[81] I. G. Mikellides, I. Katz, and D. M. Goebel. Model of the Plasma Potential Distribution in the Plume of a Hollow Cathode. In *40th AIAA/ASME/SAE/ASEE Joint Propulsion Conference and Exhibit*, 2004. Paper no. 4108.

[82] I. G. Mikellides, I. Katz, and D. M. Goebel. Numerical Simulation of the Hollow Cathode Discharge Plasma Dynamics. In *International Electric Propulsion Conference*, 2005.

[83] I. G. Mikellides, I. Katz, D. M. Goebel, and K. K. Jameson. Evidence of nonclassical plasma transport in hollow cathodes for electric propulsion. *Journal of Applied Physics*, 101(6), 2007.

[84] I. G. Mikellides, I. Katz, D. M. Goebel, K. K. Jameson, and J. E. Polk. Wear Mechanisms in Electron Sources for Ion Propulsion, II: Discharge Hollow Cathode. *Journal of Propulsion and Power*, 24(4):866–879, 2008.

[85] I. G. Mikellides, I. Katz, D. M. Goebel, and J. E. Polk. Hollow cathode theory and experiment. II. A two-dimensional theoretical model of the emitter region. *Journal of Applied Physics*, 98(11):113303, dec 2005.

[86] I. G. Mikellides, I. Katz, R. R. Hofer, and D. M. Goebel. Magnetic shielding of a laboratory Hall thruster. I. Theory and validation. *Journal of Applied Physics*, 115(4), 2014.

[87] I. G. Mikellides, A. Lopez Ortega, D. M. Goebel, and G. Becatti. Dynamics of a hollow cathode discharge in the frequency range of 1–500 kHz. *Plasma Sources Science and Technology*, 29(3):035003, mar 2020.

[88] I. G. Mikellides and A. L. Ortega. Growth of the modified two-stream instability in the plume of a magnetically shielded Hall thruster. *Physics of Plasmas*, 27(10):100701, oct 2020.

[89] T. Miyasaka, T. Kobayashi, and K. Asato. Characteristics of ions impacting grid surfaces in an ion engine. *Vacuum*, 85(5):585–590, 2010.

[90] T. F. Morse. Kinetic Model Equations for a Gas Mixture. *The Physics of Fluids*, 7:2012, 1964.

[91] A. Myers, P. Colella, and B. Van Straalen. A 4th-order particle-in-cell method with phase-space remapping for the vlasov-poisson equation. *SIAM Journal on Scientific Computing*, 39(3):B467–B485, 2017.

[92] K. Nishikawa and C.-S. Wu. Effect of Electron Trapping on the Ion-Wave Instability. *Physical Review Letters*, 23(18):1020–1022, nov 1969.

[93] Y. Omura, H. Matsumoto, T. Miyake, and H. Kojima. Electron beam instabilities as generation mechanism of electrostatic solitary waves in the magnetotail. *Journal of Geophysical Research: Space Physics*, 101(A2):2685–2697, 1996.

[94] A. L. Ortega, B. A. Jorns, and I. G. Mikellides. Hollow Cathode Simulations with a First-Principles Model of Ion-Acoustic Anomalous Resistivity. *Journal of Propulsion and Power*, 34(4):1026–1038, 2018.

[95] K. Papadopoulos. A review of anomalous resistivity for the ionosphere. *Reviews of Geophysics*, 15(1):113, 1977.

[96] P. Petkaki, M. P. Freeman, T. Kirk, C. E. Watt, and R. B. Horne. Anomalous resistivity and the nonlinear evolution of the ion-acoustic instability. *Journal of Geophysical Research: Space Physics*, 111(1):1–12, 2006.

[97] P. Petkaki, C. E. J. Watt, R. B. Horne, and M. P. Freeman. Anomalous resistivity in non-Maxwellian plasmas. *Journal of Geophysical Research: Space Physics*, 108(A12):1–11, 2003.

[98] S. Pieraccini and G. Puppo. Implicit-explicit schemes for BGK kinetic equations. *Journal of Scientific Computing*, 32(1):1–28, 2007.

[99] S. B. Pope. *Turbulent Flows*. Cambridge University Press, 2000.

[100] V. Puech and S. Mizzi. Collision cross sections and transport parameters in neon and xenon. *Journal of Physics D: Applied Physics*, 24(11):1974–1985, 1991.

[101] B. H. Quon and A. Y. Wong. Formation of Potential Double Layers in Plasmas. *Physical Review Letters*, 37(21):1393–1396, 1976.

[102] D. J. Rader, M. A. Gallis, J. R. Torczynski, and W. Wagner. Direct simulation Monte Carlo convergence behavior of the hard-sphere-gas thermal conductivity for Fourier heat flow. *Physics of Fluids*, 18(7), 2006.

[103] A. L. Raisanen. *A Two-dimensional Hybrid-Direct Kinetic Model of a Hall Thruster.* Dissertation, University of Michigan, 2020.

[104] C. Riconda, A. Heron, D. Pesme, S. Hüller, V. T. Tikhonchuk, and F. Detering. Electron kinetic effects in the nonlinear evolution of a driven ion-acoustic wave. *Physical Review Letters*, 94(5):1–4, 2005.

[105] P. L. Roe. Characteristic-Based Schemes for the Euler Equations. *Annual Review of Fluid Mechanics*, 18(1):337–365, jan 1986.

[106] C. J. Roy. Grid convergence error analysis for mixed-order numerical schemes. In *15th AIAA Computational Fluid Dynamics Conference*, 2001. Paper no. 2606.

[107] K. Saeki, S. Iizuka, and N. Sato. Ion heating due to double-layer disruption in a plasma. *Physical Review Letters*, 45(23):1853–1855, 1980.

[108] R. Sagdeev and A. Galeev. *Nonlinear Plasma Theory.* W. A. Benjamin, New York, 1969.

[109] R. Sahu, A. R. Mansour, and K. Hara. Full fluid moment model for low temperature magnetized plasmas. *Physics of Plasmas*, 27(11), 2020.

[110] V. Saini, S. K. Pandey, P. Trivedi, and R. Ganesh. Coherent phase space structures in a 1D electrostatic plasma using particle-in-cell and Vlasov simulations: A comparative study. *Physics of Plasmas*, 25(9), 2018.

[111] G. Sary, L. Garrigues, and J. P. Boeuf. Hollow cathode modeling: II. Physical analysis and parametric study. *Plasma Sources Science and Technology*, 26(5):55008, 2017.

[112] G. Sary, L. Garrigues, and J.-P. P. Boeuf. Hollow cathode modeling: I. A coupled plasma thermal two-dimensional model. *Plasma Sources Science and Technology*, 26(5):55007, 2017.

[113] T. Sato and H. Okuda. Ion-Acoustic Double Layers. *Physical Review Letters*, 44(11):740–743, 1980.

[114] H. Schamel. The Theory of Double Layers. In *Symposium on Plasma Double Layers*, Roskilde, Denmark, 1982.

[115] A. N. Sekar and Y. C. Saxena. Development of ion-acoustic double layers through ion-acoustic fluctuations. *Plasma Physics and Controlled Fusion*, 27(2):181–191, 1985.

[116] A. Sleeper, J. Weinstock, and B. Bezzerides. Nonlinear Saturation of the Ion-Acoustic Instability. *Physical Review Letters*, 29(6):343–345, aug 1972.

[117] A. M. Sleeper, J. Weinstock, and B. Bezzerides. Nonlinear theory and angular spectrum of the ion-acoustic instability. *Physics of Fluids*, 16(9):1508–1518, 1973.

[118] G. A. Sod. A survey of several finite difference methods for systems of nonlinear hyperbolic conservation laws. *Journal of Computational Physics*, 31:1–31, 1978.

[119] T. E. Stringer. Electrostatic instabilities in current-carrying and counterstreaming plasmas. *Journal of Nuclear Energy. Part C, Plasma Physics, Accelerators, Thermonuclear Research*, 6(3):267–279, 1964.

[120] H. Sugimoto and Y. Sone. Numerical analysis of steady flows of a gas evaporating from its cylindrical condensed phase on the basis of kinetic theory. *Physics of Fluids A*, 4(2):419–440, 1992.

[121] P.-Y. C. R. Taunay, C. J. Wordingham, and E. Choueiri. An empirical scaling relationship for the total pressure in hollow cathodes. In *2018 Joint Propulsion Conference*, 2018. Paper no. 4428.

[122] B. van Leer. Towards the ultimate conservative difference scheme. V. A second-order sequel to Godunov's method. *Journal of Computational Physics*, 32(1):101–136, jul 1979.

[123] A. R. Vazsonyi and I. D. Boyd. An Axisymmetric Direct Kinetic Solver for Simulation of Hollow Cathode Plasmas. In *36th International Electric Propulsion Conference*, Vienna, Austria, 2019. Paper no. 331.

[124] A. R. Vazsonyi, K. Hara, and I. D. Boyd. Kinetic Simulation of Instability-Driven Anomalous Transport for a Hollow Cathode Plasma. In *AIAA Propulsion and Energy 2020 Forum*, aug 2020. Paper no. 3640.

[125] A. R. Vazsonyi, K. Hara, and I. D. Boyd. Non-monotonic double layers and electron two-stream instabilities resulting from intermittent ion acoustic wave growth. *Physics of Plasmas*, 27(11):112303, nov 2020.

[126] A. M. Verhoff. *Numerical Simulation of Transitional, Hypersonic Flows using a Hybrid Particle-Continuum Method*. Dissertation, University of Michigan, 2015.

[127] P. Virtanen, R. Gommers, T. E. Oliphant, M. Haberland, T. Reddy, D. Cournapeau, E. Burovski, P. Peterson, W. Weckesser, J. Bright, S. J. van der Walt, M. Brett, J. Wilson, K. J. Millman, N. Mayorov, A. R. J. Nelson, E. Jones, R. Kern, E. Larson, C. J. Carey, Polat, Y. Feng, E. W. Moore, J. VanderPlas, D. Laxalde, J. Perktold, R. Cimrman, I. Henriksen, E. A. Quintero, C. R. Harris, A. M. Archibald, A. H. Ribeiro, F. Pedregosa, and P. van Mulbregt. SciPy 1.0: fundamental algorithms for scientific computing in Python. *Nature Methods*, 17(3):261–272, mar 2020.

[128] G. V. Vogman. *Fourth-order conservative Vlasov-Maxwell solver for Cartesian and cylindrical phase space coordinates*. Dissertation, University of California, Berkeley, 2016.

[129] G. V. Vogman, U. Shumlak, and P. Colella. Conservative fourth-order finite-volume Vlasov–Poisson solver for axisymmetric plasmas in cylindrical (r,vr,vθ) phase space coordinates. *Journal of Computational Physics*, 373:877–899, 2018.

[130] J. E. Wiebenga. *High-Fidelity Material Response Modeling as Part of an Aerothermoelastic Framework for Hypersonic Flows*. Dissertation, University of Michigan, 2014.

[131] G. J. Williams, M. T. Domonkos, and J. M. Chavez. Measurement of doubly charged ions in ion thruster plumes. In *27th International Electric Propulsion Conference*, 2001. Paper no. 310.

[132] J. T. Yim. *Computational Modeling of Hall Thruster Channel Wall Erosion*. Dissertation, University of Michigan, 2008.

[133] A. B. Yoo, M. A. Jette, and M. Grondona. SLURM: Simple Linux Utility for Resource Management. In D. Feitelson, L. Rudolph, and U. Schwiegelshohn, editors, *Job Scheduling Strategies for Parallel Processing*, pages 44–60, Berlin, Heidelberg, 2003. Springer Berlin Heidelberg.